Quantum control and coherence of interacting spins in diamond

Quantum control and coherence of interacting spins in diamond

Proefschrift

ter verkrijging van de graad van doctor
aan de Technische Universiteit Delft,
op gezag van de Rector Magnificus prof. ir. K.C.A.M Luyben,
voorzitter van het College voor Promoties,
in het openbaar te verdedigen op 10 september 2012 om 12:30 uur

door

Gijsbertus DE LANGE

natuurkundig ingenieur
geboren te Rotterdam.

Dit proefschrift is goedgekeurd door de promotor:
Prof. dr. ir. L. P. Kouwenhoven

Copromotor:
Dr. ir. R. Hanson

Samenstelling van de promotiecommissie:

Rector Magnificus	voorzitter
Prof. dr. ir. L.P. Kouwenhoven	Technische Universiteit Delft, promotor
Dr. ir. R. Hanson	Technische Universiteit Delft, copromotor
Prof. dr. ir. L.M.K. Vandersypen	Technische Universiteit Delft
Prof. dr. ir. T.H. Oosterkamp	Universiteit Leiden
Prof. dr. F. Jelezko	Ulm University, Duitsland
Prof. dr. H. Bluhm	Rheinisch-Westfaelische Technische Hochschule Aachen, Duitsland
Dr. M. Blaauboer	Technische Universiteit Delft
Prof. dr. ir. J.E. Mooij	Technische Universiteit Delft, reservelid

Published by: Gijsbertus de Lange
Printed by: Ipskamp drukkers, Enschede
Cover art: Tremani

ISBN: 978-90-8593-129-4
Casimir PhD Series, Delft-Leiden 2012-18

Contents

Chapter 1

Introduction

1.1 Quantum science and technology

These are exciting times for experimental quantum physicists. Although the theory of quantum mechanics has been around for more than a century, some of the most powerful applications, which exploit the quantum nature of solid-state systems, have only recently started to appear on the technological horizon. The incredible developments in nanotechnology and mesoscopic physics, which deal with creating and understanding solid-state systems operating at the smallest scales, have led to new experiments in research and technology. In these experiments, quantum states are used to create a new class of solid-state devices with unprecedented performance and capabilities.

Out of all the current goals in quantum science and technology, the realisation of the quantum computer can probably considered to be the biggest. In a quantum computer bits are replaced by quantum objects called qubits [1], which can be in an arbitrary superposition of 0 and 1. The quantum computer enables a dramatic speed-up for some types of computational tasks for which the complexity increases exponentially with the size of the problem. Examples of such problems are prime factorization of large numbers [2] and simulations of large quantum systems [3, 4].

As an illustration, suppose we want to a quantum system (e.g., a molecule with several atoms) on a "classical" computer. Determining the exact level structure of such a system using the combined computational power of every classical computer that exists in the world today takes much longer than the current lifetime of the universe. And even if future computers are fast enough, storing a maximal superposition state of a system with 500 degrees of freedom (such as our molecule) on a classical computer, requires many more bits than there are atoms in the universe. This sets a rather fundamental limit to what is possible with

conventional computational means. On a quantum computer, however, superposition states are directly encoded in superposition states of qubits, and therefore do not require such large resources.

More conventional areas of technology also stand to gain tremendously by exploiting quantum states and their evolution. Extremely sensitive magnetic and electric field probes with nanoscale resolution can be created by tracking the evolution of a superposition state of a single spin. Such probes can be used for example in data storage or to image the protons in single molecules [5].

The operation of devices based on isolated quantum systems requires the initialization and read out of fragile quantum states, and an exceptionally high level of control over the evolution of these quantum states. Experiments involving isolated quantum systems in the solid state could only be performed after the incredible advancements made in device fabrication and experimental control techniques since the start of the eighties of the last century. Since then, quantum control has been achieved in a rich variety of single solid state quantum systems such as single electrons in quantum dots [6], superconducting circuits [7] and defects in solids [8, 9].

The main challenge in all of these experiments is to avoid the loss of quantum coherence by control errors and uncontrolled coupling to the environment. Although these experiments demonstrate a level of control that is sufficient to perform the first proof-of-principle experiments, the perfection needed to use them in actual applications is still lacking. The inherent contradiction of controlling and coupling such systems together on the one hand and isolating them from their environment on the other, is what makes these experiments so challenging. However, by controlling its evolution with high precision, a quantum system can be efficiently isolated from its environment [10], while, if so desired, maintaining the internal coherent couplings between its components (e.g., to perform computational tasks [11]).

Achieving high-fidelity control of quantum systems and using it to study and counteract decoherence of quantum systems in the solid state are the main motivations for the experiments in this thesis. We demonstrate that we can preserve the quantum state of a single electron spin with carefully designed sequences of high fidelity pulses (chapter 4 of this thesis) and that they can be used to increase the storage time of quantum information. Furthermore, as is demonstrated experimentally in this thesis, these sequences can also be used to dramatically reduce the magnetic field noise of a single spin magnetometer and improve its sensitivity to time-varying magnetic fields. These experiments provide an illustration of how high-fidelity control over the evolution of an isolated quantum system enables the development of new devices with superior performance.

Apart from the possible technological applications, studying quantum control and decoherence of quantum systems with increasing complexity will aid in our

understanding and interpretations of some of quantum mechanics' most peculiar predictions. Take, for instance, the projective quantum measurement, during which the state of the observed system probabilistically changes to the state corresponding to the observation [12]. Although there is a working formalism for dealing with this so-called "collapse" of the wavefunction, to this day it is unknown how this collapse occurs exactly. On a related issue it is still somewhat of a mystery how the macroscopic "classical" world, the one we experience every day, emerges from the quantum world. Interesting ideas in this respect have been put forward, where decoherence is thought to be able to bridge the gap between the quantum and classical world [13].

In the final two experiments of this thesis we focus more on the fundamental aspects of decoherence and the interactions between quantum systems. Using the techniques developed in the first part of this thesis we demonstrate quantum control of a mesoscopic spin ensemble and a single spin and study the interaction between them. Finally, we explore the coupling between a large spin ensemble and a superconducting circuit. Apart from being interesting from a fundamental perspective, one can also think of constructing such hybrid devices where two or more systems are combined in a single device with superior performance.

1.2 Diamond spins in quantum science and technology

Spins in diamond are now used by many research groups around the world in experimental quantum information and computation as well as in other areas of quantum science and technology. Spins in diamond demonstrate long spin coherence times that can be coherently controlled, even at room temperature, and therefore form a unique platform to study spin-spin interactions and decoherence. Figure 1.1 shows a few of the paramagnetic impurities that exist in typical diamond samples. The two main defects used in the experiments described in this thesis are the single substitutional nitrogen impurity and the nitrogen vacancy (NV) color center. The latter has a unique combination of highly useful properties for experiments on single spins, whereas ensembles of nitrogen spins can be used in hybrid devices based on the combination of diamond and superconducting circuits.

1.2.1 The nitrogen-vacancy center in diamond

The most promising paramagnetic impurity in diamond for applications in quantum technologies is the nitrogen-vacancy (NV) color center [15], which is a single substitutional nitrogen atom with a vacancy in one of the adjacent lattice sites

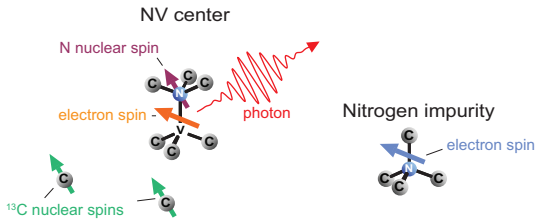

Figure 1.1: Spins in diamond. The nitrogen vacancy (NV) center consists of a substitutional nitrogen atom adjacent to a vacancy in the diamond carbon lattice. Its electron spin is coupled to the nuclear spin of its own nitrogen atom, and can furthermore be coupled to nuclear spins of nearby ^{13}C atoms or to electron spins of nearby substitutional nitrogen impurities. The NV center has spin-dependent optical transitions, allowing its quantum state to be transmitted over long distances through the use of photons. Picture adapted from [14].

(Fig. 1.1). The NV center has a spin triplet electronic ground state and strong spin dependent optical transitions within the band gap of diamond. The list of attractive features of the NV center is quite long. One of the main features of the NV center is that it is a bright and stable source of single photons [16]. Its electronic spin state can be initialized and read out by simple optical means [17]. It exhibits long coherence times, even at room temperature, ranging from 3 μs [18] to almost 2 ms [19] and its spin state can be coherently manipulated on ns timescales [20, 21] using electron spin resonance techniques. Furthermore, the strong coupling to its host ^{14}N nuclear spin make it a basic two qubit register which can readily be turned into three qubits if all the spin levels are used and even more qubits can be contained in the register when nearby ^{13}C spins are located close the NV centers [22, 23].

NV centers can be used as spin based magnetic field sensors, or magnetometers, which may find applications in areas such as material science, data storage and biomedical science [5, 24, 25]. They are highly sensitive due to the long spin coherence times and nanoscale resolution can be achieved by using shallow NV centers or nanocrystals. NV magnetometers in nanocrystals have already been shown to be compatible with living human cells [25], potentially allowing new ways of exploring intracellular processes.

From a more fundamental perspective the NV center forms a excellent testbed to study decoherence [26–30]. Its magnetic environment can be tailored to range from highly dense and dynamic [26], to slow [31], to being practically devoid of any magnetic activity [19].

The experiments in this thesis involving NV centers are all conducted at room temperature. However, the already impressive list of favorable properties

becomes even longer when NV centers are used at low (< 10 K) temperatures. At these temperatures, both the electronic and nuclear spin states of an NV center can be projected and read out in a single measurement shot [32]. The optical transitions at these temperatures have narrow line widths and can be coherently controlled [33]. By addressing the right optical transitions the electronic spin of the NV center can be entangled with its emitted photon [34]. This means that in principle the spin states of multiple distant NV quantum registers can be coupled together by interfering their emitted photons on a beam splitter [35, 36]. These properties can be used to close some of the loop holes, such as the communication and detector loopholes, in Bell test experiments and, although there are many challenges ahead, such a network of multiple, optically coupled NV qubit registers may some day be used to perform multi-qubit quantum algorithms [35].

1.2.2 Nitrogen impurities

The parent defect of the NV center is the single substitutional nitrogen atom. It is a paramagnetic defect which has an electron spin ($S = 1/2$). Ensembles of nitrogen impurities can be used in solid-state hybrid architectures as a long term memory. Solid-state qubits such as those created using superconducting circuits are easy to couple together and relatively straightforward to scale up [37], but they generally suffer from relatively short coherence times. Spin ensembles can be used as a long term quantum memory for superconducting qubits by storing quantum information in a collective mode involving the collective motion of $\sim 10^{12}$ spins [38, 39]. Apart from the possible application, it is mind boggling that such a large ensemble of independent systems can move in unison and demonstrate quantum coherence with a single microwave photon.

Research with solid-state hybrid devices is still in its infancy, but already quite remarkable advancements have been made by using ensembles of NV centers in quantum circuits in which a single microwave photon was coherently swapped back-and-forth between a superconducting qubit and the NV ensemble [40, 41] . The advantage of using NV ensembles is that they can be used at zero magnetic field. However, for every NV center created there are several nitrogen impurities. These impurities will cause dephasing and degrade the memory performance. Instead highly pure ensembles of nitrogen impurities can be used at high magnetic field. This implies that one has to develop new architectures for superconducting qubit devices which are able to operate at high magnetic fields. Efforts by our collaborators are under way to creating such superconducting circuits, but they do not yet exist at this time.

1.3 Thesis overview

Chapter 2 provides an introduction to the theoretical and experimental concepts that are aimed in providing a basis for understanding the subsequent chapters. I start by explaining some of the basic theory of quantum control, quantum processes and spin-spin interactions. A detailed description of the most common magnetic impurities found in diamond is given in the next section. A mean field theoretical model is provided that provides an accurate description of the decoherence mechanism for a single NV spin which interacts with a bath of electron spins. The final section gives an overview of the experimental techniques used in this thesis.

The first experiment described in 3 describes a new technique that is used to measure pulse errors using erroneous pulses in a bootstrap protocol. It also describes how the acquired knowledge of pulse errors can be used for corrections in quantum process tomography.

In chapter 4 we show that an arbitrary state of a single quantum object, a single NV spin, can be protected from decoherence by applying self correcting dynamical decoupling sequences. We use these self-correcting dynamical decoupling sequences in chapter 5 as sensing sequences to enhance the sensitivity of a single-spin magnetometer.

In chapter 6 we demonstrate control of the spin bath surrounding the NV spin and use that to suppress dephasing of the NV spin and probe the quantum dynamics and temporal correlations of the nitrogen spin bath.

Chapter 7 demonstrates experimentally that strong coupling can be achieved between an ensemble of nitrogen spins and a superconducting microwave resonator. We use this device to study depolarization and spin diffusion of the nitrogen spin ensemble.

In the final chapter the main results of this thesis are summarized and discussed and an outlook for the future is given.

Bibliography

[1] T. D. Ladd *et al.* Quantum computers. *Nature* **464**, 45 (2010).

[2] P. W. Shor. Algorithms for quantum computation: discrete logarithms and factoring. *35^{th} Annual Symposium on Foundations of Computer Science*. IEEE Press, Los Alamitos, CA (1994).

[3] R. P. Feynman. Simulating physics with computers. *International Journal of Theoretical Physics* **21**, 467 (1982).

[4] S. Lloyd. Universal quantum simulators. *Science* **273**, 1073 (1996).

[5] C. L. Degen. Scanning magnetic field microscope with a diamond single-spin sensor. *Applied Physics Letters* **92**, 243111 (2008).

[6] R. Hanson, L. P. Kouwenhoven, J. R. Petta, S. Tarucha and L. M. K. Vandersypen. Spins in few-electron quantum dots. *Reviews of Modern Physics* **79**, 1217 (2007).

[7] Y. Nakamura, Y. Pashkin and J. Tsai. Coherent control of macroscopic quantum states in a single-cooper-pair box. *Nature* **398**, 786 (1999).

[8] A. Morello *et al.* Single-shot readout of an electron spin in silicon. *Nature* **467**, 687 (2010).

[9] F. Jelezko, T. Gaebel, I. Popa, A. Gruber and J. Wrachtrup. Observation of coherent oscillations in a single electron spin. *Physical Review Letters* **92**, 76401 (2004).

[10] L. Viola, S. Lloyd and E. Knill. Universal Control of Decoupled Quantum Systems. *Physical Review Letters* **83**, 4888 (1999).

[11] T. van der Sar *et al.* Decoherence-protected quantum gates for a hybrid solid-state spin register. *Nature* **484**, 82 (2012).

[12] M. A. Nielsen and I. Chuang. *Quantum Computation and Quantum Information*. Cambridge University Press, 2000.

[13] W. H. Zurek. Decoherence, einselection, and the quantum origins of the classical. *Reviews of Modern Physics* **75**, 715 (2003).

[14] T. van der Sar. *Quantum control of single spins and single photons in diamond*. Ph.D. thesis, Delft, The Netherlands (2012).

[15] F. Jelezko and J. Wrachtrup. Single defect centres in diamond: A review. *physica status solidi (a)* **203**, 3207 (2006).

[16] C. Kurtsiefer, S. Mayer, P. Zarda and H. Weinfurter. Stable solid-state source of single photons. *Physical Review Letters* **85**, 290 (2000).

[17] A. Gruber *et al.* Scanning Confocal Optical Microscopy and Magnetic Resonance on Single Defect Centers. *Science* **276**, 2012 (1997).

[18] R. Hanson, F. M. Mendoza, R. J. Epstein and D. D. Awschalom. Polarization and readout of coupled single spins in diamond. *Physical Review Letters* **97**, 087601 (2006).

[19] G. Balasubramanian *et al.* Ultralong spin coherence time in isotopically engineered diamond. *Nature Materials* **8**, 383 (2009).

[20] F. Jelezko *et al.* Observation of coherent oscillation of a single nuclear spin and realization of a two-qubit conditional quantum gate. *Physical Review Letters* **93**, 130501 (2004).

[21] G. D. Fuchs, V. V. Dobrovitski, D. M. Toyli, F. J. Heremans and D. D. Awschalom. Gigahertz dynamics of a strongly driven single quantum spin. *Science* **326**, 1520 (2009).

[22] L. Childress *et al.* Coherent dynamics of coupled electron and nuclear spin qubits in diamond. *Science* **314**, 281 (2006).

[23] M. Gurudev Dutt *et al.* Quantum register based on individual electronic and nuclear spin qubits in diamond. *Science* **316**, 1312 (2007).

[24] J. M. Taylor *et al.* High-sensitivity diamond magnetometer with nanoscale resolution. *Nature Physics* **4**, 810 (2008).

[25] L. McGuinness *et al.* Quantum measurement and orientation tracking of fluorescent nanodiamonds inside living cells. *Nature Nanotechnology* **6**, 358 (2011).

[26] R. Hanson, V. V. Dobrovitski, A. E. Feiguin, O. Gywat and D. D. Awschalom. Coherent dynamics of a single spin interacting with an adjustable spin bath. *Science* **320**, 352 (2008).

[27] V. V. Dobrovitski, A. Feiguin, D. D. Awschalom and R. Hanson. Decoherence dynamics of a single spin versus spin ensemble. *Physical Review B* **77**, 245212 (2008).

[28] V. V. Dobrovitski, A. E. Feiguin, R. Hanson and D. D. Awschalom. Decay of rabi oscillations by dipolar-coupled dynamical spin environments. *Physical Review Letters* **102**, 237601 (2009).

[29] G. de Lange, Z. H. Wang, D. Ristè, V. V. Dobrovitski and R. Hanson. Universal dynamical decoupling of a single solid-state spin from a spin bath. *Science* **330**, 60 (2010).

[30] G. de Lange *et al.* Controlling the quantum dynamics of a mesoscopic spin bath in diamond. *Scientific Reports* **2**, 382 (2012).

[31] E. Togan, Y. Chu, A. Imamoglu and M. Lukin. Laser cooling and real-time measurement of the nuclear spin environment of a solid-state qubit. *Nature* **478**, 497 (2011).

[32] L. Robledo *et al.* High-fidelity projective read-out of a solid-state spin quantum register. *Nature* **477**, 574 (2011).

[33] L. Robledo, H. Bernien, I. Van Weperen and R. Hanson. Control and coherence of the optical transition of single nitrogen vacancy centers in diamond. *Physical Review Letters* **105**, 177403 (2010).

[34] E. Togan *et al.* Quantum entanglement between an optical photon and a solid-state spin qubit. *Nature* **466**, 730 (2010).

[35] L. Jiang, J. Taylor, A. Sørensen and M. Lukin. Distributed quantum computation based on small quantum registers. *Physical Review A* **76**, 062323 (2007).

[36] L. Childress, J. M. Taylor, A. S. Sørensen and M. D. Lukin. Fault-tolerant quantum communication based on solid-state photon emitters. *Physical Review Letters* **96**, 070504 (2006).

[37] J. Majer *et al.* Coupling superconducting qubits via a cavity bus. *Nature* **449**, 443 (2007).

[38] Y. Kubo *et al.* Strong Coupling of a Spin Ensemble to a Superconducting Resonator. *Physical Review Letters* **105**, 140502 (2010).

[39] D. Schuster *et al.* High-cooperativity coupling of electron-spin ensembles to superconducting cavities. *Physical Review Letters* **105**, 140501 (2010).

[40] Y. Kubo *et al.* Hybrid quantum circuit with a superconducting qubit coupled to a spin ensemble. *Physical Review Letters* **107**, 220501 (2011).

[41] X. Zhu *et al.* Coherent coupling of a superconducting flux qubit to an electron spin ensemble in diamond. *Nature* **478**, 221 (2011).

Chapter 2

Quantum control of interacting spins in diamond

The theoretical concepts and the experimental techniques covered in this chapter form the foundation for all the experiments described in the rest of this thesis. All the experimental studies presented in this thesis involve the manipulation and detection of coupled spins using quantum control techniques. I therefore start with a section containing basic theory behind spin control, the description and characterization of quantum processes and spin-spin interactions. The next section of this chapter gives a detailed description of the various species of spins that are typically present in diamond samples. The details of the experimental techniques that are used throughout this thesis will be given in 2.4.

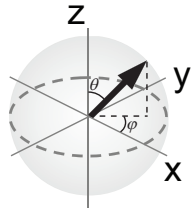

Figure 2.1: Bloch sphere representation for a qubit. The state of the qubit is indicated by the arrow.

2.1 Basic theory

Before I go into the specific details regarding interacting spins in diamond, I first provide a brief introduction of few basic concepts regarding quantum control, the characterization of quantum processes and spin-spin interactions. For more details on the subjects covered in this section, the reader is referred to the books listed by refs. [1, 2].

2.1.1 Qubits and quantum operations

The two-level system is the simplest quantum system. Spins with $S = 1/2$ are the canonical examples of two-level systems. A qubit can be created from any multi-level system which has two levels that can be isolated and selectively addressed. These two levels can then be treated as an effective two-level system, or pseudo spin-1/2.

Spins are magnetic moments and they will therefore respond to magnetic fields much in the same way as classical magnetic moments. As we will show in this section, the most direct way to manipulate a spin is to use oscillating magnetic fields. A convenient geometrical tool to describe what happens to a spin which is subject to a magnetic field is to represent its state as a vector in the Bloch sphere (Fig. 2.1) which points along its magnetization. The eigenstates $|\uparrow\rangle$ and $|\downarrow\rangle$ are on the poles located on the z-axis. For an arbitrary pure state of a qubit, neglecting a global phase, we can write

$$|\Psi\rangle = \cos\frac{\theta}{2}|\uparrow\rangle + \sin\frac{\theta}{2}e^{i\varphi}|\downarrow\rangle \tag{2.1}$$

with θ and φ defined as in Fig. 2.1. We can now label a superposition along the

x or y axis of the Bloch sphere as

$$|X\rangle = \frac{|\uparrow\rangle + |\downarrow\rangle}{\sqrt{2}} \tag{2.2}$$

$$|Y\rangle = \frac{|\uparrow\rangle + i|\downarrow\rangle}{\sqrt{2}} \tag{2.3}$$

Equivalently, one can write its density matrix $\rho = |\Psi\rangle\langle\Psi|$ in terms of the expectation values $r_{x,y,z} = \langle\Psi|\sigma_{x,y,z}|\Psi\rangle$

$$\rho = \frac{1}{2}(I + r_x\sigma_x + r_y\sigma_y + r_z\sigma_z) \tag{2.4}$$

with σ_i the Pauli spin matrices (i.e. with eigenvalues -1 and +1). The vector in the Bloch sphere is simply $\overrightarrow{r} = (r_x, r_y, r_z)$. The superposition state along the $x(y)$-axis is $\rho = \frac{I}{2} + \frac{\sigma_{x(y)}}{2}$. A pure state corresponds to $|\overrightarrow{r}| = 1$ and $|\overrightarrow{r}| < 1$ implies that the state is mixed. This mixing may be the result of the qubit being entangled with another quantum system (e.g. the nitrogen nuclear spin), or due to qubit decoherence. It is therefore convenient to represent spin states using the density matrix representation when they are analyzed in the context of decoherence.

Driving spin transitions is done by generating an oscillating magnetic field. This magnetic control field B_x is oriented perpendicular to the quantization axis z of the spin and with its frequency tuned in resonance with the transition. All experiments in this thesis involve quantum control of spins which have transition frequencies in the microwave (MW) and radiofrequency (RF) regime. The Hamiltonian that describes the electron spin resonance (ESR) of a spin, quantized along the z direction and with angular transition frequency ω_0, is given by

$$H_{\mathrm{dr}} = \omega_0 S_z + \Omega_1 \cos(\omega_c t + \phi) S_x \tag{2.5}$$

where $\Omega_1 = \gamma_e B_x$ is the driving strength and ω_c and ϕ are the carrier frequency and phase of the oscillating magnetic field respectively. The time dependence in (2.5) can be removed by applying the transformation $S_{x',y',z'} = \exp(-i\omega_c t S_z) S_{x,y,z} \exp(i\omega_c t S_z)$, i.e. move to the frame that rotates around the z axis with angular frequency ω_c, and disregard the terms which oscillate with angular frequency $\omega_0 + \omega_c$. This is the well known rotating wave approximation, which is valid for $\Omega_1 << \omega_0$. The result is the time-independent effective Hamiltonian for a driven two level system with detuning $\Delta = \omega_0 - \omega_c$ given by

$$H'_{\mathrm{eff}} = \Delta S_{z'} + \frac{\Omega_1}{2}[S_{x'}\cos(\varphi) + S_{y'}\sin(\varphi)] \tag{2.6}$$

where the $S_{x',y',z'}$ are the operators in the rotating frame.

Applying the driving to the state $|\Psi_i\rangle$ will cause it to precess according to the evolution operator $U(t) = \exp[-iH'_{\text{eff}}t]$. The operator $U(t)$ describes a rotation of the state vector in the Bloch sphere around the axis $\overrightarrow{n} = (\omega_1 \cos\varphi, \omega_1 \sin\varphi, \Delta)/\omega_{\text{eff}}$ with angular frequency $\omega_{\text{eff}} = \sqrt{\omega_1^2 + \Delta^2}$ and $\omega_1 = \Omega_1/2$ and $U(t) = \exp^{-i\omega_{\text{eff}} t \overrightarrow{n}\cdot\overrightarrow{\sigma}}$.

From Eq. (2.6) we see that when $\omega_c = \omega_0$ (i.e. the carrier is in resonance with the spin transition) and $\phi = 0$, then $U(t) = I\cos(\frac{\omega_1 t_p}{2}) + \sigma_x \sin(\frac{\omega_1 t_p}{2})$. The state vector will start to rotate around the x'-axis in the rotating frame with frequency ω_1. The driving will induce coherent oscillations between the populations of the levels involved. These oscillations are known as Rabi oscillations and they are key ingredients for gate operations in quantum information and other quantum technologies with spins.

Arbitrary gate operations $R_\varphi(\theta)$ can be applied to the qubit by driving it on resonance with a pulsed oscillating magnetic field with phase φ and pulse length t_p such that $\theta = \omega_1 t_p$. These gate operations rotate the state vector $\overrightarrow{r}$ around the axis $\cos(\varphi)x' + \sin(\varphi)y'$. Any rotation over an arbitrary angle and around any axis can be constructed from multiple successive rotations. In this thesis we will use sequences of π-pulses, or $R_{0^\text{o}(90^\text{o})}(\pi)$ rotations, which are denoted by the short-hand notation as $X(Y)$ pulses. The $R_{0^\text{o}(90^\text{o})}(\pi/2)$ rotations used to prepare and project superposition states on the x' and y' axes Bloch sphere are denoted as $X/2(Y/2)$.

2.1.2 Quantum process tomography (QPT)

So far we have only described unitary, or reversible, operations on a qubit. However, decoherence due to energy relaxation or dephasing are processes which are irreversible and therefore not unitary. Such processes can be described using the product operator formalism [1], where the quantum process is defined in terms of basis operators. For operations on a single qubit a complete set of operations is given by the 2×2 identity matrix and the 2×2 Pauli matrices $\{E_0, E_1, E_2, E_3\} = \{I, \sigma_x, \sigma_y, \sigma_z\}$. Any process $\varepsilon(\rho_i)$ acting on a initial state ρ_i can then be decomposed into these four basic operations

$$\rho_o = \varepsilon(\rho_i) = \sum_{k,m=0}^{3} E_k \rho_i E_m^\dagger \chi_{km} \tag{2.7}$$

The process is then completely characterized by the process matrix χ. The goal of quantum process tomography (QPT) is to find χ.

An example of the χ matrices for two processes is given in Fig. 2.2. The upper matrices represent the real and imaginary part of the χ matrix for the unitary process that describes a $\pi/2$ rotation around the z axis, respectively, which is given by $\varepsilon(\rho) = \frac{1}{2}(I + i\sigma_z)\rho(I - i\sigma_z)$. In this case $\chi_{00} = \chi_{33} = \frac{1}{2}$ and

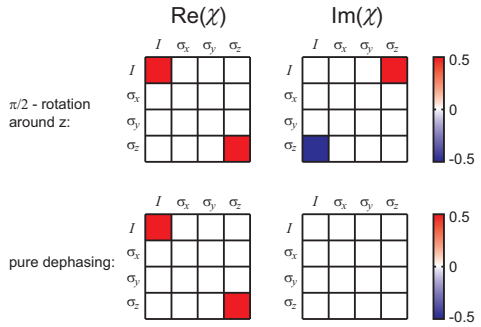

Figure 2.2: Top: Real (left) and imaginary (right) parts of the process matrix χ for the unitary process of a $\pi/2$-pulse around the z axis. Bottom: Proces matrix describing pure dephasing.

$\chi_{03} = -\chi_{30} = \frac{i}{2}$ and all other elements are zero. Depicted on the bottom of Fig. 2.2, is the non-unitary process of complete dephasing, characterized by the process $\varepsilon(\rho) = \frac{1}{2}(I\rho I + \sigma_z\rho\sigma_z)$. Here $\chi_{00} = \chi_{33} = \frac{1}{2}$ and all other elements including the off-diagonal terms are zero.

QPT is performed by preparing an independent set of input states ρ_i onto which the quantum process is applied. State tomography is then performed on each resulting output state. The process can be reconstructed from the correlations between the resulting output states by following the recipe found in Ref. [1].

That QPT can be used to determine if processes are unitary or non-unitary is especially relevant when QPT is used to test the performance of quantum control protocols and allows one to separate systematic errors from decoherence. The experimental setup for quantum control of spins and the experimental implementation of QPT are detailed in section 2.4.2 and chapter 3, respectively.

There are two issues that arise when QPT is performed experimentally. First there is the problem of measurement noise in the results of state tomography. A second problem arises from the systematic errors in the preparation and read out pulses. Both these problems may result in correlations between output states that result in a unphysical χ matrix, meaning that it has negative eigenvalues [1]. Chapter 3 addresses the issue that arises when states are prepared and read out using pulses that contain systematic errors and how to correct for those errors if needed. That leaves the problem of measurement noise. This leads to random errors which can not be corrected. Instead, a physical χ matrix is found using maximum likelihood estimation (MLE) [3], which is the closest match to the measured χ matrix, the details of which can also be found in chapter 4.

2.1.3 The magnetic dipole coupling

Many of the effects described in this thesis are the result of spin-spin interactions. The direct interaction between two spins usually results from the magnetic dipole coupling. Two spins sense each other's magnetic fields that are generated by their magnetic moments. A magnetic dipole with moment $\boldsymbol{\mu}$ will produce a magnetic field $\delta\mathbf{b}_{\mathrm{dip}}$, at some distance r from the dipole, that is given by [2]

$$\delta\mathbf{b}_{\mathrm{dip}} = \frac{\mu_0}{4\pi r^3}\left(3\mathbf{n}\left(\boldsymbol{\mu}\cdot\mathbf{n}\right) - \boldsymbol{\mu}\right), \tag{2.8}$$

where μ_0 the magnetic permeability and $\mathbf{n}$ the unit vector that points towards the moment. To get a feeling for the numbers; for an electron spin with moment $\mu_e = \gamma_e\hbar\hat{\mathbf{S}}$ with $\gamma_e = 2.8$ MHz/G, the prefactor in Eq. (2.8) has a magnitude of ~ 2 G at 3 nm distance. For two electron spins, with spin operators $\hat{S}_i$ and $\hat{S}_j$ and gyromagnetic ratios γ_i and γ_j, the dipole-interaction term of the Hamiltonian can be derived from Eq. (2.8)

$$H_{\mathrm{dip}} = \frac{\mu_0\gamma_i\gamma_j\hbar^2}{4\pi r^3}\left[\hat{\mathbf{S}}_i\cdot\hat{\mathbf{S}}_j - 3\left(\hat{\mathbf{S}}_i\cdot\mathbf{n}_{ij}\right)\left(\hat{\mathbf{S}}_j\cdot\mathbf{n}_{ij}\right)\right] \tag{2.9}$$

The strength and nature of the coupling depends on the exact geometry of the situation and whether or not the two spins $\hat{S}_i$ and $\hat{S}_j$ belong to the same species (i.e. have similar resonance frequencies). In most of the situations in the experiments described in this thesis the dipolar term is not the dominating term in the Hamiltonian and can therefore be treated as a perturbation.

2.1.4 Electron-nuclear hyperfine interaction

A typical situation that occurs in defects in solids is when an electronic spin $\mathbf{S}$ interacts with nuclear spin $\mathbf{I}$. The nature of the coupling depends heavily on the orbital wavefunction Ψ_e of the electron. One contribution to the hyperfine interaction is the result of the dipolar interaction averaged over the electron orbital wavefunction

$$\langle H_{\mathrm{dip}}\rangle_{\Psi_e} = \int H_{\mathrm{dip}}|\Psi_e(\mathbf{r})|^2 d^3\mathbf{r} \tag{2.10}$$

where $\mathbf{r}$ is taken with respect to the nuclear spin. From this it can be shown that the dipolar interaction only contributes to the hyperfine interaction when $\Psi_e(\mathbf{r})$ is not spherically symmetric with respect to the nucleus carrying the nuclear spin. Contact hyperfine interaction results when $\Psi_e(0) \neq 0$ (e.g. when the atom occupies an s-type orbital of the atom containing the nuclear spin). If one assumes that $\Psi_e(\mathbf{r}) = \Psi_e(0)$ (i.e. the electron wavefunction does not vary over volumes comparable to that of the nucleus) the contact term H_{cont} can be determined by

calculating the energy of the electron spin S which interacts with the magnetic field $\mathbf{B}_{\rm nuc}$ produced by the nuclear spin I. Eq. (2.10) then reduces to the volume integral of the magnetic field produced by the nuclear magnetic moment which occupies a volume bounded by R_N [4]

$$H_{\rm cont} = \gamma_S \hbar |\Psi_e(0)|^2 \mathbf{S} \cdot \int_{r<R_N} \mathbf{B}_{\rm nuc} d^3\mathbf{r} \tag{2.11}$$

$$= -\frac{2}{3}\mu_0 \gamma_S \gamma_I \hbar^2 |\Psi_e(0)|^2 \mathbf{S} \cdot \mathbf{I} \tag{2.12}$$

The total hyperfine interaction is the $H_{\rm HF} = H_{\rm cont} + \langle H_{\rm dip} \rangle_{\Psi_e}$. The contact hyperfine interaction is always isotropic and results from the s-type contribution of $\Psi_e(\mathbf{r})$. Any anisotropy in $H_{\rm HF}$ is therefore the result from orbital contributions to Ψ_e which are of p, d, f or higher. In diamond s and p-type orbitals are the lowest energy orbitals that are available for bonds. Therefore, any anisotropy in the electron-nuclear hyperfine interaction with nuclei located within defects in diamond are the result from the p-type contribution to $\Psi_e(\mathbf{r})$.

2.2 Paramagnetic impurities in diamond

The experiments described in this thesis are all performed using paramagnetic defects in diamond. This section therefore will provide a detailed description of the defects studied in these experiments. We start with the most important defect.

2.2.1 The NV color center

The nitrogen vacancy center was already introduced briefly in section 1.2.1. NV center research has intensified a great deal in the past fifteen years. This section[1] provides an overview of the current level of understanding details on the electronic level structure, spin properties of the optical transitions and spin level structure of the electronic ground state of the NV center.

Electronic level structure

The electronic structure of the NV center has been the subject of intensive theoretical and experimental studies in recent years [6–9]. The NV center can exist in two charge states: the neutral state NV^0 and the negatively charged state NV^-. In this thesis we deal exclusively with the NV^- center, and for brevity we will denote this as the NV center.

[1] The following section is adapted from [5]

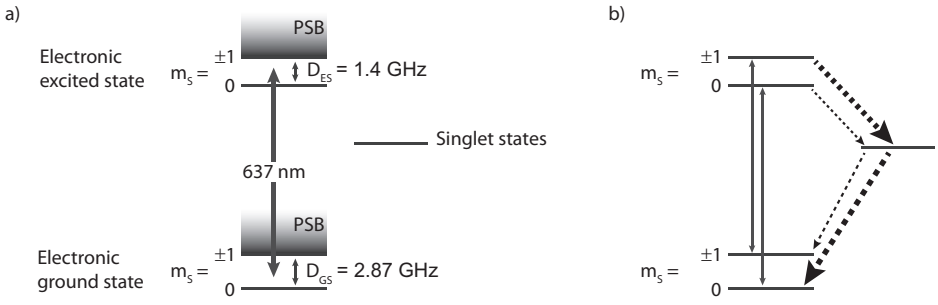

Figure 2.3: a, Energy level diagram of the NV center. The ground state of the NV center is a spin triplet with zero-field splitting $D_{\mathrm{GS}} = 2.87$ GHz which is connected to the excited state by an optical transition with a zero-phonon-line (ZPL) at 637 nm. At room temperature, the excited state can be described as a spin triplet with zero-field splitting $D_{\mathrm{ES}} = 1.4$ GHz. To explain the properties of the NV center relevant for the experiments described in this thesis, it suffices to summarize the singlet states states into one level. **b,** Energy level diagram explaining the optical spin readout and initialization mechanism. The red lines indicate optical transitions, the dashed lines indicate the other primary (dark) transitions. Spin polarization into the $m_s = 0$ state is a result of spin-dependent decay via the singlet states. Decay from the excited state into the singlet states happens primarily from the $m_s = \pm 1$ states, and decay from the singlet states into the ground state happens primarily into the $m_s = 0$ state.

There are six electrons associated with the NV center [6]: three from the dangling bonds of the vacancy, two from dangling bonds of the nitrogen atom, and one additional electron which is attracted from somewhere else in the diamond, presumably another nitrogen atom. The electronic ground state is a spin triplet, of which the $m_s = 0$ and $m_s = \pm 1$ states, where m_s denotes the quantum number of the spin projection along the symmetry axis (z-axis) of the NV center, are split in energy due to spin-spin interaction by a zero-field splitting $D = 2.87$ GHz (Fig. 2.3a).

The electronic excited state is also a spin triplet but an orbital doublet. It is connected to the electronic ground state by a strong optical transition with a zero-phonon line (ZPL) at 637 nm (1.945 eV). At room temperature, rapid inter-orbital transitions within the excited state lead to an effective averaging of the spin properties of the orbitals [10]. As a result, the orbital doublet nature can be neglected and the electronic excited state can be described as a single spin triplet, of which the spin states $m_s = 0$ and $m_s = \pm 1$ are split by a zero-field splitting $D_{ES} = 1.4$ GHz (Fig. 2.3a).

It is now believed that there exist at least three singlet states that lie between the electronic ground and excited state [11]. Recent ensemble measurements

have shown that there is an optical transition at 1046 nm between two of these states [12]. Since this transition is estimated to be $\sim 10^4$ times weaker than the 637 nm ZPL, passage through the singlet states is essentially a dark process. As we will describe in section 2.2.1, passage through the singlet states is strongly spin-dependent. Therefore the spin state of the NV center can be detected through the spin-dependent photoluminescence rate which is used as the standard method for room-temperature readout of the spin state of the NV center.

Using the NV center spin as qubit

The energy spectrum of the electron spin of the NV center in the electronic ground state is described by the Hamiltonian

$$H_{\mathrm{NV}} = D_{\mathrm{GS}} S_z^2 + \gamma_e \mathbf{B} \cdot \mathbf{S} \tag{2.13}$$

where $\mathbf{S} = [S_x, S_y, S_z]$, the S_i are the Pauli spin operators, and $\gamma_e = 2.8$ MHz/G is the gyromagnetic ratio of an electron spin with total spin $S = 1$. The first term describes the zero-field splitting and the second term the Zeeman interaction with a magnetic field $\mathbf{B}$. The energy spectrum of Eq. (2.13) is shown in Fig. 2.4 as a function of a magnetic field applied along the NV symmetry axis. The zero-field degeneracy of the $m_s = \pm 1$ states is lifted by a magnetic field. If the energy separation between the $m_s = \pm 1$ is large enough so that this transition can be driven selectively means that the $m_s = 0$ and $m_s = -1$ levels form a pseudo spin-1/2 which we can use as a qubit.

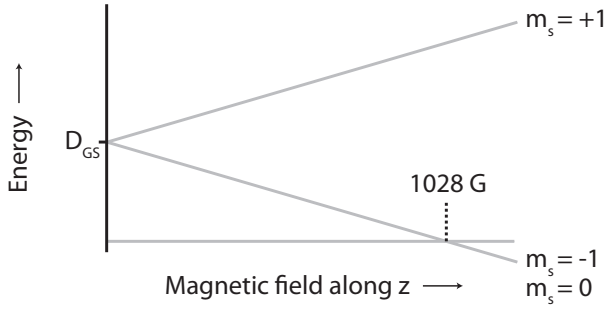

Figure 2.4: Energy spectrum of the NV center electron spin in a magnetic field applied along the symmetry axis of the NV center. The energies of the $m_s = \pm 1$ states shift with 2.8 MHz/G.

One of the most remarkable properties of the NV center is that its electron spin can be initialized and read out by off-resonant excitation, even at room tem-

perature. Together with full coherent control of its spins state the initialization and read out, make that most of the basic requirements for a qubit are found in the NV center. The mechanism responsible for optical spin polarization and readout will be explained below.

Due to a spin-dependent relaxation mechanism between electronic ground and excited state, the NV center electron spin polarizes into the $m_s = 0$ state under optical excitation. During optical cycling, spin-flips mainly occur through decay via the singlet states (Fig. 2.3b) [6, 11]. Decay from the excited state into the singlet states occurs primarily for the $m_s = \pm 1$ states, and decay from the singlet states into the electronic ground state occurs primarily into the $m_s = 0$ state. After just a few optical cycles the system therefore mainly occupies the $m_s = 0$ state. By following the optical excitation with a few microseconds of dark waiting time to allow deshelving of remaining population in the singlet states, the electron qubit is initialized in the $m_s = 0$ state with a typical spin polarization between 80% and 95% [11, 13].

The spin-dependent relaxation mechanism between electronic excited and ground state responsible for spin polarization also allows optical detection of the NV center spin state. Because the system is more likely to decay via the dark singlet states if it is in the $m_s = \pm 1$ states than if it is in the $m_s = 0$ state, the photoluminescence (PL) is spin-dependent and can be used to detect the spin state of the NV center. Fig. 2.5 depicts a optically detected magnetic resonance (ODMR) spectrum of a single NV center in small magnetic field ($B = 29$G). It clearly demonstrates how the detected PL decreases when microwaves are applied that are in resonance with the $m_s = 0$ to the $m_s = \pm 1$ transitions which induce population of the $m_s = \pm 1$ sublevels. The experimental details on how ESR and read out is achieved are explained in section 2.4. The three dips observed in the ESR spectrum of Fig. 2.5b are associated with hyperfine coupling to the ^{14}N nuclear spin of the NV center's own nitrogen atom. The ^{14}N isotope, the most common species (99.63% natural abundance), carries spin $I = 1$ which couples to the NV electronic spin. The energy spectrum can therefore be understood by analyzing the the Hamiltonian of the coupled system

$$H = H_{\mathrm{NV}} + PI_z^2 + \gamma_n \mathbf{B} \cdot \mathbf{I} + A_{||} S_z I_z + A_{\perp}(S_x I_x + S_y I_y) \tag{2.14}$$

Here, $P = 4.95$ MHz is the nuclear quadrupolar splitting, $\gamma_n = 0.30$ kHz/G is the nuclear gyromagnetic ratio, and $A_{||} = 2.16$ MHz and $A_{\perp} = 2.1$ MHz are the hyperfine coupling parameters.

The flip-flop terms (the terms containing $S_x I_x$ and $S_y I_y$) in Eq. (2.14) can be neglected as long as the applied field B_z is such that the electronic spin transitions are far off-resonant from the nuclear spin transitions. This is the case in the experiments described in this thesis, where the electron (nuclear) spin resonances in the electronic ground state are of order GHz (MHz). Terms in Eq. (2.14)

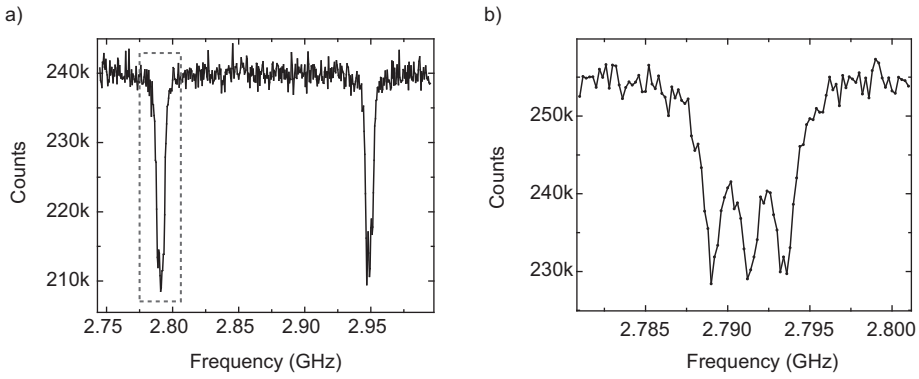

Figure 2.5: ODMR spectrum of an NV center in a field of $B_z = 29$ G. Plotted is the detected photoluminescence under continuous optical excitation as a function of the frequency of an applied microwave field. **a,** ODMR spectrum showing the two dips associated with the electron spin transitions from $m_s = 0$ to the $m_s = \pm 1$ states. **b,** Zoom-in on the $m_s = 0 \leftrightarrow m_s = -1$ ODMR dip of **a** showing the three dips associated with the three different spin states of the host ^{14}N nuclear spin.

containing only nuclear spin operators do not affect the electron spin transition frequencies. The three resonance frequencies observed in the ESR spectrum of Fig. 2.5 consequently differ by $A_{||}$.

2.2.2 Nitrogen impurities

Substitutional nitrogen impurities together with the NV center are the key players for all the experiments in this thesis. Each nitrogen defect has an unpaired electron ($S = 1/2$) and a nuclear spin ($I = 1$) from the ^{14}N atom. In Ib diamond nitrogen impurities are the dominant impurity species and form a bath of electron spins which shows interesting many-body dynamics. Perhaps the most interesting behavior results from the interplay between the nitrogen spin bath and a single NV center. This configuration is often called the central spin problem [14], which plays an important role in the study of decoherence and coherence protection of spins in the solid state. First, we discuss the physical properties of a single nitrogen defect which results in a rather rich level structure. Second, we will give a theoretical description of the spin bath formed by the nitrogen electron spin ensemble.

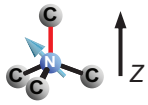

Figure 2.6: A single substitutional nitrogen defect in diamond. Its symmetry is broken by the static Jahn-Teller effect, which shortens one of the four N-C bonds along one of the four ⟨111⟩ directions (indicated red).

Level structure

Substitutional nitrogen impurities in diamond (also called P1 centers in literature) give rise to a deep donor levels well below the conduction band of diamond, with optical and thermal ionization energies of 2.2 eV and 1.7 eV respectively [15]. The unpaired electron ($S = 1/2$) of the nitrogen atom is responsible for a paramagnetic resonance signal which was first observed by Smith *et al.* [16]. Nitrogen impurities exhibit trigonal symmetry due to a static Jahn-Teller distortion (Fig. 2.6 which elongates one of the four N-C bonds. The unpaired electron predominantly occupies an antibonding orbital at the elongated bond, which is predominantly of s and p-type character [17].

A strong anisotropic hyperfine interaction exists between the electron spin and nuclear spin ($I = 1$) of the host ^{14}N atom (99.6% abundance). The hyperfine interaction of the nitrogen impurity is given by [16]

$$\hat{H}_{\text{int}} = \hat{A}_{||}\hat{S}_Z\hat{I}_Z + A_{\perp}(\hat{S}_X\hat{I}_X + \hat{S}_Y\hat{I}_Y) - P\hat{I}_Z^2 \tag{2.15}$$

with $A_{||} = 114$ MHz, $A_{\perp} = 86$ MHz and $P = 4.2$ MHz and $\hat{S}$ and $\hat{I}$ are the operators for the electron and nuclear spin respectively of the nitrogen impurity. The direction of the anisotropy (z) axis is set by the JT distortion axis, which is randomly oriented along one of the four ⟨111⟩ directions (Fig. 2.6). Similarly if the carbon atom of the N-C bond is ^{13}C (1.1% abundance), which has nuclear spin ($S = 1/2$), it too will interact with the electron spin. The ^{13}C hyperfine parameters are [16] $A'_{||} = 341.2$ MHz and $A'_{\perp} = 141.6$ MHz. Hyperfine coupling strength with ^{13}C located at all other sites is at most one order of magnitude smaller then the aforementioned values. Much information can be extracted from the hyperfine interaction about the distribution of the wavefunction Ψ_e of the donor electron. As the largest hyperfine parameters are found for the N and C atom of the N-C bond indicates that the majority of Ψ_e is shared mostly between those sites.

As is explained in section 2.1.4, the s character of the oprbital wavefunction is responsible for the isotropic part of the hyperfine interaction and the p character is responsible for the anisotropy in the hyperfine interaction. Given the trigonal

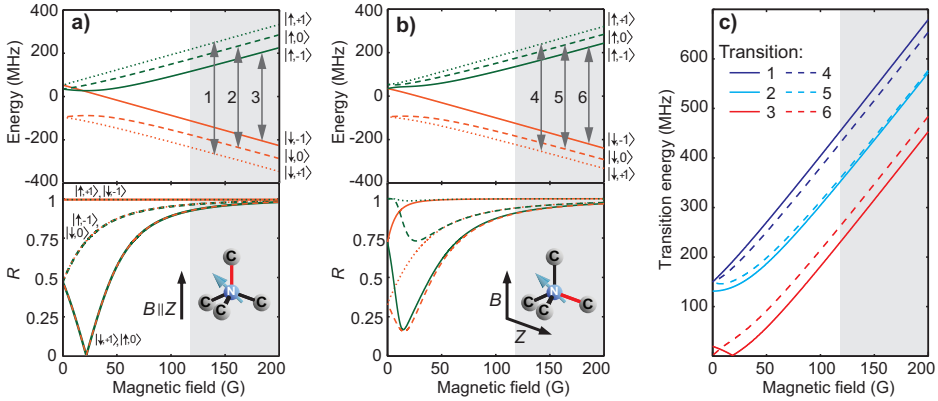

Figure 2.7: Magnetic field dependence of the energy levels of the nitrogen impurity defect center for a field applied along one of the four ⟨111⟩ directions. **a,** Energy levels (upper panel) and spin mixing (lower panel, see text) for the eigenstates of a nitrogen impurity with the JT axis (red, see inset) aligned with the externally applied field. At low magnetic field ($B < 100$ G) the eigenstates are entangled states of the electron and nuclear spin (mixtures are indicated in the lower panel). Gray arrows indicate the allowed transitions for $B > 100$ G which drive the electron spin and preserve the nuclear spin state. **b,** Same as in **a**, but then for a nitrogen impurity with its JT axis aligned with one of the three other equivalent ⟨111⟩ directions. **c** Combined energy spectrum of an ensemble of P1 centers.

symmetry of defect the relative contributions of the p and s part can be estimated by [17]

$$A_{||} = O + 2P \tag{2.16}$$
$$A_{\perp} = O - P \tag{2.17}$$

with P representing the p type contribution to the hyperfine interaction and O is the contribution of the s character of Ψ_e. Plugging the values for $A_{||}$ and $A_{\perp}$ into Eq. (2.17) shows that the majority of the hyperfine interaction for both ^{13}C and ^{14}N originates from the contact term. From O the overlap of the electron with the nuclear spin can be directly calculated since

$$O = \frac{2}{3}\mu_0\gamma_S\gamma_I\hbar^2|\Psi_e(0)|^2 \tag{2.18}$$

whereγ_S and γ_I are the gyromagnetic ratios for the electron en nuclear spin respectively.

In Fig. 2.7 the magnetic field dependence of the energy levels of the nitrogen defect is depicted. At low magnetic field the states are entangled states of the

electron and nuclear spin. The lowest energy states are At high magnetic field the eigenstates of the nitrogen impurity consist of pure electron spin and nuclear spin states and $S_z = +1/2, -1/2$ and $I_z = +1, 0, -1$ can be considered to be good quantum numbers for the electron and nuclear spin respectively. The transitions that can be driven most efficiently using RF irradiation are the ones which involve electron spin transitions (indicated by the gray arrows in Fig. 2.7. To get a feeling for how well the eigenstates are defined by the electron spin quantum numbers $S_z = +1/2, -1/2$ the quantity $R = \sqrt{\langle S_x \rangle^2 + \langle S_y \rangle^2 + \langle S_z \rangle^2}$ is plotted in the lower panels of Fig. 2.7 for all the levels as a function of the magnetic field. The experiments described in this thesis are all performed at fields $B_{\text{ext}} > 100$ G where $R > 0.9$. In Ib diamond the local concentration of nitrogen impurities is between 1 and 200 ppm. In these samples the bath of nitrogen electron spins forms the main contribution to the magnetic environment. As we show in chapter 6 we can identify several spectral sub-ensembles, or groups, distinguished by their JT orientation and nuclear spin projection for $B_{\text{ext}} > 100$ G.

The dipolar interactions between the spins belonging to the same spectral group, as well as the off-resonant dipolar interactions between spins from different spectral groups induces dynamics on short < 50 μs timescales. The activation energy for the reorientation of the JT-axis is ~ 0.7 eV [17]. At room temperature both the reorientation of the JT-axis [18] and spin-lattice relaxation times range from milliseconds to hours for the electron spins [19] and nuclear spins [20] respectively. In section 2.3 we will explain how all these processes and their timescales influence the coherence of single NV centers.

2.2.3 ^{13}C spins

The nuclear spin of ^{13}C is a paramagnetic impurity that is present in most diamond samples due to its 1.1% natural abundance. In pure diamonds where nitrogen concentrations are in the $1 <$ ppb regime the magnetic environment can be considered to be fully determined by ^{13}C nuclear spins. NV centers in such samples demonstrate excellent coherence with line widths typically 150 kHz and coherence times $T_2 \sim 300$ μs [21]. This can be reduced dramatically in isotopically engineered diamonds with 0.3% ^{13}C abundance. In such samples line widths and coherence times are reduced to 55 kHz and 1.8 ms, respectively [22].

2.3 Quantum dynamics of spins in diamond

In this section we will describe the decoherence resulting from the interaction of a single quantum system with a dynamic environment. The two most well known models applicable in solid state systems are the spin-boson model [23], which describes a spin coupled to a bath of bosons and the central spin problem [14]

where a single central spin is coupled to an ensemble, or bath, of spins. The central spin problem is found in many solid state systems besides diamond [24], such as as in quantum dots [25] and phosphorous donors in silicon [26]. It is an important model in the context of quantum information with spin qubits. Furthermore, studying the central spin problem is of fundamental importance as decoherence plays an important role in theories that describe how the classical world emerges from interacting quantum systems [27].

In diamond, the NV center takes the role as central spin (or qubit) and the nitrogen electron spins forms the quantum environment or spin bath. In this thesis we mainly study NV centers in Ib diamonds with high (10-100 ppm) nitrogen content. Although these nitrogen concentrations are still roughly two orders of magnitude lower than the ^{13}C nuclear spin concentration (1.1 % natural abundance), the magnetic environment for NV centers in such samples is fully dominated by the electron spins belonging to nearby nitrogen defects. This is a direct consequence of the large gyromagnetic ratio for the electrons ($\gamma_e/2\pi = 2.8$ MHz/G) compared to that for ^{13}C nuclear spins ($\gamma_{^{13}\mathrm{C}}/2\pi = 1.07$ kHz/G).

An important consequence of the large gyromagnetic ratio for bath spins is that the internal bath coupling strengths are similar to the coupling strength between a bath spin and an NV, for which $\gamma_{\mathrm{NV}} \approx \gamma_e$. This means that for each bath spin the coupling to the single NV spin is completely overshadowed by the coupling to all the other bath spins. There is therefore no back-action of the NV spin to the spin bath[2].

The decoherence the spin bath induces for the NV spin is then the result of the fluctuating dipolar field $\delta b_z(t)$ at the site of the NV spin, which is generated by the statistical polarization of nearby bath spins. Having no backaction on the spin bath by the NV spin, means that a single NV center can also be regarded as a non-invasive probe of its own magnetic environment (see chapter 6). The next section explains the model for the dynamics of $\delta b_z(t)$ and how this results in decoherence of the central spin.

2.3.1 Dynamics of the nitrogen electron spin bath

The Hamiltonian of the dipolarly coupled spin bath is given by

$$H_B = \sum_{k,l} H_{\mathrm{N}\leftrightarrow\mathrm{N},kl} + \sum_k H_{0,k} \tag{2.19}$$

Here, the internal Hamiltonian of each bath spin $H_{0,k}$ contains the Zeeman term and local hyperfine interaction with the ^{14}N nuclear spin (see Eq. (2.15)) and

[2]The opposite regime is found for a ^{13}C nuclear spin bath [21], where the coupling to the central spin dominates the intra-bath coupling strengths

$H_{\mathrm{N}\leftrightarrow\mathrm{N},kl}$ is the intra-bath coupling term [2]

$$H_{\mathrm{N}\leftrightarrow\mathrm{N},kl} = C_{kl}[S_{z,k}S_{z,l} - \frac{1}{4}(S_{+,k}S_{-,l} + S_{-,k}S_{+,l})] \tag{2.20}$$

with $C_{kl} = \mu_0\gamma_e^2\hbar^2/|\mathbf{r}_{kl}|^3(1-3\cos^2(\theta_{kl}))$, $\mathbf{r}_{kl} = \mathbf{r}_k - \mathbf{r}_l$ is the vector connecting the k-th bath spin to the l-th bath spin and θ_{kl} is the angle this vector makes with the z-axis which is set by the external field if $B > 100G$. The flip-flop terms (i.e. terms that contain S_-S_+ in Eq. (2.20) only commute with $H_{0,k}$ and $H_{0,l}$ when bath spins k and l belong to the same spectral group (see chapter 6), meaning that either they have equivalent Jahn-Teller orientations or when the ^{14}N nuclear spins of both bath spins have nuclear spin projection $m_I = 0$. For all other combinations these terms induce transtions between levels which do not conserve energy and can be neglected. This means that the local hyperfine interaction suppresses the dynamics. As is shown in the next section this slows down the local environment for a single NV spin and typical dephasing times are much shorter then its coherence times.

2.3.2 Decoherence of a single NV spin interacting with an electron spin bath

Spin bath dynamics

At moderate external fields ($B < 300$ G) the NV spin level splitting between $m_s = 0$ and $m_s = -1$ is > 2 GHz (Fig. 2.4). These are used as the qubit levels $|0\rangle$ and $|1\rangle$ respectively in all our experiments. Bath spins have level splittings < 1 GHz (Fig. 2.7). The detuning therefore greatly exceeds the typical coupling strengths between the NV spin and nearby bath spins, which are at most several MHz. Flip-flops between the NV spin and bath spins are therefore forbidden and the interaction between the NV spin and the spin bath is [28]

$$H_{\mathrm{NV}\leftrightarrow\mathrm{N}} = S_{z,\mathrm{NV}}\sum_k a_k S_{z,k} \tag{2.21}$$

where we take $S_{z,NV}$ the pseudo-spin 1/2 operator for the NV center for the $m_s = 0$ and $m_s = -1$ levels and where coupling constants are given by $a_k = \mu_0\gamma_e^2\hbar^2[1-3\cos^2(\theta)]/4\pi r_k^3$ with r_k the length of the vector $\mathbf{r}_k$ connecting the NV spin and k-th bath spin. The angle θ is the angle between the external field (which is oriented along the NV symmetry axis) and $\mathbf{r}_k$. The prefactor a_k is of order 1 MHz for $r_k = 5$ nm, which is roughly the average nearest-neighbour N-N or N-NV distance in diamond with 100 ppm nitrogen content.

Each bath spin k shifts the $m_s = 0 \leftrightarrow m_s = -1$ level splitting up or down by the amount $a_k/2$, depending whether the k-th bath spin is pointing up or down.

The decoherence of the NV spin is the result of the time-dependent fluctuations in the level splittings, which originates from the reorientation of bath spins. There are many bath spins that contribute significantly to the fluctuation in the level splitting so we can apply the central limit theorem and model the fluctuation as a normally distributed random value with zero mean, and variance given by

$$b^2 = \frac{1}{4}\sum_k a_k^2. \tag{2.22}$$

For Ib diamond with nitrogen contents ranging from 10-100 ppm typical values for b range from 0.4-4 MHz [20]. The self- and interaction Hamiltonians combined give the Hamiltonian for the complete central spin system

$$H_{\text{tot}} = H_{\text{NV}} + H_{\text{NV}\leftrightarrow\text{N}} + H_B \tag{2.23}$$

with H_{NV} given by Eq. (2.13). The reorientation of bath spins is generated by the internal Hamiltonian of the spin bath H_B. The influence of the spin bath on the NV spin can be calculated by transforming to the interaction representation [28]

$$H_{\text{sys}} = H_{\text{NV}} + S_{z,\text{NV}}\delta\hat{b}_z(t) + H_B \tag{2.24}$$

where $\delta\hat{b}_z(t) = \exp^{iH_Bt}\sum_k a_k S_{z,k}\exp^{-iH_Bt}$. All the influence of the spin bath on the NV spin is now captured by $\delta\hat{b}_z(t)$. The last term H_B in Eq. (2.24) can therefore be disregarded since we are only interested in the NV spin.

Following refs. [28, 29] we replace the operator $\delta\hat{b}_z(t)$ by the z-component of a random dipolar field $\delta b_z(t)$. The time dependence of $\delta b_z(t)$, which is generated by the flip-flops between bath spins, is highly complex and results from the many-body dynamics of the spin bath. To a good approximation, however, the process can be regarded as a stochastic process in which flip-flops occur randomly with some probability. This probability is fixed in time, since there is negligible back action of the NV spin on the bath spins and intra-bath couplings do not change over time (bath spins do not change their location in the diamond lattice). The fluctuations in the dipolar field $\delta b_z(t)$ therefore resembles a Markovian process, which is Gaussian by virtue of the central limit theorem, with variance given by Eq. (2.22). Furthermore, $\delta b_z(t)$ has zero mean for all times, which means that the process is also stationary.

A process which is stationary, Markovian and Gaussian is by definition a Ornstein-Uhlenbeck process [30] with correlation function

$$C(t_0, t_0+t) = \langle \delta b_z(t_0)\delta b_z(t_0+t)\rangle = b^2\exp -|t|/\tau_C \tag{2.25}$$

with τ_C the correlation time. At low frequencies the spin bath can therefore be modeled as classical noise with a Lorentzian power spectral density with its cutoff

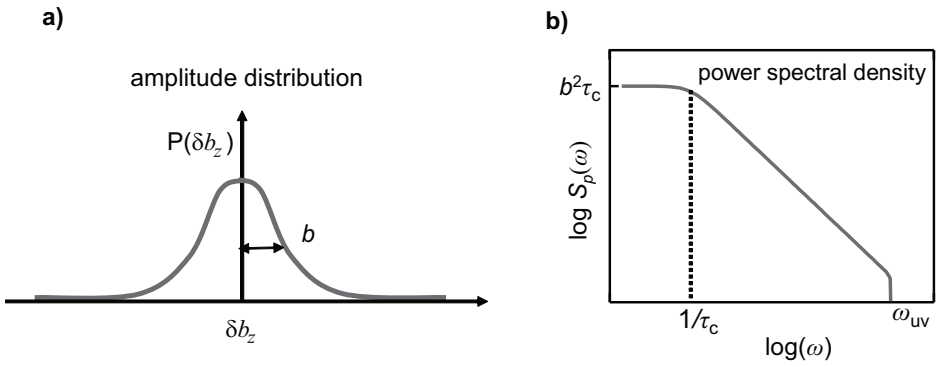

Figure 2.8: Classical model for the spin bath. **a,** Distribution of the dipolar field generated by the spin bath at the location of a single NV spin. The distribution is Gaussian with variance b^2. **b,** Power spectral density of the spin bath with a hard cut-off at ω_{uv}.

frequency at $f = 1/(2\pi\tau_C)$ (Fig. 2.8). At very high frequencies the spectrum will be cut-off by ω_{uv} since highest spectral component is determined by the maximum flip flop rate. The highest rates occur for bath spins located only a few lattice sites away from each other, giving coupling strengths in the hundreds of MHz. This model has been previously applied successfully to describe free induction and spin-echo decay in solid state spin systems [29, 31] and, as we will show in chapter 4 and 6, is also very useful in explaining experiments involving more complicated pulse sequences.

The correlation time τ_C is determined by the flip-flop rate $R = 1/\tau_C$. The flips-flop rate between bath spins is suppressed due to the local hyperfine interaction with the N nucleus, which limits the flip-flops to occur only between bath spins from the same spectral group. However, all bath spins surrounding a single bath spin k, including those from other spectral groups, contribute to its inhomogeneous broadening (see Ch. 6). In the regime where the average transition rate $T = \langle C_{kl}^2 \rangle / 16$ Eq. (2.20) is much smaller than the ensemble inhomogeneous line width Δ_e, the flip-flop rate R is given by [31]

$$R = \frac{\pi}{9} \frac{\langle C_{kl}^2 \rangle}{16 \Delta_e} \tag{2.26}$$

A rough estimate for C_{kl} for bath spins belonging to spectral group III which have ^{14}N nuclear spin projection $I = 0$ is given by $C_{kl} = \Delta_e/\sqrt{3}$ (Ch. 6). In a 100 ppm sample where $\Delta_e \approx 4$ MHz the correlation time is estimated to be a few tens of microseconds. The electron spin bath of nitrogen spins is thus

expected to be a quasistatic environment for the NV spin since $b >> R$. This is directly evidenced by the shapes of the decays during free evolution, spin echo and dynamical decoupling sequences [29] (see Ch. 4).

NV spin decoherence

Decoherence results from either energy relaxation where there is energy transfer between the qubit and its environment or dephasing which is an energy conserving process. Energy relaxation and dephasing are also called longitudinal and transverse relaxation respectively in literature. The origin of these terms becomes clear when we visualize what happens to a spin which is subject to decoherence on the Bloch sphere. Energy relaxation is any processes in which a spin exchanges energy with its environment, resulting in a change of the r_z component of the state vector $\overrightarrow{r}$ and a reduction of the transverse $r_{x,y}$ components. Dephasing always only reduces the $r_{x,y}$ components.

The relaxation process of the NV center arises from the coupling to lattice phonons via the spin-orbit interaction. Another term for the energy relaxation of spins is therefore also called spin-lattice relaxation. Note that the energy relaxation can either take ρ to a pure state (its ground state with $r_z = +1$) when $k_B T$ is less than the level splitting between $|\uparrow\rangle$ and $|\downarrow\rangle$, since then the qubit can only give its energy to the environment and not vice versa. At room temperature the level splitting is generally much lower and energy transfer occurs in both directions. In that case ρ decays to a mixed state (i.e. $r_z = 0$). Spin-orbit coupling strengths for both NV and N centers is small since for both, the electronic spin g-factors are isotropic and close to that of free electrons [17]. Both NV and N centers therefore have spin-lattice relaxation times $T_1 > 1$ ms at room temperature and even become seconds at low temperature [19, 32]. Decoherence of NV spins is therefore completely dominated by the dephasing induced by the dipolar coupling to the spin bath.

As we discussed in the previous sections the spin bath around an NV spin can be modeled as a quasistatic random classical magnetic field $\delta b_z(t)$ with a Gaussian distribution with width b. The pure dephasing can be measured using the Ramsey pulse sequence $\pi/2 - \tau - \pi/2$ (Fig. 2.9). The experiment starts by initializing the qubit along the z-axis in $\rho_0 = |0\rangle\langle 0|$. For an NV spin this is done by preparing it in the $m_s = 0$ state by optical pumping (see section 2.4.1). The first $\pi/2$ pulse applies the operator $R_y(\pi/2)$ which is a rotation around the y axis by a $\pi/2$ angle and which creates a superposition along the x axis in the Bloch sphere. During the free evolution time τ the superposition is let to precess freely. The random field $\delta b_z(t)$ causes a precession of the state vector around the z axis described by the evolution operator

$$\delta Z(\tau) = e^{-i \int_0^\tau \delta b_z(t) S_z dt} \tag{2.27}$$

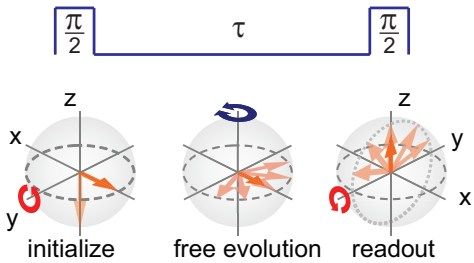

Figure 2.9: Ramsey experiment. A fist $\pi/2$ pulse initializes the state vector along the x-axis followed by a period of free evolution. During this free evolution period the NV spin picks up a random phase which is determined by $\delta b_z(t)$ which is different for every experimental run (indicated by the spread in evolution of the state vector). The final x-component of the state vector is then determined by a final $\pi/2$ rotation. After this the z projection is measured using the optical spin read out.

After this another $\pi/2$ pulse is applied which rotates the x-component of the state back onto the z-axis. The total evolution of the whole sequence is then $U(\tau) = R_y(\pi/2)\delta Z(\tau)R_y(\pi/2)$. After this the optical readout is used to determine the z-projection $\langle S_z \rangle$ of the state vector (see section 2.4.1). In order to build statistics the experiment is repeated many ($\sim 10^6$) times so the signal will be the average over many realizations of $\delta b_z(t)$

$$\langle S_z \rangle = \left\langle \mathrm{Tr}\left[S_z U(\tau)\rho_0 U^\dagger(\tau)\right] \right\rangle = -\left\langle \exp\left(i \int_0^\tau \delta b_z(t)\, dt \right) \right\rangle \tag{2.28}$$

where $\langle \cdots \rangle$ denotes the averaging. Since for an electron spin bath $\delta b_z(t)$ is generated by a Gaussian process, eq. (2.28) can be calculated explicitly [33]

$$\langle S_z \rangle = -e^{-\chi(\tau)} \tag{2.29}$$

The minus sign results from the two $\pi/2$ rotations. The exponent $\chi(\tau)$ is determined by the correlation function $C(t_0, t) = \langle \delta b_z(t_0)\delta b_z(t) \rangle$ and a time-domain filter function $f_R(t)$ belonging to the Ramsey sequence [34]

$$\chi(\tau) = \frac{1}{2} \int_0^\tau dt \int_0^\tau dt_0\; C(t_0, t) f_R(t_0) f_R(t) \tag{2.30}$$

For a Ramsey sequence with total free evolution time τ the filter function $f_\mathrm{R}(t) = u(t) - u(t-\tau)$ with $u(t)$ the unit-step function.

Eq. (2.29) can also be written in the frequency domain by using the fact that the power spectral density of $\delta b_z(t)$ is given by $S_C(\omega) = \int_{-\infty}^{+\infty} dt\ e^{-i\omega t} C(t_0, t_0 + t)$ and that (2.29) represents a convolution. The exponent $\chi(\tau)$ calculated in the frequency domain is then

$$\chi(\tau) = \frac{2}{\pi} \int_0^{\infty} d\omega\ S_C(\omega)\, |F(\omega)|^2 \tag{2.31}$$

where $F(\omega)$ is the Fourier transform of the filter function. The frequency domain counterpart of $f_{\mathrm{R}}(t)$ is $F_{\mathrm{R}}(\omega) = 1/i\omega\,[1 - \exp(i\omega\tau)]$.

Using the correlation function 2.25 from the classical model for the electron spin bath we get for the decay during free evolution

$$\langle S_z \rangle = -\exp\left[-\frac{b^2}{R^2}(R\tau + e^{-R\tau} - 1)\right]. \tag{2.32}$$

If $b < R$ (i.e. a fast bath) the Ramsey signal will decay exponentially with time-constant $T_2^* = R/(b^2)$. Since the line shape in the frequency domain is given by the Fourier transform of the time-domain decay shape this will result in a Lorentzian line shape with full-width-half-maximum (FWHM) $\Delta = 1/\pi T_2^*$. This linewidth is a factor b/R smaller then what one would expect from the Gaussian distribution of $\delta b_z(t)$ which has width b. This phenomenon is called motional narrowing in literature [2] and is the result of the time integral of $b_z(t)$ approaching zero for $\tau >> 1/R$.

In the opposite regime where the bath is slow $R\tau << 1$ and $b > R$ the first order terms in (2.32) cancel and second order terms become the leading terms. In this case the decay is $\langle S_z \rangle = -\exp\left(-b^2\tau^2/2\right)$. If we take the Fourier transform to determine the linewidth in frequency $\Delta \simeq b/\pi$ it indeed corresponds to the distribution of $\delta b_z(t)$. This is also expected since now the dipolar field $\delta b_z(t)$ is quasistatic (i.e. it does not change during the measurement, but is different each time a measurement is repeated).

The filter function appearing in Eqs. (2.30) and (2.31) provides a convenient tool to calculate the signal for any pulse sequence such as the Hahn-echo, or spin echo (SE) sequence [35] $\pi/2 - \tau/2 - \pi - \tau/2 - \pi/2$ (Fig. 2.10). The sequence works as follows. As in the Ramsey sequence, the state vector is rotated in the xy-plane of the Bloch sphere by the first $\pi/2$ pulse. After this a period of free evolution of length $\tau/2$ follows during which the spin starts to precess in the random field $\delta b_z(t)$. A π pulse is then used to flip the spin by rotating it around the y-axis by 180^{o} (hence the name π-pulse). During the second free evolution period the spin will continue to precess. If $\delta b_z(t)$ remains constant during the whole sequence the

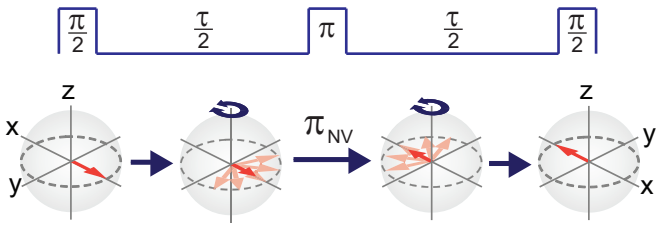

Figure 2.10: Spin echo experiment. As in the Ramsey experiment a fist $\pi/2$ pulse is used to initialize the state vector along the x-axis. This is followed by a first initial period of free evolution $\tau/2$ during which a random phase accumulates. A π pulse half way during the sequence is used to rotate the state vector around the y axis by 180°. The evolution continues and if during the total free evolution time τ $\delta b_z(t)$ does not change the statevector will end up along the x-axis irrespective of the exact value of $\delta b_z(t)$. The final $\pi/2$ pulse is used for the read out of the x-component of the state vector the same way as in the Ramsey experiment.

spin will be aligned again along the x-axis after the second period of free evolution and an echo is formed. This refocusing of the state vector is independent of the value of $\delta b_z(t)$ as long as it does not change during the sequence. Finally, the last $\pi/2$ pulse rotates the x-component of the state vector back to the z-axis which followed by the read out.

Another way of looking at the spin echo sequence is by moving to the reference frame which is turned up-side-down whenever a π-pulse is applied. In this so-called toggling frame the spin is no longer being flipped but it is the random field $\delta b_z(t)$ which changes sign whenever a π-pulse is applied. We can therefore write for the filter function of the SE sequence $f_{\mathrm{SE}} = u(t) - 2u(t-\tau/2) + u(t-\tau)$. Plugging this into (2.29) gives the signal for the SE dacay

$$\langle S_z \rangle = \exp\left[-b^2/R^2\big(\, R\tau + 4e^{-R\tau} - e^{-R\tau} - 3\,\big)\right] \tag{2.33}$$

The signal is now no longer negative because of the extra π-pulse in the SE sequence. Again, looking at the case of fast bath where $R > b$ we see that the spin echo decays with the same rate as the Ramsey signal. This reflects the fact that for this situation there is no correlation between $\delta b_z(t)$ during the first free evolution period and the second and the refocussing effect of the π-pulse is diminished.

For a slow bath, where $b > R$, we only have a signal at $\tau << 1/R$. In that case all terms in the exponent up to the second order cancel and the signal decays as $\langle S_z \rangle = \exp\left(-b^2 R\tau^3/12\right)$ and so we have for the spin-echo decay time, or coherence time, $T_2 = [12/(b^2 R)]^{1/3}$. The decay is slowed down dramatically at times $\tau << T_2$ which means that we can expect state fidelities to be high in

this regime.

Dynamical decoupling

It would be convenient if this favorable short timescale behavior, on which there is such a small influence of decoherence, could be extended. One natural way is to just apply more π-pulses. A sequence with N pulses which are applied at times $\delta_j \tau$ with $0 < \delta_j < 1$ results in a time-domain filterfunction

$$f(t) = u(t) + (-1)^N + 1u(t-\tau) + 2\sum_{j=1}^{N}(-1)^j u(t-\delta_j\tau) \tag{2.34}$$

which in the freqeuncy domain becomes

$$F(\omega) = \frac{1}{i\omega}\left(1 + (-1)^N + 1e^{i\omega\tau} + 2\sum_{j=1}^{N}(-1)^j e^{i\omega\delta_j\tau}\right) \tag{2.35}$$

By applying N cycles of the echo sequence each of which has length τ/N, we get the so-called Carr-Purcell (CP) sequence $\pi/2 - [\tau/2N - \pi - \tau/2N]^N - \pi/2$ and for which $\delta_j = (2j-1)/2N$. Sequences with CP timing of the π-pulses can indeed be used to extend the coherence time of a single NV spin as we show in Ch. 4.

From the shape of the spin echo decay we can estimate what the new decay shape will be when we apply the N-pulse CP sequence. For short τ the spin refocusses along the x-axis after each echo cycle. The next cycle will then be a refocussed echo of the previous echo. We therefore expect the amplitude of the echo to decrease exponentially with N according to $\sim \exp\left[-N\left(\tau/T_2\right)^3\right]$. Rewriting this in terms of the total free evolution time $t_{fe} = N\tau$ we get for the decay $\sim \exp\left[-t_{fe}^3/\left(N^2T_2^3\right)\right]$ and we get for the new $1/e$ coherence decay time $T_{1/e} = N^{2/3}T_2$. A more rigorous proof of this scaling behavior is given in Ch. 4 by using the filter function approach. There we also show that this scaling continues even in the case that the total free evolution time exceeds the correlation time of the spin bath.

The scaling can in principle be generalized to any spin echo decay shape for which $\exp\left[-\left(\tau/T_2\right)^k\right]$ where an exponent $k \neq 3$ can be the result from a spectrum other than a Lorentzian spectrum. For instance classical noise can have a power-law spectrum $S(\omega) \sim \omega^{-\beta}$. In this case the coherence time characterized by the $1/e$ time of the coherence decay curves is $T_{1/e} = N^{1-1/k}T_2$ and there is a simple relation between the power of the exponent k of the SE decay and the power β of the noise spectrum which is given by $\beta = k - 1$ [36]. In cases

where signal quality is too low to determine the exact decay shape of the Hahn-echo dynamical decoupling can be used to estimate β. Aside from prolonging qubit coherence, dynamical decoupling can be used to extract information of the noise sources that couple to a qubit. Another practical application of dynamical decoupling sequences is in magnetometry. In Ch. 5 we show how flipping a single spin in resonance with an externally applied AC magnetic field dramatically improves the sensitivity of spin-based magnetometers. In addition to diamond, dynamical decoupling has been implemented in a variety of systems, such as trapped ions [37], superconducting qubits [38], rare-earth ions [39], quantum dots [40] and donors in silicon [41], in the context of quantum information and metrology.

There are many other types of sequences that can be constructed and which are not necessarily periodic in the timing of the pulses. One example is the Uhrig DD sequence [42]. This sequence is efficient with Ohmic spectra or in cases where there is a hard high-frequency cut-off in the spectrum [37]. In the case of the electron spin bath the power spectrum decays with ω^{-2}, which can be considered soft. The hard cut-off of the electron spin bath is at such a high frequency ($\sim$ 1 GHz) and it is impossible to apply π-pulses on such short timescales. The periodic sequences CP therefore work best for a bath of electron spins and we will therefore not focus on aperiodic sequences in this thesis.

2.4 Experimental techniques

This section gives an overview of the experimental techniques involved in the control and read out of the spin sates of single NV centers. The optical detection is discussed first[3]. The rest of this section discusses how quantum control of the spin states is achieved using microwave magnetic fields and how the performance of processes is characterized using quantum process tomography (QPT).

2.4.1 Detecting single NV centers

The 637 nm ZPL of the NV center is accompanied by a broad phonon sideband (PSB), both in emission and absorption (Fig. 2.3a). The PSB is associated with transitions between electronic ground and excited state which, in addition to the emission/absorption of a photon, involve the excitation/absorption of a (local) vibration of the NV center [43]. These vibronic states, which have short $\ll$ 1ps lifetimes corresponding to tens of nanometer spectral widths, give the PSB its characteristic spectral shape (Fig. 2.12a).

[3]The description of the detection of single NV centers is adapted from [5]

The PSB allows efficient excitation of the NV center by off-resonant laser light at e.g. 532 nm. The short optical lifetime ($\sim$ 12 ns in bulk diamond), in combination with a high quantum efficiency for radiative relaxation ($\eta \sim 1$), allows relatively straightforward detection of the photoluminescence of single NV centers. NV centers were first observed individually in 1997 by Gruber *et al.* using a confocal microscope [44].

Nowadays, the confocal microscope has become the standard tool to optically isolate and study single NV centers. Fig. 2.11 schematically shows one of the confocal microscopes built for the experiments described in this thesis. NV centers are excited by a 532 nm laser which is focused to a diffraction limited spot by a high numerical aperture (NA) objective (typically NA=0.95). Photoluminescence originating from the sample is separated from the excitation light by a dichroic mirror and optical filters. A photoluminescence map of a sample is made by scanning the position of the excitation laser across the sample and detecting the position-dependent photoluminescence using avalanche photodiodes. A confocal microscope employs a pinhole to increase the signal-to-background ratio of the detected photoluminescence by blocking out-of-focus light.

The diffraction limit limits the spatial resolution of a confocal microscope to the order of a wavelength. NV centers can therefore only be optically isolated if the distance to neighbouring NV centers is large enough [44]. In our bulk diamond samples the typical seperation between NV centers is a few μm and the spot size sufficiently small < 400 nm, allowing us to address single centers.

That the photoluminescence detected from a diffraction-limited spot originates from a *single* NV center, can be checked if the statistics of the photoluminescence corresponds to that of a single photon emitter. A single photon emitter emits only one photon when it decays from the excited state to the ground state. This single photon nature can be revealed by measuring the second order autocorrelation function $g^2(\tau)$ of the emitted photoluminescence, defined as

$$g^2(\tau) = \frac{\langle I(0)I(\tau)\rangle}{\langle I^2(t)\rangle} \tag{2.36}$$

where $I(t)$ is the detected photoluminescence intensity at a time t.

For large time differences there is no correlation in the emitted photoluminescence, so $g^2(\tau \to \infty) = 1$. However, a single photon emitter will have an anti-bunching dip in its autocorrelation function at zero time difference ($g^2(0) = 0$) because two photons are never emitted at the same time. Fig. 2.12b shows a measurement of the autocorrelation function of NV center photoluminescence. The anti-bunched nature of single NV center emission was first observed by Kurtsiefer et al. [45].

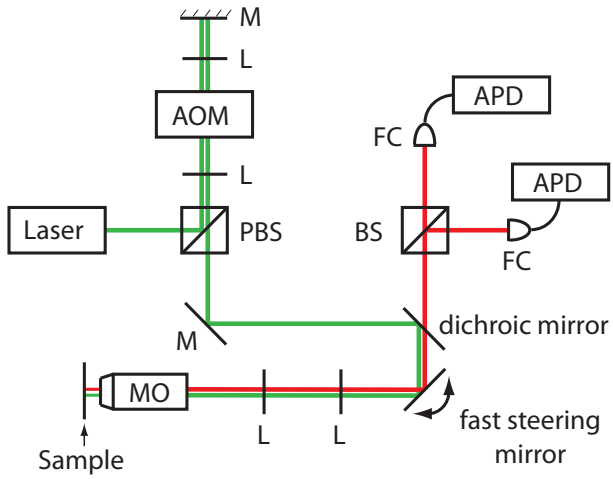

Figure 2.11: Schematic of the confocal microscope used to study single NV centers. A 532 nm laser (Coherent Compass 315M, frequency doubled Nd:YAG) is used for excitation. An acousto-optical modulator (AOM, Crystal Technologies 3200-121), in double-pass configuration to increase the extinction ratio to about 60 dB, can be used to create laser pulses with a risetime of about 10 ns. A fast steering mirror (FSM, Newport FSM-300-01) is used to scan the laser over the sample. Two lenses image the FSM onto the back focal plane of a microscope objective (MO). The objective (NA=0.95, Olympus MplanApo50x) focuses the laser to a diffraction limited spot of about 500 nm. The same microscope objective collects the photoluminescence. The excitation light is separated from the photoluminescence by a dichroic mirror and further suppressed by an optical filter. The photoluminescence is focused onto the core of an optical single mode fiber by a fiber coupler (fc) and detected using an avalanche photodiode (APD, Perkin & Elmer SPCM-AQR-14-FC). The fiber core acts as the confocal detection pinhole. For samples with very low background fluorescence, the fiber is replaced by a multimode fiber to increase collection efficiency. The beamsplitter (BS) is only used for antibunching measurements and is usually taken out of the beam path.

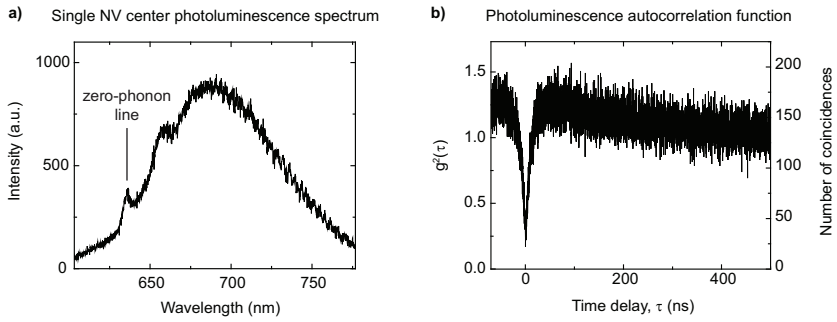

Figure 2.12: a, Room temperature photoluminescence spectrum of a single NV center. The spectrum is characterized by the zero-phonon line around 637 nm, which is accompanied by a broad phonon sideband. **b,** Autocorrelation function of single NV center luminescence, measured by splitting the photoluminescence to two detectors in a Hahnbury-Brown-Twiss setup.

2.4.2 Setup for quantum control

As explained in section 2.1.1 spins can be controlled with pulsed oscillating magnetic fields. The challenge in quantum control is to achieve high control fidelities. The characterization of quantum control pulses is the subject of chapter 3. In this section provides a brief overview of the origin of pulse errors and the measures taken to prevent them.

There are several effects that can limit control fidelity. The first is inhomogeneous broadening and local hyperfine interaction with the nitrogen nucleus which causes the transition frequency of the NV spin to vary from one measurement shot to another. For pulse sequences that are longer than the bath correlation time τ_C, the transition frequency can even change within one measurement. We therefore need π pulses which are much shorter then the dephasing time ($T_2^* > 100$ ns for the NV spin). For a Gaussian decay the pulse fidelity is roughly $F_p \approx 1 - t_p^2/T_2^{*2}$. In order to reduce the error resulting from inhomogeneous broadening to < 1 % means $t_p < 10$ ns. Such strong driving can be realized by using high power (~ 30 W) amplifiers and on-chip waveguides that confine the large microwave power to small volumes. The electronic setup and the preparation of the sample are described in section 2.4.2.

Another source for errors in the control pulses are phase transients in the tails of the control pusles which may arise from limited bandwidth and reflections. As we will explain in the next section we use high-bandwidth on-chip coplanar waveguides to deliver the microwave pusles to the sample. Reflections can be reduced by placing attenuators at locations in the setup where impedance

mismatches occur (e.g. at the ports of the amplifiers and microwave launchers of the PCB containing the sample). Attenuators placed after the amplifier will reduce the microwave power at the sample. In our setup we can achieve Rabi frequencies in excess of 200 MHz (see Fig. 2.14, for our setup, however, $\sim$ 60 MHz driving is sufficient. The surplus of power is therefore enough to reduce reflections by roughly an order of magnitude.

Electronic setup

The timing between all optical, microwave and trigger pulses is controlled by the AWG. A schematic overview of the setup is depicted in Fig. 2.13. Each measurement cycle consists of three steps (Fig. 2.13). First, the NV center is initialized in the spin ground state $m_s = 0$ by a laser pulse (600 ns length). Then the desired MW pulses are applied. Finally, another green pulse is applied and the photoluminescence (PL) is measured during an integration time of about 600 ns.

For the experiments performed in chapter 6 two vector signal generators are used to simultaneously control the NV and surrounding Nitrogen electron spins. A bath spin have multiple transitions depending on which spectral group it belongs to. This means that in order to control all spectral groups simultaneously in one experiment we need to generate sequences containing multi-frequency control pulses. These are synthesized using two of the analog channels of the AWG and the high bandwidth (250 MHz) IQ modulation input of a vector source operating in the RF range. The undesired image frequency for each pulse in the sequence is rejected by giving each pulse in the I and Q sequence the proper phase that selects the sum or difference frequency.

Sample preparation

The diamond sample is a single crystal type Ib plate from Element Six, with a Nitrogen concentration specified to be less than 200 ppm. In order to achieve high sufficiently strong driving of the NV spin we need to apply oscillating magnetic fields of > 35 G in the microwave range perpendicular to the $\langle 111 \rangle$ orientation of the NV center.

We achieve this by sending RF and MW signals through a coplanar waveguide (CPW), which is fabricated directly on the diamond substrate using e-beam lithography. The amplitude of the MW current is the highest at the edges of the conductors. This current will produce a microwave magnetic field B_1 between the Au conductors of the CPW (Fig. 2.14). By making the lateral dimensions of the waveguide sufficiently small (seperation between the conductors ~ 10 μm) the current distribution profile of the waveguide will be compressed and resulting in large induced magnetic fields B_1 near the conductors of the CPW.

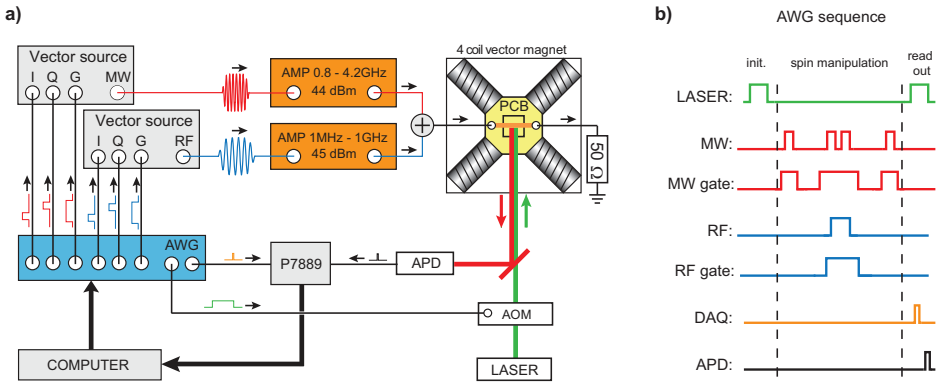

Figure 2.13: a, Room temperature electronic setup. An arbitrary Waveform Generator (AWG, Textronix AWG5014) is at the core of the electronic setup, synchronizing the input signals to the instruments through multiple channels. The AWG provides the I/Q modulation of a Rohde & Schwartz SMBV 100A vector signal generator (Vector source). To increase the MW source on/off ratio, the pulse modulation input (labeled G) is used as gate which suppresses the microwave leakage by < 80 dB. The MW bursts are amplified by a high power amplifier (Amplifier Research 25S1G4, bandwidth 0.8 - 4.2 GHz). Pulses of ac current in the radio frequency range (∼MHz) are generated by a separate vector source operating the in the RF range. After amplification (Amplifier Research 30W1000B, bandwidth 1 MHz - 1 GHz), the RF and MW bursts are combined and sent to the sample via the printed circuit board (PCB). The PCB is terminated by 50 Ω at the output of the PCB. The PCB is is mounted in a 4 coil vector magnet which allows for a careful alignment of the static magnetic fields along the NV symmetry axis. The AWG also provides the modulation to the AOM to generate laser pulses, and triggers a multiple-event time digitizer (FastComTec P7889) to start counting photons detected by the APD. Picture adapted from [5]. **b,** Basic measurement pulse sequence. The NV center is first initialized in $m_s = 0$ using a 600 ns green (532 nm) laser pulse. After that the manipulation stage follows where microwave and (optionally) RF pulse sequences are applied. Gate pulses are defined around the MW and RF pulses to suppress leakage. MW pulses with inter-pulse delays shorter than 10 ns share a single gate. Optical read out is followed where a laser pulse is applied. At the same time a trigger is sent to the P7889 data acquisition (DAQ) board which records the photon detections events coming from the APD during a time window of 600 ns.

Close to the surface B_1 will be oriented perpendicular to the substrate surface which has its normal along the $\langle 001 \rangle$ orientation. The component of B_1 perpendiclar to the $\langle 111 \rangle$ orientation will therefore be roughly $0.8B_1$. We are able to generate oscillating magnetic fields of > 100 G and achieve a Rabi frequency well in excess of 100 MHz. Typical driving strengts used for pulses in this thesis range

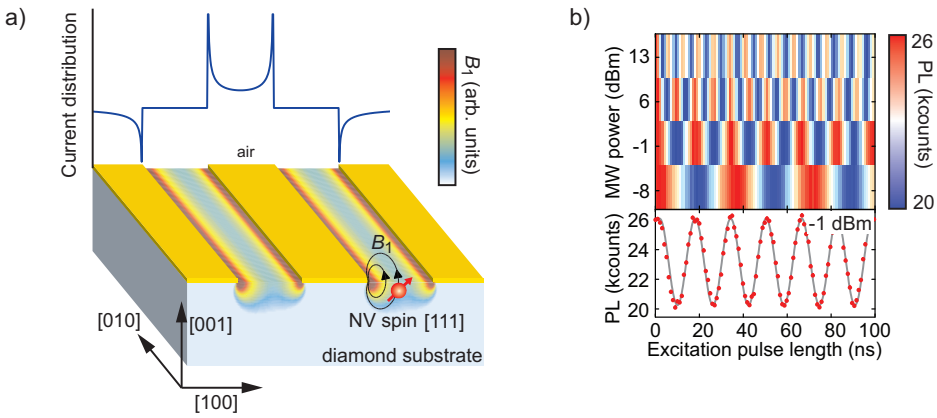

Figure 2.14: **a,** Current distribution in a CPW (top) and schematic picture of the sample (bottom). The current distribution peaks at the edges of the Au conductors (yellow). The CPW (Au) is fabricated directly on the diamond substrate. The amplitude profile of the vertical component of the driving field B_1 is determined using the above current profile. An exposed section of $\langle 001 \rangle$ oriented diamond is located between the Au conductors. NV centers between the conductors of the CPW have their quantization axis along one of the four $\langle 111 \rangle$ directions. The driving field B_1 is oriented predominantly along the $\langle 001 \rangle$ direction. **b,** Coherent oscillations of the NV spin for increasing power. For the highest powers we achieve Rabi frequencies well in excess of 100 MHz. The single trace shows coherent oscillations of 60 MHz.

between 50 and 80 MHz. This is mainly to prevent pulses from being distorted by non-linearities in the electronics and to prevent heating of the sample for long sequences with high duty cycles.

Data normalization and noise reduction

The spin state is determined from the spin-dependent PL. Normalization is performed by measuring the spin-dependent fluorescence belonging to the $m_s = 0$ ($|0\rangle$) $m_s = -1$ ($|1\rangle$) before each individual data point. Normalization measurements give the maximum and minimum PL levels respectively, and are used to rescale the data. The maximum PL is found by performing a readout after polarization, while the minimum PL is found by applying a π-pulse after the polarization and before the readout. The effectiveness of population inversion after a π-pulse is confirmed by process tomography ($F \approx 0.99$, see Ch. 3) and by comparison with adiabatic inversion experiments [46].

To prevent $1/f$ noise in the PL induced by drifts in the setup, a single data point, including its normalization, is measured once before moving to the next

data point. This results in fast ($\sim$ 1 ms) sweeps during which all data points are measured. These sweeps are repeated until the desired signal-to-noise ratio is achieved. Noise in both data and normalization is due to Poissonian statistics of the photon detection events. Due to the low readout efficiency ($\sim$ 1%), the typical number of averages to get reduce the noise to 2% is of the order of 10^6. We average the normalization points ten times more than the data points to limit the noise introduced by the normalization.

Bibliography

[1] M. A. Nielsen and I. Chuang. *Quantum Computation and Quantum Information*. Cambridge University Press, 2000.

[2] C.P. Slichter. *Principles of Magnetic Resonance*. Springer-Verlag, New York (1990).

[3] M. Howard *et al.* Quantum process tomography and Linblad estimation of a solid-state qubit. *New Journal of Physics* **8**, 33 (2006).

[4] J. D. Jackson. *Classical Electrodynamics*. John Wiley & Sons, Inc., 1975.

[5] T. van der Sar. *Quantum control of single spins and single photons in diamond*. Ph.D. thesis, Delft, The Netherlands (2012).

[6] N. Manson, J. Harrison and M. Sellars. Nitrogen-vacancy center in diamond: Model of the electronic structure and associated dynamics. *Physical Review B* **74**, 104303 (2006).

[7] A. Gali, M. Fyta and E. Kaxiras. Ab initio supercell calculations on nitrogen-vacancy center in diamond: Electronic structure and hyperfine tensors. *Physical Review B* **77**, 155206 (2008).

[8] A. Batalov *et al.* Low Temperature Studies of the Excited-State Structure of Negatively Charged Nitrogen-Vacancy Color Centers in Diamond. *Physical Review Letters* **102**, 195506 (2009).

[9] M. W. Doherty, N. B. Manson, P. Delaney and L. C. L. Hollenberg. The negatively charged nitrogen-vacancy centre in diamond: the electronic solution. *New Journal of Physics* **13**, 025019 (2011).

[10] L. J. Rogers, R. L. McMurtrie, M. J. Sellars and N. B. Manson. Time-averaging within the excited state of the nitrogen-vacancy centre in diamond. *New Journal of Physics* **11**, 063007 (2009).

[11] L. Robledo, H. Bernien, T. van der Sar and R. Hanson. Spin dynamics in the optical cycle of single nitrogen-vacancy centres in diamond. *New Journal of Physics* **13**, 025013 (2011).

[12] L. J. Rogers, S. Armstrong, M. J. Sellars and N. B. Manson. Infrared emission of the NV centre in diamond: Zeeman and uniaxial stress studies. *New Journal of Physics* **10**, 103024 (2008).

[13] T. van der Sar *et al.* Decoherence-protected quantum gates for a hybrid solid-state spin register. *Nature* **484**, 82 (2012).

[14] Gaudin, M. Diagonalisation d'une classe d'hamiltoniens de spin. *Journal of Physics France* **37**, 1087 (1976).

[15] J. Walker. Optical absorption and luminescence in diamond. *Reports on Progress in Physics* **42**, 1605 (1979).

[16] W. Smith, P. Sorokin, I. Gelles and G. Lasher. Electron-spin resonance of nitrogen donors in diamond. *Physical Review* **115**, 1546 (1959).

[17] J. H. N. Loubser and J. A. van Wyk. Electron spin resonance in the study of diamond. *Reports on Progress in Physics* **41**, 1201 (1978).

[18] G. Davies. The Jahn-Teller effect and vibronic coupling at deep levels in diamond. *Reports on Progress in Physics* **44**, 787 (1981).

[19] E. C. Reynhardt, G. L. High and J. A. van Wyk. Temperature dependence of spin-spin and spin-lattice relaxation times of paramagnetic nitrogen defects in diamond. *Journal of Chemical Physics* **109**, 8471 (1998).

[20] J. A. van Wyk, E. C. Reynhardt, G. L. High and I. Kiflawi. The dependences of esr line widths and spin - spin relaxation times of single nitrogen defects on the concentration of nitrogen defects in diamond. *Journal of Physics D: Applied Physics* **30**, 1790 (1997).

[21] L. Childress *et al.* Coherent dynamics of coupled electron and nuclear spin qubits in diamond. *Science* **314**, 281 (2006).

[22] G. Balasubramanian *et al.* Ultralong spin coherence time in isotopically engineered diamond. *Nature Materials* **8**, 383 (2009).

[23] A. J. Leggett *et al.* Dynamics of the dissipative two-state system. *Reviews of Modern Physics* **59**, 1 (1987).

[24] R. Hanson, V. V. Dobrovitski, A. E. Feiguin, O. Gywat and D. D. Awschalom. Coherent dynamics of a single spin interacting with an adjustable spin bath. *Science* **320**, 352 (2008).

[25] R. Hanson, L. P. Kouwenhoven, J. R. Petta, S. Tarucha and L. M. K. Vandersypen. Spins in few-electron quantum dots. *Reviews of Modern Physics* **79**, 1217 (2007).

[26] A. Morello *et al.* Single-shot readout of an electron spin in silicon. *Nature* **467**, 687 (2010).

[27] W. Zurek. Quantum darwinism. *Nature Physics* **5**, 181 (2009).

[28] V. V. Dobrovitski, A. E. Feiguin, R. Hanson and D. D. Awschalom. Decay of rabi oscillations by dipolar-coupled dynamical spin environments. *Physical Review Letters* **102**, 237601 (2009).

[29] J. Klauder and P. Anderson. Spectral diffusion decay in spin resonance experiments. *Physical Review* **125**, 912 (1962).

[30] L. Ornstein and G. Uhlenbeck. On the theory of brownian motion. *Physical Review* **36**, 823 (1930).

[31] R. de Sousa and S. Das Sarma. Electron spin coherence in semiconductors: Considerations for a spin-based solid-state quantum computer architecture. *Physical Review B* **67**, 033301 (2003).

[32] R. Amsüss *et al.* Cavity qed with magnetically coupled collective spin states. *Physical Review Letters* **107**, 060502 (2011).

[33] R. Kubo, M. Toda and N. Hashitsume. *Statistical Physics II.* Springer, Berlin, New York (1998).

[34] M. J. Biercuk, A. C. Doherty and H. Uys. Dynamical decoupling sequence construction as a filter-design problem. *Journal of Physics B: Atomic, Molecular and Optical Physics* **44**, 154002 (2011).

[35] E. L. Hahn. *Physical Review* **80**, 580 (1950).

[36] J. Medford *et al.* Scaling of dynamical decoupling for spin qubits. *Physical Review Letters* **108**, 086802 (2012).

[37] M. J. Biercuk *et al.* Optimized dynamical decoupling in a model quantum memory. *Nature* **458**, 996 (2009).

[38] J. Bylander *et al.* Noise spectroscopy through dynamical decoupling with a superconducting flux qubit. *Nature Physics* **7**, 565 (2011).

[39] J. Du *et al.* Preserving electron spin coherence in solids by optimal dynamical decoupling. *Nature* **461**, 1265 (2009).

[40] H. Bluhm *et al.* Dephasing time of gaas electron-spin qubits coupled to a nuclear bath exceeding 200 μs. *Nature Physics* **7**, 109 (2011).

[41] Z.-H. Wang *et al.* Effect of pulse error accumulation on dynamical decoupling of the electron spins of phosphorus donors in silicon. *Physical Review B* **85**, 085206 (2012).

[42] G. Uhrig. Keeping a quantum bit alive by optimized π-pulse sequences. *Physical Review Letters* **98**, 100504 (2007).

[43] G. Davies and M. F. Hamer. Optical Studies of the 1.945 eV Vibronic Band in Diamond. *Proceedings of the Royal Society A: Mathematical, Physical and Engineering Sciences* **348**, 285 (1976).

[44] A. Gruber *et al.* Scanning Confocal Optical Microscopy and Magnetic Resonance on Single Defect Centers. *Science* **276**, 2012 (1997).

[45] C. Kurtsiefer, S. Mayer, P. Zarda and H. Weinfurter. Stable solid-state source of single photons. *Physical Review Letters* **85**, 290 (2000).

[46] G. D. Fuchs, V. V. Dobrovitski, D. M. Toyli, F. J. Heremans and D. D. Awschalom. Gigahertz dynamics of a strongly driven single quantum spin. *Science* **326**, 1520 (2009).

Chapter 3

Bootstrap tomography of the pulses for quantum control

V. V. Dobrovitski, G. de Lange, D. Ristè and R. Hanson

Long-time dynamical decoupling and quantum control of qubits require high-precision control pulses. Full characterization (quantum tomography) of imperfect pulses presents a bootstrap problem: tomography requires initial states of a qubit which can not be prepared without perfect pulses. We present a protocol for pulse error analysis, specifically tailored for a wide range of the single solid-state electron spins. Using a single electron spin of a nitrogen-vacancy (NV) center in diamond, we experimentally verify the correctness of the protocol, and demonstrate its usefulness for quantum control tasks.

This chapter has been published in Physical Review Letters **107**, 077601 (2010)

3.1 Introduction

Coherent manipulation of single and few electron spins has recently been achieved in several solid-state systems such as quantum dots and diamond defect centers. Such systems are promising candidates for quantum information processing [1,2], precise metrology [3–5] and ultra-sensitive magnetometry [6–8]. They also present an excellent testbed for studying the fundamental problems of quantum dynamics of open systems [9–16]. High-speed manipulation of the system's quantum state can be achieved by using microwave or optical pulses [17–22], which must be fine-tuned to provide a high degree of fidelity. For example, sequences of quantum control pulses can be used to extend the coherence time via dynamical decoupling [23–28]. For long sequences, even small errors in the pulses will destroy the coherence that one attempts to preserve [27, 29] and may even lead to artificial saturation [30–32]. Therefore, precise characterization of errors is essential for successful implementation of complex quantum control protocols. With known errors, composite pulses and/or special pulse sequences can be chosen to mitigate the problem.

Complete information on the action of a pulse can in principle be gained with quantum process tomography (QPT) [33]. However, QPT of an imperfect pulse requires preparation and measurement of a complete set of reference states, whereas in many solid-state qubit systems (e.g. quantum dots, diamond defect centers, superconducting circuits) only one state can be prepared reliably (without the imperfect pulses), and only one observable can be directly measured. All other states can be prepared only with the imperfect pulses themselves, and therefore have errors [34]. This presents a bootstrap problem: the reference states contain the very same errors that we want to determine.

The problem of pulse error analysis has been studied extensively in the areas of NMR and ESR [35–38]. However, single electron spins in solid-state settings present new opportunities and challenges, and call for new approaches tailored at the specific demands of these systems. The driving pulse field can be tightly confined in the vicinity of the target spin. The resulting strong, nanosecond-timescale pulses enable fast spin manipulation, but the standard pulse error analysis [35–39] used in NMR becomes inapplicable. At strong driving, the spin dynamics changes noticeably [22]. The non-secular terms in the rotating frame can become important. The ac-Stark and Bloch-Siegert shifts can significantly detune the pulse frequency from resonance [22] and tilt the rotation axis towards the z-axis. Also, the pulse edges constitute a much larger fraction of the short pulse, and the driving field at the edges varies much faster and stronger than in typical NMR pulses. The resulting errors [22] (e.g. tilting of the rotation axis) can go beyond the standard treatment, and can not always be removed by symmetrizing the pulse shape.

Also, typical NMR systems have long coherence times that exceed the pulse width by orders of magnitude. The standard tune-up protocols [35–38] exploit this advantage, and use sequences with tens or hundreds of pulses to achieve outstanding precision in pulse parameters. But single solid-state electron spins are dephased faster, on a timescale T_2^* of microseconds down to tens of nanoseconds [9]. After only tens of pulses the signal becomes a complex mixture of pulse errors and decoherence [30–32]. To ensure a reliable measurement of the errors, the sequences for single electron spins must be short so that decoherence during each sequence would be negligible.

3.2 The Bootstrap protocol

Here, we present a systematic approach to pulse characterization for single solid-state electron spins, which is usable at shorter coherence times and much stronger driving power compared to traditional NMR systems. The proposed protocol contains four series of measurements, each having only 1–3 pulses, thus minimizing the effect of decoherence. The measured signal quantifying the pulse errors grows linearly with the errors to ensure a good accuracy for small errors. Also, the signal is zero for zero errors for good relative accuracy. The protocol determines all pulse errors: the rotation angle and all three components of the rotation axis. We experimentally demonstrate the protocol on a single spin of a nitrogen-vacancy (NV) defect center in diamond. By deliberately introducing known pulse errors, we verify the accuracy and self-consistency of the protocol, and use it to significantly increase the fidelity of QPT.

Our goal is to determine the parameters of four pulses, π_X, π_Y, $\pi/2_X$, and $\pi/2_Y$ applied to a two-level quantum system (π_X denotes a rotation by an angle π around the x-axis in the rotating frame; other notations are analogous). Minimization of the pulse errors and pulse optimization are not the subjects of this paper. This set of pulses allows implementation of universal decoupling XY sequences [23–25], full tomography of the density matrix, and universal single-qubit gates [33]. We assume that the pulse errors are reasonably small, and consider only the first-order terms in these quantities (since we want the signal to grow proportionally to errors). We also assume that the pulse width t_p is small in comparison with the dephasing time T_2^*; in this case the impact of decoherence is of second order, $(t_p/T_2^*)^2$, and is negligible for short sequences. Under this assumption the evolution of a spin during the pulse can be described a unitary rotation. For example, for $S = 1/2$, the evolution (in the rotating frame) during an imperfect π_X pulse is given by

$$U_X = \mathrm{e}^{-i(\vec{n}\vec{\sigma})(\pi+2\phi)/2} \approx -\phi\mathbf{1} - i(\sigma_x + \epsilon_y\sigma_y + \epsilon_z\sigma_z), \tag{3.1}$$

where $\sigma_{x,y,z}$ are the Pauli matrices, $\mathbf{1}$ is a 2×2 identity matrix, the rotation angle

error is 2ϕ and the rotation axis $\vec{n}$ has small components $n_y = \epsilon_y$ and $n_z = \epsilon_z$. Similarly, a $\pi/2_X$ pulse U'_X has the rotation angle error $2\phi'$, and the small rotation axis components ϵ'_y and ϵ'_z along y and z, respectively. Note that two $\pi/2$ pulses do not yield the same evolution as one π pulse due to errors introduced by the pulse edges. Analogous parameters for y-pulses will be denoted as 2χ, v_x, and v_z (angle and axis errors for π_Y), and $2\chi'$, v'_x, and v'_z (angle and axis errors for $\pi/2_Y$).

The bootstrap protocol shares ideas with standard QPT, and with the NMR tune-up sequences. Before each measurement, the spin is in the state $|\uparrow\rangle$, and the measured signal is $\langle\psi|\sigma_z|\psi\rangle$, where $|\psi\rangle$ is the wavefunction after the pulse. The preparation and the readout axes are usually fixed: e.g., for NV centers, they both coincide with one of the crystallographic $\langle 111\rangle$ directions. A possible mismatch between these axes in other systems can be taken into account, but complicates the protocol, and is not considered here. An imperfect pulse U_j can be represented as a product $U_j = U_j^{(0)} V_j \approx U_j^{(0)}(\mathbf{1} - iK_j)$, where $U_j^{(0)}$ is a corresponding ideal rotation and the Hermitian operator K_j is proportional to small pulse errors. Applying two pulses U_1 and U_2 in succession, we obtain up to linear order in K_j

$$U_{21} = U_2 U_1 \approx U_2^{(0)} U_1^{(0)} - iU_2^{(0)} K_1 - iK_2 U_1^{(0)}, \tag{3.2}$$

and the terms $U_2^{(0)} K_1$ and $K_2 U_1^{(0)}$ contain different matrix elements of the operators K_1 and K_2. E.g., if U_1 and U_2 are the (imperfect) $\pi/2_Y$ and $\pi/2_X$ rotations, the signal detected after this sequence, $S_{21} = \mathrm{Tr}(\sigma_z U_{21}|\uparrow\rangle\langle\uparrow| U_{21}^\dagger)$, contains a linear combination of the matrix elements $\langle\uparrow|K_1|Y\rangle$ and $\langle\uparrow|K_2|X\rangle$ (where $|Y\rangle = |\uparrow\rangle + i|\downarrow\rangle$ and $|X\rangle = |\uparrow\rangle + |\downarrow\rangle$). Combining different pulses, we obtain a sufficient number of such linear combinations of various matrix elements of K_j to uniquely determine all of them. A general approach to bootstrap tomography can be formulated in the language of QPT, by expanding the operation element operators [33] in terms of small errors. More complex bootstrap protocols applicable to more complex systems (higher spins, few qubits, etc.) can be designed in a similar manner. Here, we focus on a single two-level system.

The protocol is summarized in Table 3.1. It consists of three blocks of measurement sequences. For each sequence the measured signal is given in terms of the error parameters. The first block, with two single-pulse sequences, yields the rotation angle errors for the $\pi/2$ pulses. This information is then used in the second block, consisting of four two-pulse sequences, to find the rotation angle errors and the components of the rotation axis along z for the π pulses. The third block has six multi-pulse sequences, yielding six signals that are linearly related to the remaining six pulse error parameters. This linear system is underdetermined, since the whole system of pulses is invariant under rotations around

Table 3.1: Summary of the bootstrap protocol: pulse sequences (read from right to left) and the resulting signals expressed in terms of the error parameters. Blocks of sequences are separated by horizontal lines.

Sequence	Signal
$\pi/2_X$	$-2\phi'$
$\pi/2_Y$	$-2\chi'$
$\pi/2_X$-π_X	$2(\phi+\phi')$
$\pi/2_Y$-π_Y	$2(\chi+\chi')$
π_Y-$\pi/2_X$	$-2v_z+2\phi'$
π_X-$\pi/2_Y$	$2\epsilon_z+2\chi'$
$\pi/2_Y$-$\pi/2_X$	$-\epsilon'_y-\epsilon'_z-v'_x-v'_z$
$\pi/2_X$-$\pi/2_Y$	$-\epsilon'_y+\epsilon'_z-v'_x+v'_z$
$\pi/2_X$-π_X-$\pi/2_Y$	$-\epsilon'_y+\epsilon'_z+v'_x-v'_z+2\epsilon_y$
$\pi/2_Y$-π_X-$\pi/2_X$	$-\epsilon'_y-\epsilon'_z+v'_x+v'_z+2\epsilon_y$
$\pi/2_X$-π_Y-$\pi/2_Y$	$\epsilon'_y-\epsilon'_z-v'_x+v'_z+2v_x$

the z-axis. We may put $\epsilon'_y = 0$, taking the phase of the $\pi/2_X$ pulse as the x direction in the rotating frame. This fixes all other directions, and all errors are uniquely determined. No unphysical results appear in this bootstrap protocol: in experiments below, we use the bare measurement data imposing no additional conditions.

3.3 Experimental verification of the protocol

We now demonstrate and verify the protocol experimentally by applying it to a single solid-state spin system. We use the spin of a single Nitrogen-Vacancy (NV) center, which is a defect in diamond composed of a substitutional nitrogen atom with an adjacent vacancy [40]. The NV center's spin can be optically polarized and read out [40]. The unpolarized part of the spin's density matrix is proportional to the identity matrix, and gives no contribution to the signal (i.e. the NV spin state is pseudo-pure as in traditional NMR/ESR). The experiments are performed in a home-built confocal microscope at room temperature. NV centers in nanocrystals are prepared on a chip with a lithographically-defined waveguide allowing fast and precise spin rotations by magnetic resonance.

We controllably introduce two types of pulse errors, and use the bootstrap protocol to extract their values. First, we vary the phase Φ of the nominal $\pi/2_Y$-pulse between $-30°$ and $30°$ from its nominal value. In this way, we are

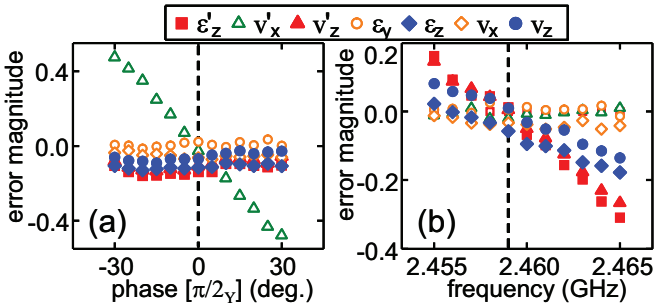

Figure 3.1: Experimental verification of the bootstrap protocol by introducing varying pulse errors. Duration of the $\pi/2$-pulses (π-pulses) is 5 ns (9 ns). **(a)** Measured error parameters for different phases Φ of the $\pi/2_Y$-pulse. The frequency of the driving field is set at 2.4605 GHz. **(b)** Measured error parameters for various frequencies of the driving field. Error bars everywhere are smaller than the symbol size.

changing the error parameter $v'_x = -\sin\Phi \approx -\Phi(\text{rad})$ while leaving all other errors constant. Figure 3.1(a) shows the experimental results that clearly support this expectation.

In the second experiment we detune the microwave excitation away from the qubit transition frequency, thereby varying the z-components of the rotation axis for all pulses. As shown in Fig. 3.1(b), the extracted error parameters v_z, v'_z, ϵ_z, and ϵ'_z strongly change (roughly linearly) with the detuning as expected, while the other error parameters stay virtually constant. The errors of the nominal $\pi/2$-pulses vary about twice as much as the errors of the nominal π-pulses, indicating that the errors originate largely from the pulse edges. Since the edges are the same for all pulses, they have larger impact on shorter pulses. The data in Fig. 3.1(a)-(b) demonstrate that the bootstrap protocol is indeed an effective and reliable tool for extracting pulse errors.

3.4 Correcting QPT results for pulse errors

Due to experimental limitations it may be impossible to cancel all errors at once. In that case, the choice of the optimal working point involves a trade-off, and precise knowledge of the pulse errors becomes particularly important. For example, when performing QPT, a set of the reference states is prepared using the pulses π_X, $\pi/2_X$, and $\pi/2_Y$. These states are acted upon by the process, and rotated to the readout basis before measurement [33]. The operation elements of the quantum process are expanded in the basis $E_0 = I$, $E_1 = \sigma_x$, $E_2 = \sigma_y$, and $E_3 = \sigma_z$, and the process is completely characterized by the 4×4 expansion

matrix χ [33]. When systematic pulse errors are present, the prepared initial states differ from the reference states, and the read-out is also performed in the incorrect basis, yielding an incorrect matrix χ. But with pulse errors known, the raw measured data can be transformed into the correct basis prior to the standard QPT data processing [33, 34, 41].

As a demonstration, and as a check of self-consistency of the bootstrap protocol, we perform QPT while introducing the same pulse errors as in Fig. 3.1. We show that with the pulse errors deduced with the protocol, the QPT results can be corrected. The comparison between raw and corrected data below is designed to use no *a priori* assumptions about correctness of the bootstrap protocol.

First, we take the (imperfect) π_Y pulse as an example of a quantum process. We introduce errors in the QPT procedure by changing the phase Φ of the nominal $\pi/2_Y$-pulse from $-30°$ to $30°$. We first determine the reference matrix of our quantum process. We perform QPT on this process using the $\pi/2_Y$ pulse with $\Phi = 0$, and the resulting reference matrix χ_0 is calculated in two ways: (i) using the raw uncorrected data, i.e. assuming that the pulses used for QPT are ideal (we denote this matrix as χ_0^{r}), and (ii) using the data corrected for the known pulse imperfections (the resulting matrix is χ_0^{c}). Next, we vary Φ, and use the artificially deteriorated $\pi/2_Y$ pulses to determine the matrix χ of the quantum process. This matrix is also determined in two ways, by using raw experimental data (matrix χ^{r}), and by correcting the data for the known pulse errors (matrix χ^{c}). For each value of Φ, we compare the raw-data matrices χ^{r} and χ_0^{r} on one hand, and the corrected matrices χ^{c} and χ_0^{c} on the other.

The process we are studying does not depend on the phase of the nominal $\pi/2_Y$ pulse. Thus, ideally, the matrices χ_0 and χ should be the same. To quantify the difference between χ_0 and χ, we use two distance measures. One is the process fidelity [33] $F = \mathrm{Tr}[\chi_0\chi]$, which depends quadratically on the pulse errors. The other measure is the Hilbert-Schmidt 2-norm $||M||_2 = \sqrt{\mathrm{Tr}[MM^\dagger]}$ of the difference matrix $M = \chi - \chi_0$. This norm is linear in, and thus more sensitive to, the pulse errors.

In Figs. 3.2(a)–(b), orange squares show the values of F and $||M||_2$ for the corrected-data matrices χ_0^{c} and χ^{c}. The expectation that χ_0 and χ should coincide is confirmed with excellent precision. Almost independently of Φ, the fidelity remains above 99%, and $||M||_2$ stays small. This is not so for the raw-data matrices χ_0^{r} and χ^{r} (blue squares). The neglected phase error of the nominal $\pi/2_Y$ pulse makes the matrix χ^{r} inaccurate, so F and $||M||_2$ depend on Φ, with fidelity dropping by 8% for $\Phi = 30°$.

In a second experiment (Figs. 2c and 2d), we perform tomography on an identity process. The reference matrix χ_0 for an ideal identity process is known, and needs no measurement. We detune the microwave excitation frequency away from the qubit transition, introducing the errors ϵ_z, ϵ_z', v_z, and v_z' (like in Fig. 3.1b)

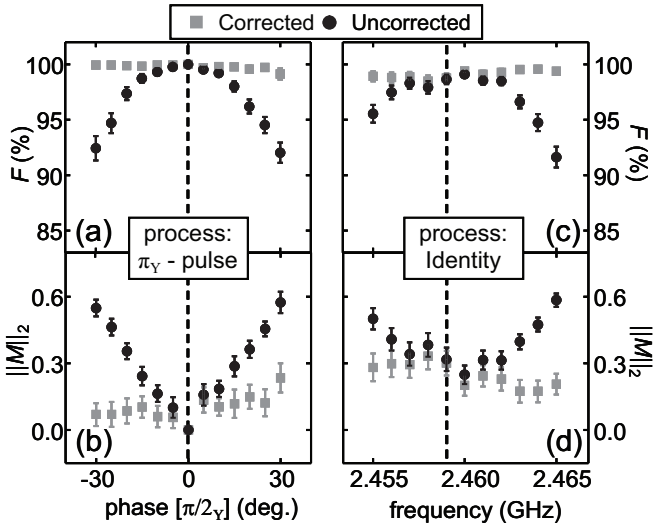

Figure 3.2: Correction of pulse errors in Quantum Process Tomography using the bootstrap protocol. **(a)** Fidelity (F) and **(b)** the 2-norm distance $||M||_2$ between the process measured at finite introduced $\pi/2_Y$ phase error and the process matrix measured at zero introduced error. The process is a π_Y- pulse with zero introduced error. Driving field frequency is 2.459 GHz. **(c)** F and **(d)** $||M||_2$ between the measured process and the actual process (identity). All measures are calculated both for the uncorrected and for the corrected data.

into all pulses. We perform QPT on the identity process and, as above, determine the corrected and the uncorrected matrices χ^{r}, and χ^{c}. These matrices are compared with the *ideal* identity process. The results are shown in Fig. 3.2(c)–(d). Again, the fidelities are high for the corrected data in the full range of introduced errors, while for the uncorrected data the fidelity has dropped by as much as 10%. The same behavior is seen for $||M||_2$. The key point here is that the corrected matrix χ^{c} does not depend on the errors: orange points in Figs. 2c and 2d form a flat curve. Without correction (blue points), the measured χ-matrix strongly depends on the pulse errors. Thus, even the effects of complex pulse errors introduced by detuning the frequency can be effectively corrected using the information from the bootstrap protocol.

3.5 Conclusions

Summarizing, we have developed and experimentally demonstrated an effective pulse error analysis protocol tailored to the specific requirements of single solid-state spins. The methods described in this paper may help in accurate determination of the properties of different quantum processes, a key feature for the fields of quantum information processing, quantum metrology and fundamental studies of quantum decoherence.

Acknowledgements

We would like to thank D. G. Cory, S. Lyon, A. Tyryshkin, M. Pruski, C. Ramanathan, K. Schmidt-Rohr, and M. Laforest for very useful and enlightening discussions. Work at Ames Laboratory was supported by the Department of Energy — Basic Energy Sciences under Contract No. DE-AC02-07CH11358. We gratefully acknowledge support from FOM, NWO and the DARPA QuEST program.

3.6 Additional material

Corrections of Quantum Process Tomography for pulse errors

It is important to know the rotation parameters of the pulses which are used for state preparation and tomography. This knowledge can be used to correct the results of process tomography performed with imperfect pulses. If the spin is rotated around an axis which deviates from the nominal rotation axis, then the preparation and readout is done in a basis which deviates from the nominal basis. Therefore, before applying the standard QPT recipe [33] to calculate the χ-matrix of the process, we use the information gained from the bootstrap protocol to transform the tomography data back to the proper basis. As the basis states, one can choose $\rho_0 = |0\rangle\langle 0|$, $\rho_1 = |1\rangle\langle 1|$, $\rho_x = |X\rangle\langle X|/2$, and $\rho_y = |Y\rangle\langle Y|/2$, which we below denote as $\{b_{01XY}\}$. Note that the matrices ρ_x and ρ_y are normalized, while the states $|X\rangle = |0\rangle + |1\rangle$ and $|Y\rangle = |0\rangle + i|1\rangle$ are not.

A general single-qubit QPT experiment consists of three basic steps. The first step of QPT is the preparation of one of the reference states using an imperfect pulse. Then, in the second step, the quantum process acts on the reference state. Finally, in the third step, state tomography of the resulting density matrix is performed, again using the pulses, to read out projections on the x, y, and z axes of the Bloch sphere and therefore requires three measurements. This recipe is

then repeated for each of the above mentioned reference states, giving a total of twelve measurements. Both preparation and readout, where imperfect pulses are used, introduce their own set of errors which might lead to unphysical and/or incorrect QPT results. The correction is done by unwinding the propagation of rotation axis errors.

To measure the distance between two process matrices, the theoretically expected reference matrix χ_0, and the experimentally obtained matrix χ, we use two metrics. One is the process fidelity $F = \mathrm{Tr}[\chi_0\chi]$. This metric is appropriate for quantum-information analysis, but depends quadratically on the pulse errors and therefore is less sensitive to them. The other measure is the Hilbert-Schmidt 2-norm $||M||_2 = \sqrt{\mathrm{Tr}[MM^\dagger]}$ of the difference matrix $M = \chi - \chi_0$. This norm is linear in, and thus more sensitive to, the pulse errors. Note also that the 2-norm $||M||_2$ is based on a quadratic function of the elements of the χ and χ_0 matrices; hence it includes the rms of experimental noise. The fidelity F, for a fixed χ_0, is a linear combination of the elements of χ.

State tomography corrections

We start our analysis from the final stage of the QPT, from the state tomography of the density matrix

$$\rho_{out} = \frac{I + r_x\sigma_x + r_y\sigma_y + r_z\sigma_z}{2}. \tag{3.3}$$

produced by the quantum process. To reconstruct this density matrix, we need to determine the projections r_x, r_y and r_z on the x, y, and z axes of the Bloch sphere. We apply (imperfect) pulses, and measure the observable σ_z. In this way, we find the projections of the density matrix on some other axes x', y', and z'. The results r'_x, r'_y, and r'_z are obtained from the measurement of σ_z after application, correspondingly, of the $\pi/2_Y$ pulse, $\pi/2_X$ pulse, and no pulse (so that z and z' axes coincide, and r'_z is equal to r_z). These measurement results are linearly related to the desired parameters r_x, r_y, and r_z:

$$\begin{bmatrix} r'_x \\ r'_y \\ r'_z \end{bmatrix} = \mathbf{M}_r \begin{bmatrix} r_x \\ r_y \\ r_z \end{bmatrix}. \tag{3.4}$$

where the linear relation between the results is defined by the transformation matrix

$$\mathbf{M}_r = \begin{bmatrix} v'_x v'_z - \eta & v'_x + v'_z\eta & v'^2_z \\ \epsilon'_z\xi - \epsilon'_y & \xi + \epsilon'_y\epsilon'_z & \epsilon'^2_z \\ 0 & 0 & 1 \end{bmatrix}. \tag{3.5}$$

Here we used the shorthand notations

$$\xi = \sqrt{1 - (\epsilon'_z)^2 - (\epsilon'_y)^2} \tag{3.6}$$

and

$$\eta = \sqrt{1 - (v'_z)^2 - (v'_x)^2}. \tag{3.7}$$

Here we assume, in accordance with our experimental situation, that the rotation angle errors ϕ, ϕ', χ, and χ' are adjusted to zero within the experimental accuracy. Note that r_z and r'_z coincide because it is read out without pulses. Also note that in the absence of errors x' axis is parallel to x, but has the opposite direction.

Inversion of the matrix $\mathbf{M}_r$ gives the correct state tomography values, which determine the density matrix for the output state of the quantum process

$$\rho_{out} = \frac{I + r_x\sigma_x + r_y\sigma_y + r_z\sigma_z}{2}. \tag{3.8}$$

Correcting for state preparation errors

The corrected density matrices are the result from the process acting on some unknown prepared reference state as a result of pulse errors. Before the standard recipe of QPT can be applied, one first needs to transform the density matrices so that they resemble density matrices resulting from the proper reference states $\{b_{01XY}\}$. Also in this case, knowledge of the pulse errors can be utilized to perform this transformation. For a process acting on an arbitrary state $\rho_{in} = a_0\rho_0 + a_1\rho_1 + a_x\rho_x + a_y\rho_y$ one finds

$$\rho_{out} = \mathcal{E}(\rho_{in}) \tag{3.9}$$

$$= a_0\mathcal{E}(\rho_0) + a_1\mathcal{E}(\rho_1) + a_x\mathcal{E}(\rho_x) + a_y\mathcal{E}(\rho_y). \tag{3.10}$$

In the case of state preparation errors, states that are prepared can be written as a linear combination of the proper reference states.

$$\begin{bmatrix} \rho'_0 \\ \rho'_1 \\ \rho'_x \\ \rho'_y \end{bmatrix} = \mathbf{M_p} \begin{bmatrix} \rho_0 \\ \rho_1 \\ \rho_x \\ \rho_y \end{bmatrix} \tag{3.11}$$

where the primes denote the real prepared states in the unknown basis. Namely, the state ρ'_1 is obtained by application of the imperfect π_X pulse to the initial state ρ_0, the state ρ'_x is obtained using the $\pi/2_Y$ pulse, and the state ρ'_y — using

the $\pi/2_X$ pulse. The explicit form of $\mathbf{M}_p$ is determined by the pulse errors and is given by

$$\mathbf{M}_p = \begin{pmatrix} 1 & 0 & 0 & 0 \\ \epsilon_z^2 - \gamma\epsilon_z - \epsilon_y\epsilon_z & 1 - \epsilon_z^2 - \gamma\epsilon_z - \epsilon_y\epsilon_z & 2\gamma\epsilon_z & 2\epsilon_y\epsilon_z \\ (\lambda_x + {v'_z}^2)/2 & (\lambda_x - {v'_z}^2)/2 & \eta + v'_x v'_z & v'_z\eta - v'_x \\ (\lambda_y + {\epsilon'_z}^2)/2 & (\lambda_y - {\epsilon'_z}^2)/2 & \epsilon'_y + \epsilon'_z\xi & \epsilon'_y\epsilon'_z - \xi \end{pmatrix} \tag{3.12}$$

where $\gamma = \sqrt{1 - \epsilon_y^2 - \epsilon_z^2}$, and we also introduced $\lambda_x = 1 - \eta - v'_x v'_z - v'_z\eta + v'_x$ and $\lambda_y = 1 + \xi - \epsilon'_y\epsilon'_z - \epsilon'_z\xi - \epsilon'_y$. If the quantum process $\mathcal{E}$ acts on the states prepared in the primed basis the result is

$$\begin{bmatrix} \mathcal{E}(\rho'_0) \\ \mathcal{E}(\rho'_1) \\ \mathcal{E}(\rho'_x) \\ \mathcal{E}(\rho'_y) \end{bmatrix} = \mathbf{M_P} \begin{bmatrix} \mathcal{E}(\rho_0) \\ \mathcal{E}(\rho_1) \\ \mathcal{E}(\rho_x) \\ \mathcal{E}(\rho_y) \end{bmatrix} \tag{3.13}$$

The matrix $(\mathbf{M_P})^{-1}$ can be used to generate the desired QPT output states. This concludes the corrections for QPT.

Often, the results of the QPT procedure result in a χ-matrix which does not satisfy the conditions of complete positivity and trace preservation (CPTP). In this case, least-square fitting can be used to fit the results to a CPTP process. No such fitting is used in this work.

Bibliography

[1] D. Loss and D. P. Divincenzo. Quantum computation with quantum dots. *Physical Review A - Atomic, Molecular, and Optical Physics* **57**, 120 (1998).

[2] L. Childress, J. M. Taylor, A. S. Sørensen and M. D. Lukin. Fault-tolerant quantum communication based on solid-state photon emitters. *Physical Review Letters* **96**, 1 (2006).

[3] J. A. Jones *et al.* Magnetic field sensing beyond the standard quantum limit using 10-spin noon states. *Science* **324**, 1166 (2009).

[4] P. Cappellaro *et al.* Entanglement assisted metrology. *Physical Review Letters* **94** (2005).

[5] J. M. Geremia, J. K. Stockton and H. Mabuchi. Suppression of spin projection noise in broadband atomic magnetometry. *Physical Review Letters* **94** (2005).

[6] J. M. Taylor *et al.* High-sensitivity diamond magnetometer with nanoscale resolution. *Nature Physics* **4**, 810 (2008).

[7] C. L. Degen. Scanning magnetic field microscope with a diamond single-spin sensor. *Applied Physics Letters* **92**, 243111 (2008).

[8] G. Balasubramanian *et al.* Nanoscale imaging magnetometry with diamond spins under ambient conditions. *Nature* **455**, 648 (2008).

[9] R. Hanson and D. D. Awschalom. Coherent manipulation of single spins in semiconductors. *Nature* **453**, 1043 (2008).

[10] L. Childress *et al.* Coherent dynamics of coupled electron and nuclear spin qubits in diamond. *Science* **314**, 281 (2006).

[11] R. Hanson, V. V. Dobrovitski, A. E. Feiguin, O. Gywat and D. D. Awschalom. Coherent dynamics of a single spin interacting with an adjustable spin bath. *Science* **320**, 352 (2008).

[12] D. J. Reilly *et al.* Measurement of temporal correlations of the overhauser field in a double quantum dot. *Physical Review Letters* **101** (2008).

[13] C. Latta *et al.* Confluence of resonant laser excitation and bidirectional quantum-dot nuclear-spin polarization. *Nature Physics* **5**, 758 (2009).

[14] I. T. Vink *et al.* Locking electron spins into magnetic resonance by electron-nuclear feedback. *Nature Physics* **5**, 764 (2009).

[15] C. H. Tseng *et al.* Quantum simulation of a three-body-interaction hamiltonian on an nmr quantum computer. *Physical Review A - Atomic, Molecular, and Optical Physics* **61**, 123021 (2000).

[16] S. Lloyd. Universal quantum simulators. *Science* **273**, 1073 (1996).

[17] J. Berezovsky, M. H. Mikkelsen, N. G. Stoltz, L. A. Coldren and D. D. Awschalom. Picosecond coherent optical manipulation of a single electron spin in a quantum dot. *Science* **320**, 349 (2008).

[18] D. Press, T. D. Ladd, B. Zhang and Y. Yamamoto. Complete quantum control of a single quantum dot spin using ultrafast optical pulses. *Nature* **456**, 218 (2008).

[19] Y. Wu *et al.* Selective optical control of electron spin coherence in singly charged gaas-al0.3ga0.7as quantum dots. *Physical Review Letters* **99** (2007).

[20] P. Neumann *et al.* Multipartite entanglement among single spins in diamond. *Science* **320**, 1326 (2008).

[21] L. Jiang *et al.* Repetitive readout of a single electronic spin via quantum logic with nuclear spin ancillae. *Science* **326**, 267 (2009).

[22] G. D. Fuchs, V. V. Dobrovitski, D. M. Toyli, F. J. Heremans and D. D. Awschalom. Gigahertz dynamics of a strongly driven single quantum spin. *Science* **326**, 1520 (2009).

[23] L. Viola, E. Knill and S. Lloyd. Dynamical decoupling of open quantum systems. *Physical Review Letters* **82**, 2417 (1999).

[24] L. F. Santos and L. Viola. Enhanced convergence and robust performance of randomized dynamical decoupling. *Physical Review Letters* **97** (2006).

[25] K. Khodjasteh and D. A. Lidar. Fault-tolerant quantum dynamical decoupling. *Physical Review Letters* **95**, 1 (2005).

[26] M. J. Biercuk *et al.* Optimized dynamical decoupling in a model quantum memory. *Nature* **458**, 996 (2009).

[27] J. Du *et al.* Preserving electron spin coherence in solids by optimal dynamical decoupling. *Nature* **461**, 1265 (2009).

[28] J. J. L. Morton *et al.* Bang-bang control of fullerene qubits using ultrafast phase gates. *Nature Physics* **2**, 40 (2006).

[29] H. D. Raedt, K. Michielsen, S. Miyashita and K. Saito. Physical Models for Quantum Computers. *Progress of Theoretical Physics Supplement* **145**, 233 (2002).

[30] W. Zhang *et al.* Long-time electron spin storage via dynamical suppression of hyperfine-induced decoherence in a quantum dot. *Physical Review B - Condensed Matter and Materials Physics* **77** (2008).

[31] W. Zhang, N. Konstantinidis, K. A. Al-Hassanieh and V. V. Dobrovitski. Modelling decoherence in quantum spin systems. *Journal of Physics Condensed Matter* **19** (2007).

[32] D. Li, A. E. Dementyev, Y. Dong, R. G. Ramos and S. E. Barrett. Generating unexpected spin echoes in dipolar solids with p pulses. *Physical Review Letters* **98** (2007).

[33] M. A. Nielsen and I. Chuang. *Quantum Computation and Quantum Information.* Cambridge University Press, 2000.

[34] J. M. Chow *et al.* Randomized benchmarking and process tomography for gate errors in a solid-state qubit. *Physical Review Letters* **102** (2009).

[35] B. C. Gerstein and C. R. Dybowski. Academic Press Inc., Orlando (1985).

[36] D. P. Burum, M. Under and R. R. Ernst. A new "tune-up" nmr pulse cycle for minimizing and characterizing phase transients. *Journal of Magnetic Resonance* **43**, 463 (1981).

[37] A. J. Shaka, D. n. Shykind, G. C. Chingas and A. Pines. Multiple-pulse sequences for precise transmitter phase alignment. *Journal of Magnetic Resonance* **80**, 96 (1988).

[38] U. Haubenreisser and B. Schnabel. Accurate phase adjustment for multiple pulse nmr of solids. *Journal of Magnetic Resonance* **35**, 175 (1979).

[39] J. J. L. Morton *et al.* Measuring errors in single-qubit rotations by pulsed electron paramagnetic resonance. *Physical Review A - Atomic, Molecular, and Optical Physics* **71**, 1 (2005).

[40] F. Jelezko and J. Wrachtrup. Read-out of single spins by optical spectroscopy. *Journal of Physics Condensed Matter* **16**, 1089 (2004).

[41] M. Howard *et al.* Quantum process tomography and linblad estimation of a solid-state qubit. *New Journal of Physics* **8**, 33 (2006).

Chapter 4

Universal dynamical decoupling of a single solid-state spin from a spin bath

G. de Lange, Z.H. Wang, D. Ristè, V.V. Dobrovitski and R. Hanson

Controlling the interaction of a single quantum system with its environment is a fundamental challenge in quantum science and technology. We strongly suppressed the coupling of a single spin in diamond with the surrounding spin bath by using double-axis dynamical decoupling. The coherence was preserved for arbitrary quantum states, as verified by quantum process tomography. The resulting coherence time enhancement is found to followed a general scaling with the number of decoupling pulses. No limit was observed for the decoupling action up to 136 pulses, for which the coherence time was enhanced more than 25 times compared to that obtained with spin echo. These results uncover a new regime for experimental quantum science and allow to overcome a major hurdle for implementing quantum information protocols.

This chapter has been published in Science **330**, 60 (2010).

4.1 Introduction

In the last decade, manipulation and measurement of single quantum systems in the solid state have been achieved [1, 2]. This control has promising applications in quantum information processing [3, 4], quantum communication [5], metrology [6], and ultra-sensitive magnetometry [7, 8]. However, uncontrolled interactions with the surroundings inevitably lead to decoherence of the quantum states [9] and pose a major hurdle for realizing these technologies. Therefore, the key challenge in current experimental quantum science is to protect individual quantum states from decoherence by their solid-state environment. If a quantum system can be controlled with high fidelity, dynamical decoupling can be exploited to efficiently mitigate the interactions with the environment [10–12]. By reversing the evolution of the quantum system at specific times using control pulses, the effect of the environment accumulated before the pulse is cancelled during the evolution after the pulse. When viewed at the end of the control cycle, the quantum system will appear as an isolated system that is decoupled from its environment. Thanks to recent progress in quantum control speed and precision [13]), we are now able to unlock the full power of dynamical decoupling at the level of a single spin.

4.2 Experimental setup

We focused on electron spins of single nitrogen-vacancy (NV) defect centers in diamond coupled to a spin bath (Fig. 4.1a). NV center spins can be optically imaged, initialized and read out, as well as coherently controlled at room temperature (Fig. 4.1b). These favorable properties have been exploited in the to gain deeper insight into spin decoherence [14], as well as for demonstrating basic quantum information protocols at room temperature [15, 16].

We used nanosecond microwave pulses to manipulate single NV spins. To raise the fidelity of our control to the required level for efficient decoupling, we fabricated on-chip coplanar waveguide (CPW) transmission lines using electron beam lithography (Fig. 4.1a). The high bandwidth of the CPW [13] combined with efficient suppression of reflections and fine-tuned pulse calibration allows fast and precise manipulation of the NV spin (Fig. 4.1b), leading to process fidelities of 99% for the basic control pulses needed for dynamical decoupling (see section 4.6).

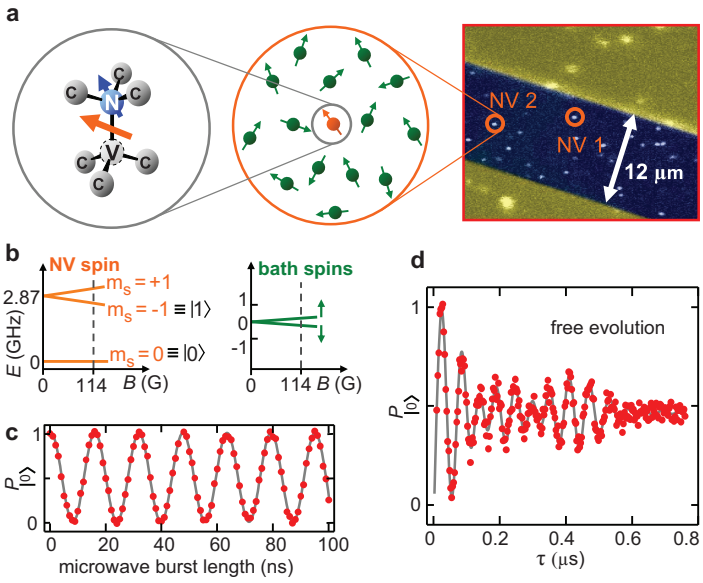

Figure 4.1: **(a)** Left: A Nitrogen-Vacancy defect is formed by a single substitutional nitrogen (^{14}N) atom and an adjacent vacancy (V). The NV electron spin (orange arrow) is coupled to the host 14N nuclear spin (blue arrow) through the hyperfine interaction. Middle: The NV center is surrounded by a bath of electron spins located at sites of substitutional nitrogen atoms in the diamond lattice [17]. Right: Confocal photoluminescence scan of a section of the device, where the golden regions are part of the on-chip coplanar waveguide (CPW) used for applying quantum control pulses and NV centers appear as bright spots in between the conductors of the CPW. **(b)** Energy level diagrams of the NV center electron spin (left) and the electron spins in the bath (right). An applied magnetic field splits the NV spin triplet electronic ground state; the effective two-level system used here is formed by the spin sublevels ms = 0 (labeled $|0\rangle$) and ms = -1 (labeled $|1\rangle$). **(c)** Coherent driven oscillations of NV1. For the pulsed experiments the same Rabi frequency is used. **(d)** Decay during free evolution of NV1 probed using Ramsey interference. Solid line is a fit (see section 4.6 and chapter 2). The fast oscillating component is due to a detuning of the driving field of 15 MHz with respect to the spin transition, whereas the beating is caused by the hyperfine interaction with the host nuclear spin.

4.3 The magnetic environment of the NV center: The spin-bath

The coherent dynamics of an NV spin are strongly influenced by the coupling to neighboring spins (the spin bath) [14, 17]. Because such spin environments

are very common in the solid state, our results are directly relevant for other solid-state quantum bits such as spins in quantum dots [18, 19] and donors in silicon [4, 20]. For the NV centers studied here, the bath is composed of electron spins localized on nitrogen impurity atoms. Resonant interactions (flip-flops) between the bath spins and the NV spin are suppressed due to a large energy mismatch [17]. Therefore, the impact of the spin bath on the NV spin is limited to dephasing and can be described as a random magnetic field $\delta B(t)$ that is directed along the NVŠs quantization axis. The value of $\delta B(t)$ is determined by the state of the environment. We modeled the bath field $\delta B(t)$ by an Ornstein-Uhlenbeck process with the correlation function $C(t) = \langle \delta B(0) \delta B(t) \rangle = b^2 \exp(-|t|/\tau_C)$, where b is the coupling strength of the bath to the spin and τ_C is the correlation time of the bath which measures the rate of flip-flops between the bath spins due to the intrabath dipolar coupling [21].

The values of the parameters describing the bath field were extracted from experiments. The bath-induced dephasing during free evolution had a Gaussian envelope $S(t) = \exp(-b^2 t^2/2)$, which yielded the value for b (see section 4.6); we found $b = (3.6 \pm 0.1)\ \mu\text{s}^{-1}$ for NV1 (Fig. 4.1c), and $b = (2.6 \pm 0.1)\ \mu\text{s}^{-1}$ for NV2 (see section 4.6). The quasi-static dephasing could be undone using a spin echo (SE) technique (Fig. 4.2a), revealing the much slower decay of spin coherence caused by the dynamics of the spin bath. The spin echo signal decayed as $SE(t) = \exp[-(t/T_2)^3]$, characteristic for a slowly fluctuating spin bath with $tau_C = T_2^3 b^2/12 >> 1/b$ [21]. The values we found for τ_C, $(25 \pm 3)\ \mu$s for NV1 ($T_2 = (2.8 \pm 0.1)\ \mu$s and $(23 \pm 3)\ \mu$s for NV2 ($T_2 = (3.5 \pm 0.2)\ \mu$s, confirmed this. The spin echo decay time T_2 is often considered as the coherence or memory time of the system. We took T_2 as the starting point and demonstrated that the coherence time could be markedly prolonged by dynamically decoupling the spin from the surrounding spin bath.

4.4 Dynamcial decoupling of the NV spin

We first explored the potential of dynamical decoupling by extending the spin-echo (SE) pulse sequence to periodic repetitions of the Carr-Purcell-Meiboom-Gill (CPMG) cycle (Fig. 4.2a). The decoupling performance was characterized by measuring the state fidelity $F_s = \langle \Psi_i | \rho_m | \Psi_i \rangle$, where $|\Psi_i\rangle$ is the expected (ideal) state after applying the sequence and ρ_m the measured density matrix of the actual state. Although the coherence had vanished after 4 microseconds for the SE case, we observe that the 8-pulse CPMG sequence preserved the coherence almost completely during this same time.

The optimal decoupling sequence for a quantum system depends on the coupling to its environment and the dynamics within the environment itself. In Ref. [23], non-periodic inter-pulse spacing, now called the UDD sequence, was

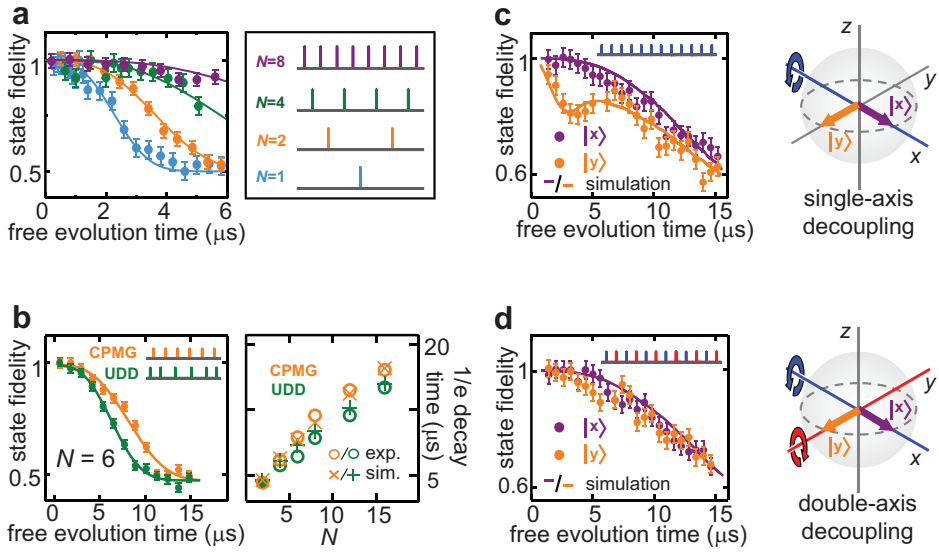

Figure 4.2: **(a)** Left: state fidelities for the CPMG decoupling sequence applied to NV1. The blue curve is a spin echo measurement. High state fidelity is recovered for increasing number of pulses N. Solid lines are fits to $\sim \exp[-(t/T_{\mathrm{coh}})^3]$. Right: vertical lines indicate the location of π-pulses. **(b)** Comparison of decoupling with CPMG (orange) and UDD (green) for $N = 6$ pulses. The solid lines are fits to $\sim \exp[-(t/T_{\mathrm{coh}})^3]$. The right panel shows the $1/e$ decay times from fits to data and to simulations [22]. The same color scheme applies. **(c)** Single-axis decoupling for different input states, showing state-selective decoupling for the CPMG sequence with $N = 12$ operations (shown in the upper right). Bloch sphere on the right shows input states and the decoupling axis. Solid lines are numerical simulations incorporating the experimental pulse errors [22]. **(d)** Double-axis decoupling, with XY4 sequence with $N = 12$, showing excellent decoupling for both input states. Pulse timings are the same as for CPMG but with the decoupling axis alternating between X and Y, as is shown on the right. The simulations for and yield virtually the same curve and therefore appear as one.

found to achieve a strong improvement in decoupling efficiency over periodic pulse spacing in the case of environmental noise spectra with a hard cut-off; this was experimentally verified in Refs. [24, 25]. Recent theory [26, 27], however, suggests that periodic, CPMG-like pulse spacing is ideal for decoupling from an environment with a soft cut-off. We investigated the efficiency of these different protocols in decoupling a single spin from a spin bath environment (Fig. 4.2b) and observed that CPMG outperforms UDD for all numbers of pulses investigated in

both simulations and experiments (Fig. 4.2b, right panel). These findings are in agreement with our model of a Lorentzian bath noise spectrum, which exhibits a soft cut-off (see section 4.6).

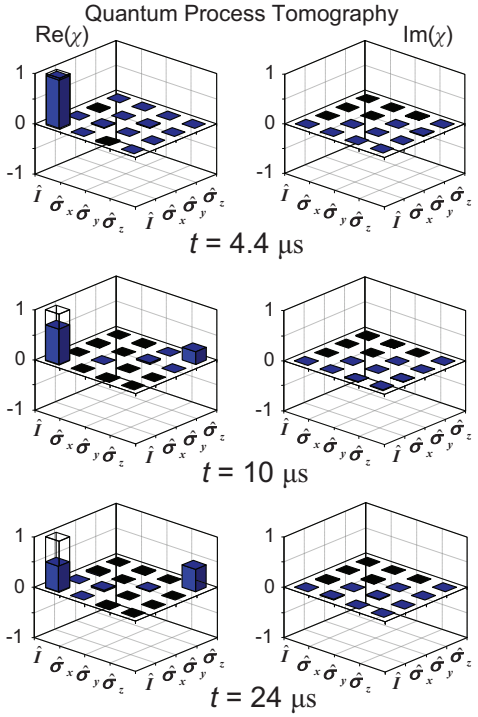

Figure 4.3: QPT is performed at free evolution times of 4.4, 10 and 24 μs for XY4 with $N = 8$ (see Fig. 4.5). At $t = 4.4$ ţs the measured process matrix nearly equals the identity process matrix ξ (fidelity of 0.96 ± 0.02) indicating close-to-perfect quantum state protection. At longer free evolution times the process changes into pure dephasing in accordance with our model of the spin bath.

For applications in quantum information processing, it is essential that the decoupling protocol is universal, meaning that it can preserve coherence for arbitrary quantum states. As pulse errors can severely degrade the coherence, universal decoupling requires robustness to pulse errors for all possible quantum states. In contrast, protocols that employ single-axis decoupling such as CPMG optimally preserve only a limited range of quantum states, whereas for other quantum states the pulse errors accumulate rapidly with increasing number of control pulses. In Fig. 4.2c we demonstrated this experimentally by comparing the decay curves of superposition states aligned ($|x\rangle$) and perpendicular ($|y\rangle$) to

the CPMG decoupling axis. Even though the fidelity of the single-pulse control was very high (see section 4.6) the remaining small errors caused a significant loss of decoupling fidelity for state $|y\rangle$ when the number of operations was increased to 12 pulses; this effect was accurately reproduced by simulations (Fig. 4.2c) [22].

The use of sequences containing decoupling pulses over two axes, such as XY4 (Fig. 4.2d) [28] avoids this selective robustness to pulse errors and can compensate certain systematic pulse errors and coherent resonant perturbations without increasing control overhead. We found that XY4 is indeed capable of preserving both quantum states $|x\rangle$ and $|y\rangle$ (Fig. 4.2d).

We studied the decoupling performance in more detail with the use of quantum process tomography (QPT), which allows for a complete characterization of any quantum process [29]. Figure 4.3 shows the experimental QPT results for XY4 with $N = 8$ operations, at different free evolution times. For a free evolution time of 4.4 microseconds, much longer than T_2, the measured process matrix ξ is in excellent agreement with the ideal process of identity that is expected for perfect universal decoupling.

By taking snapshots of the process for different free evolution times, we monitored how decoherence affects the quantum states. We observed that after $t = 10$ μs the process element corresponding to identity had decreased, while the $\sigma_z - \sigma_z$ element had grown. After 20 μs these elements had approximately equal amplitudes. This behavior is characteristic for pure, off-diagonal dephasing [29] and is consistent with our model of the environment, in which the magnetic dipolar coupling with the bath leads to phase randomization. The independently measured energy relaxation time $T_1 > 1$ ms (see section 4.6) confirmed that longitudinal decay is not relevant in this regime.

4.5 Scaling of the coherence time with the number of pulses N

Finally, we investigated how the coherence time scales with the number of control pulses. A detailed theoretical analysis showed that for N perfect pulses, the decoupling fidelity decayed as $F(t) = \exp[-ANt^3/(2N\tau_C)^3]$, where the total free evolution time $t = 2N\tau$ and τ is the inter-pulse distance. For the XY4 sequence, we found $A = (2/3)b^2 2\tau_C^2$ for both large and small N. The theory predicts two interesting features: first, the decay follows the universal form $\exp[-(t/T_{\rm coh})^3]$ for all N, and second, the $1/e$ decay time scales as $T_{\rm coh}(N) = T^2 N 2/3$.

In Fig. 4.4a we show XY4 decoupling for $N = 4$, 16, 72, as well as the spin echo for comparison. These data indicate that the $1/e$ decay time indeed scales with the number of pulses. For a thorough comparison with the theory we renormalized the time axis to $T_2 N^{2/3}$ (Fig. 4.4b). We found that all data

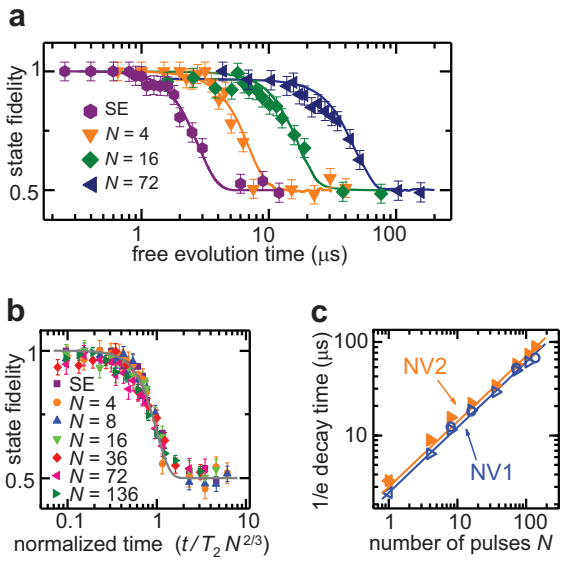

Figure 4.4: **(a)** Decoupling for different number of control pulses N. Increasing N extends the coherence to longer times. Solid lines are simulations [22]. **(b)** Data rescaled to the normalized time axis $t/(T_2 N^{2/3})$. **(c)** Coherence $1/e$ decay time (T_{coh}) plotted as a function of the number of control pulses for NV1 and NV2. Solid lines are fits to $T_{\mathrm{coh}}(N) = T_2 N^{2/3}$ with T_2 as free parameter.

collapse onto a single curve in line with the prediction. Then, we plotted the 1/e decay time of coherence of NV1 and NV2, and fit to the expected scaling law. The data of both NV centers showed excellent agreement with the theory over a range in N spanning two orders of magnitude. For the longest sequence applied (136 pulses) the coherence time was increased by a factor of ~ 26.

Is there a limit to the coherence enhancement that can be achieved with dynamical decoupling? Our results demonstrate that we can prolong the spin coherence beyond the bath correlation time τ_C. Also, the nuclear spin bath, which would affect the NV dynamics on a 5-microsecond timescale for the magnetic field used here [14], is efficiently decoupled from the NV spin. In fact, the theory indicates no fundamental limit to the coherence time. In practice the decoupling efficiency will be limited by the minimum inter-pulse delay (of the order of the pulse widths), and the longitudinal relaxation time.

Because the spin bath environment is common to solid-state quantum bits, our findings can be transferred to other promising systems such as spins in quantum dots [3,18,19] and donors in silicon [4,20]. Furthermore, the performance of

spin-based magnetometers can greatly benefit from this work, because the magnetic field sensitivity scales with the coherence time [7, 8]. Finally, dynamical decoupling can be applied to protect entangled states, which are at the heart of quantum information science.

4.6 Additional material

Quantifying the decoupling fidelity

The performance of decoupling sequences can be characterized by different figures of merit. One of them is state preservation fidelity, which is defined as the overlap of the initial state Ψ_{in} with the state at the end of the sequence, i.e. $F_s = \langle\Psi_{\rm in}|\,\rho_{\rm out}\,|\Psi_{\rm in}\rangle$ [29]. The state density matrix $\rho_{\rm out}$ can be found by reading the spin projections $(\langle S_x\rangle, \langle S_y\rangle, \langle S_z\rangle)$ along three orthogonal axes. In practice, this is accomplished by applying a final pulse to rotate the spin instead of the measurement basis, which is restricted to the quantization axis. The state can then be reconstructed $\rho_{out} = \frac{I}{2} + \langle S_x\rangle\,\sigma_x + \langle S_y\rangle\,\sigma_y + \langle S_z\rangle\,\sigma_z$. However, noise in the measurement can result in unphysical density matrices resulting from state tomography, yielding state vectors with a norm $r_\rho = \sqrt{\langle S_x\rangle^2 + \langle S_y\rangle^2 + \langle S_z\rangle^2} > 0.5$. When this occurs the measured x, y and z-components are normalized by r_ρ.

A more general way to characterize the process is through quantum process tomography (QPT). A process can be identified by its effect on an arbitrary state with the relation $\rho_{\rm out} = \sum_{i,j}\chi_{ij}E_i\rho_{\rm in}E_j^\dagger$, where $\{E_i\} = \{\sigma_x, \sigma_y, \sigma_z, I\}$. For a single qubit, the protocol consists of applying the process to a basis of four input states (see Fig. 4.5). Knowledge of the resulting output states is sufficient to reconstruct the matrix elements χ_{ij}. Also in this case noise will introduce errors. This can result in an unphysical process since it can introduce unphysical correlations between the four density matrices measured for each input state. With a technique akin to maximum likelihood estimation [30], we find an estimate of the actual physical process matrix $\chi^{\rm est}$ by imposing the trace-preserving constraint $\sum_i \chi_{ij}^{\rm est}E_i^\dagger E_j = I$, while minimizing the distance from the measured matrix elements $\sum_{i,j}|\chi_{ij}^{\rm est} - \chi_{ij}^{\rm meas}|^2$. The optimization search is performed with the Python function fmin_slsqp in the scipy.optimize package. If the process is a single pulse, its accuracy is assessed through the process fidelity $F = {\rm Tr}(\chi^{\rm ideal}\chi^{\rm est})$, where $\chi^{\rm ideal}$ is the matrix describing a perfect pulse. Similarly, when the process is a decoupling sequence, its performance is given by the same equation, where $\chi^{\rm id}$ specifies the identity process.

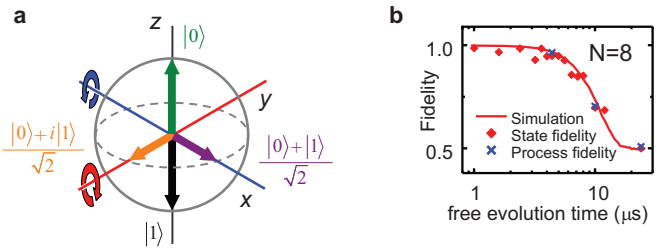

Figure 4.5: **(a)** Bloch sphere representation of the reference states for QPT. The qubit is prepared in four independent reference states $\{|0\rangle, |1\rangle, (|0\rangle + |1\rangle)/\sqrt{(2)}, (|0\rangle - i|1\rangle)/\sqrt{(2)})\}$. After the decoupling process is applied, the resulting state ρ_m is reconstructed using state tomography, which involves measuring its projection on the x, y and z axis. **(b)** Two-cycle XY4 sequence with $N = 8$ control pulses for NV1. Data points are state fidelities measured at varying free evolution times. Solid line is a simulation including pulse errors. Blue crosses are measured process fidelities determined with QPT, where fidelity $F_p = 1$ implies the identity operation.

Ramsey interference

Ramsey fringes are characteristic of an NV center and its environment, yielding the free induction decay time, the hyperfine coupling with the N nuclear spin and the qubit energy splitting. The experiment is performed by applying the sequence $\frac{\pi}{2}_x - \tau - \frac{\pi}{2}_x$, where τ is a variable free evolution time. Fig. S3a shows the measured probability that the spin is in state $|0\rangle$ as a function of τ with a detuning $\delta\omega \approx 15\,\mathrm{MHz}$ from the transition frequency for NV2. The beating of three signals is a clear indication of the hyperfine coupling with a ^{14}N nucleus ($H_{hf} = \omega_{hf} I_z$, with $I_z = 0, \pm 1$ and $\omega_{hf} = 2\pi \cdot 2.2\,\mathrm{MHz}$ [31]). The data are well reproduced by the fitting function:

$$P_{|0\rangle}(t) = \exp\left\{-\frac{1}{2}b^2t^2\right\}\frac{1}{3}\sum_{k=-1}^{1} P_k \cos[(\delta\omega + k\omega_{\mathrm{hf}})t + \phi], \tag{4.1}$$

where the Gaussian envelope accounts for the dephasing due to the slow spin bath (see main text). The different values of the fit parameters P_0, P_1, P_{-1} is a signature of partial polarization of the nuclear spin, which indicates that the field is properly aligned with the NV center [32]. A common phase ϕ is introduced to include the effect of a rotation axis error in the $\pi/2$ pulses, arising from the detuning $\delta\omega$. (Note that for all other experiments $\delta\omega$ is set to zero to achieve optimal pulse fidelities.)

Additional data

In Fig. 4.5 we show the decay curve for the sequence used in Fig. 4.3 of the main text, with the three free evolution times indicated where QPT has been performed. In Fig. 4.6b we also present additional measurements on NV2 analogous to Figs. 4.1c, 4.1a and b on NV1 in the main text. The same behavior was observed for NV2 as for NV1, both in the coherence enhancement and in the decay shape. Fig. 4.7 shows a measurement of the spin relaxation on NV1, yielding $T_1 > 1$ ms.

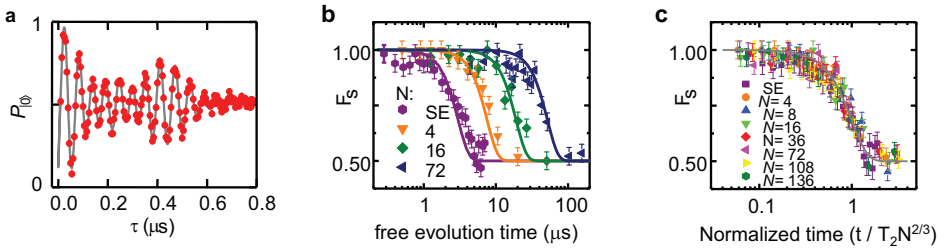

Figure 4.6: **(a)** Measurement of the Ramsey fringes of NV2. The fit to Eq.(4.1) yields the detuning $\omega = 2\pi$ (15.67 ± 0.01) MHz, and the nuclear polarization $P_{1,0,-1} = 0.50, 0.30, 0.20$ (all ± 0.01). **(b)** XY4 for increasing N for NV2. **(c)** Coherence decay curves for NV2 on a normalized time axis.

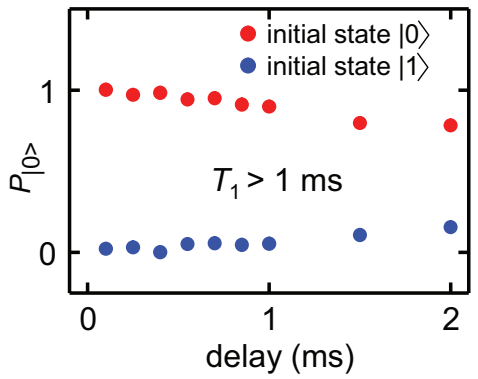

Figure 4.7: Decay of initial states $|0\rangle$ and $|1\rangle$ due to spin relaxation measured by varying the delay between initialization and read out for NV1.

Dynamical decoupling sequences

In our work, the spectrum of noise has Lorentzian shape (unless extremely high frequencies $\omega_{\rm uv}$ are considered), which decreases very slowly at high frequencies. Previous investigations [26, 27, 33, 34] show that for such a noise spectrum, the periodic CPMG-type sequences would perform well, while Uhrig's decoupling sequence would demonstrate sub-optimal performance. This is also confirmed by our experimental results. Thus, we focus our analysis on the case of periodic sequences with CPMG-like pulse timings.

We consider evolution of the central spin between times $t = 0$ and $t = T$. To analyze a complex pulse sequence, where the operator S_z changes sign many times in a complex fashion, we introduce a time-domain filter function $\xi(t)$, which equals $+1$ at $t = 0$, and changes sign after each pulse [27, 35–37]. We assume that $\xi(t) = 0$ at $t < 0$ and at $t > T$. The signal at $t = T$, after application of the pulse sequence characterized by the function $\xi(t)$, is

$$S(T) = \left\langle \exp\left(-i\int_0^T \xi(s)B(s)ds\right)\right\rangle. \tag{4.2}$$

Since $B(t)$ is an OU process with zero average, the averaging can be done explicitly [38] to give $S(T) = \exp\left[-b^2\, W(T)\right]$ where

$$W(T) = \int_0^T ds \exp\left(-Rs\right) \int_0^{T-s} \xi(t)\xi(t+s)dt. \tag{4.3}$$

We assume that the decoupling sequence contains N cycles, each of duration T_c (so that $T = NT_c$). Each cycle is characterized by the filter function $\xi_0(t)$. The latter is defined analogously to $\xi(t)$: it is zero at $t < 0$ and $t > T_c$ (where T_c is the period of the sequence), has initial value $+1$ at $t = 0$, and changes sign after each pulse.

The dephasing exponent $W(T)$ can be expressed in terms of $\xi_0(t)$. First, we calculate the integral $W(T)$ by breaking the domain $[0, T]$ of s into N pieces of length T_c:

$$W(T) = \left\{\int_0^{T_c} + \int_{T_c}^{2T_c} + \ldots\right\} \mathrm{e}^{-Rs} p(s)ds = \sum_{m=0}^{N-1} \int_{mT_c}^{(m+1)T_c} \mathrm{e}^{-Rs} p(s)ds \tag{4.4}$$

where $p(s)$ is the convolution integral $p(s) = \int_0^{T-s} \xi(t)\xi(t+s)dt$.

Next, we calculate $p(s)$ at each segment $s \in [mT_c, (m+1)T_c]$ separately. We represent $s = mT_c + s'$ (with $s' < T_c$), and take into account that $\xi(t)$ and $\xi(t+s)$

overlap over $N-m$ full cycles. This gives

$$p(s) = \int_0^{T-s} \xi(t)\xi(t+s)dt = (N-m)\int_0^{T_c-s'} \xi_0(t)\xi_0(t+s')dt \quad (4.5)$$
$$+ \quad (N-m-1)\int_0^{s'} \xi_0(t)\xi_0(t+T_c-s')dt,$$

where the second term in the sum takes into account the non-overlapping part. It is convenient to represent $p(s)$ in the form

$$p(s) = (N-m)[q_{11}(s')+q_{12}(s')] - q_{12}(s') \quad (4.6)$$
$$q_{11}(s') = \int_0^{T_c-s'} \xi_0(t)\xi_0(t+s')dt$$
$$q_{12}(s') = q_{11}(T_c-s') = \int_0^{s'} \xi_0(t)\xi_0(t+T_c-s')dt.$$

We substitute this answer into Eq. 4.4, and take into account that $\mathrm{e}^{-Rs} = \mathrm{e}^{-mRT_c}\mathrm{e}^{-Rs'}$. As a result, we obtain:

$$W(T) = -\int_0^{T_c} \mathrm{e}^{-Rs'} q_{12}(s')ds' \cdot \{1 + \mathrm{e}^{-RT_c} + \mathrm{e}^{-2RT_c} + \dots \quad (4.7)$$
$$+ \quad \mathrm{e}^{-(N-1)RT_c}\} \quad (4.8)$$
$$+ \quad \int_0^{T_c} \mathrm{e}^{-Rs'}[q_{11}(s')+q_{12}(s')]ds' \cdot \{N + (N-1)\mathrm{e}^{-RT_c}$$
$$+ \quad (N-2)\mathrm{e}^{-2RT_c} + \dots\} \quad (4.9)$$

Now, we need to calculate the two sums (denoted by curly brackets) appearing in the expression above. The first sum is the simple geometric progression, its value is

$$P_N = \sum_{m=0}^{N-1} \mathrm{e}^{-mRT_c} = \frac{1-\exp(-NRT_c)}{1-\exp(-RT_c)}. \quad (4.10)$$

The second sum is

$$\Sigma_N = \sum_{m=0}^{N-1} (N-m)\exp(-mRT_c) = NP_N - \sum_{m=0}^{N-1} m\exp(-mRT_c) \quad (4.11)$$
$$= NP_N + (1/T_c)dP_N/dR.$$

Therefore we find

$$\Sigma_N = \frac{N-(N+1)\mathrm{e}^{-RT_c} + \mathrm{e}^{-(N+1)RT_c}}{(1-\mathrm{e}^{-RT_c})^2} \quad (4.12)$$

Thus, we have a preliminary answer. We have a sequence containing N cycles, each cycle has duration T_c and is characterized by a filter function $\xi_0(t)$, so that the total evolution time is $T = T_c N$. The transverse component of the central spin is

$$S(T) = \exp\left[-b^2\, W(T)\right] \tag{4.13}$$

where

$$W(T) = \Sigma_N[Q_{11} + Q_{12}] - P_N Q_{12} \tag{4.14}$$

where the sums are

$$\begin{aligned} \Sigma_N &= \frac{N - (N+1)\mathrm{e}^{-RT_c} + \mathrm{e}^{-(N+1)RT_c}}{(1 - \mathrm{e}^{-RT_c})^2} \\ P_N &= \frac{1 - \exp\left(-NRT_c\right)}{1 - \exp\left(-RT_c\right)}. \end{aligned} \tag{4.15}$$

and the integrals are

$$\begin{aligned} Q_{11} &= \int_0^{T_c} \mathrm{e}^{-Rs} q_{11}(s) ds \\ Q_{12} &= \int_0^{T_c} \mathrm{e}^{-Rs} q_{12}(s) ds. \end{aligned} \tag{4.16}$$

The partial convolution integrals in this expression are:

$$\begin{aligned} q_{11}(s) &= \int_0^{T_c - s} \xi_0(t)\xi_0(t+s) dt \\ q_{12}(s) &= q_{11}(T_c - s) = \int_0^{s} \xi_0(t)\xi_0(t + T_c - s) dt. \end{aligned} \tag{4.17}$$

Thus, we only need to calculate $q_{11}(s)$ and $q_{12}(s)$, and Q_{11} and Q_{12} for specific sequences.

XY4 and XY8

For XY4 sequence, the full period is d-X-d-d-Y-d-d-X-d-d-Y-d, where d denotes a free evolution of duration τ. However, the filter function of a single XY4 period has a twice shorter cycle, of total length only 2τ. Thus, it is convenient to take the duration of each cycle $T_c = 4\tau$, the number of cycles N equal to twice the number of XY4 periods, and the single-cycle filter function

$$\xi_0(t) = \begin{cases} +1, & \text{for } \tau > t \geq 0 \\ -1, & \text{for } 3\tau > t \geq \tau \\ +1, & \text{for } 4\tau > t \geq 3\tau \end{cases} \tag{4.18}$$

and zero otherwise.

The convolution integrals are:

$$q_{11}(s) = \begin{cases} 4\tau - 5s, & \text{for } \tau > s \geq 0 \\ -s, & \text{for } 2\tau > s \geq \tau \\ 3s - 8\tau, & \text{for } 3\tau > s \geq 2\tau \\ 4\tau - s, & \text{for } 4\tau > s \geq 3\tau \end{cases} \tag{4.19}$$

and $q_{12}(s) = q_{11}(4\tau - s)$. Correspondingly, the integrals appearing in Eq. 4.14 are:

$$Q_{11} = [4R\tau - 5 + 4\mathrm{e}^{-R\tau} + 4\mathrm{e}^{-2R\tau} - 4\mathrm{e}^{-3R\tau} + \mathrm{e}^{-4R\tau}]/R^2 \tag{4.20}$$

and

$$Q_{12} = [1 - 4\mathrm{e}^{-R\tau} + 4\mathrm{e}^{-2R\tau} + 4\mathrm{e}^{-3R\tau} - 4R\tau\mathrm{e}^{-4R\tau} - 5\mathrm{e}^{-4R\tau}]/R^2. \tag{4.21}$$

Now, we consider the experimentally interesting case when $R\tau \ll 1$ and consider the evolution at short times, when both $RT_c \ll 1$ and $NRT_c \ll 1$, and at long times, when $RT_c \ll 1$ but $NRT_c \gg 1$. In both cases, we find the decay rate

$$W_{XY4}(T) = -N\ \frac{4}{3}(R\tau)^3\ \frac{1}{R^2}. \tag{4.22}$$

The symmetrized version of XY4, so-called XY8 sequence, does not require separate analysis. Its filter function $\xi(t)$ is the same as for the XY4 sequence, so the decay rate is also the same.

Numerical Simulations

The simulations are performed for a spin $S = 1/2$ in the rotating frame. Evolution of the spin in the random magnetic field $B(t)$, created by the bath, was modeled using the Runge-Kutta method of the 4-th order [39]. The random field $B(t)$ was modeled as an Ornstein-Uhlenbeck process [17,35,36,40–42]. with the correlation function $\langle B(0)B(t)\rangle = b^2 e^{-R|t|}$. The experimentally determined parameters from NV1 were used. The averaging was performed over 5000 realizations of $B(t)$.

The hyperfine interaction $A_0 S^z I_0^z$ between the electron spin and the nuclear spin of the NV center [17] is taken into account. Since the intrinsic relaxation time of the nuclear spin I_0 is of orders of milliseconds, for a single experimental run, I_0^z is a constant of motion [17]. The mean of the Ornstein-Uhlenbeck process is therefore taken as $\delta B + A_0 I_0^z$, where δB is the small field along z-axis. This field corresponds to the systematic detuning of the carrier frequency of the pulse from the exact resonance. For different runs, corresponding to different realizations of $B(t)$, we sample $I_0^z = +1, -1, 0$ randomly with probability $p_+ = 0.5$, $p_- =$

0.2, $p_0 = 0.3$, respectively. These values are obtained from the Ramsey fringe experiment.

The control pulses are assumed to have infinitely small width, and are treated as rotation operators. The pulse imperfections are taken into account by considering rotations with errors in both rotation axis and rotation angles. That is, for π-pulses about X and Y axis, the rotation operators are

$$\hat{X} = e^{-i(\pi+\epsilon_x)\hat{S}\cdot\vec{n}}$$

and

$$\hat{Y} = e^{-i(\pi+\epsilon_y)\hat{S}\cdot\vec{m}}$$

respectively. Here ϵ_x and ϵ_y are the rotation angle errors and

$$\vec{n} = (\sqrt{1-n_y^2-n_z^2}, n_y, n_z) \tag{4.23}$$

(close to X axis) and

$$\vec{m} = (m_x, \sqrt{1-m_x^2-m_z^2}, m_z) \tag{4.24}$$

(close to Y axis) are the rotation axis.

The pulse errors ϵ_x, ϵ_y, n_y, m_x are taken as constant for the pulses in each run and for different runs. Since the hyperfine coupling $A_0 S^z I_0^z$ serves as a main contribution to the errors n_z and m_z, these two errors are treated as static during each run, but have different values for different runs, depending on the choice of I_0^z:

$$n_z = \begin{cases} +n_0\ , & \text{if } I_0^z = 1 \\ -n_0\ , & \text{if } I_0^z = -1 \\ 0 & \text{if } I_0^z = 0 \end{cases} \tag{4.25}$$

$$m_z = \begin{cases} +m_0\ , & \text{if } I_0^z = 1 \\ -m_0\ , & \text{if } I_0^z = -1 \\ 0 & \text{if } I_0^z = 0 \end{cases} \tag{4.26}$$

The values of the parameters above are $\epsilon_x = \epsilon_y = -0.02$, $m_x = 0.005$, $n_0 = m_0 = 0.05$, $n_y = 0$, and $\delta B = -0.5$ MHz. The simulations with these parameters have been performed for Ramsey fringe, spin echo, single-axis DD, XY4 and UDD, all yielding results in very good agreement with the experimental results. The parameters characterizing the random bath field were taken from the Ramsey and the spin echo experiments as described above, $b = 3.6\ \mu\text{s}^{-1}$ and $R = 25\ \mu\text{s}^{-1}$ for NV1, and $b = 2.6\ \mu\text{s}^{-1}$ and $R = 23\ \mu\text{s}^{-1}$ for NV2, see the main text.

We note that all the simulations have been performed with the same set of parameters. For the data in Fig. 2B, we also performed the simulations without pulse errors and found the difference with the simulation results with pulse errors to be smaller than 1% for all data points. This shows that the difference between UDD and CPMG observed in Fig. 2B is not an artifact of pulse errors.

Bibliography

[1] J. Clarke and F. K. Wilhelm. Superconducting quantum bits. *Nature* **453**, 1031 (2008).

[2] R. Hanson and D. D. Awschalom. Coherent manipulation of single spins in semiconductors. *Nature* **453**, 1043 (2008).

[3] D. Loss and D. P. Divincenzo. Quantum computation with quantum dots. *Physical Review A - Atomic, Molecular, and Optical Physics* **57**, 120 (1998).

[4] B. E. Kane. A silicon-based nuclear spin quantum computer. *Nature* **393**, 133 (1998).

[5] L. Childress, J. M. Taylor, A. S. Sørensen and M. D. Lukin. Fault-tolerant quantum communication based on solid-state photon emitters. *Physical Review Letters* **96**, 070504 (2006).

[6] J. Jones *et al.* Magnetic field sensing beyond the standard quantum limit using 10-spin noon states. *Science* **324**, 1166 (2009).

[7] C. L. Degen. Scanning magnetic field microscope with a diamond single-spin sensor. *Applied Physics Letters* **92**, 243111 (2008).

[8] J. Taylor *et al.* High-sensitivity diamond magnetometer with nanoscale resolution. *Nature Physics* **4**, 810 (2008).

[9] W. Zurek. Quantum darwinism. *Nature Physics* **5**, 181 (2009).

[10] L. Viola, E. Knill and S. Lloyd. Dynamical decoupling of open quantum systems. *Physical Review Letters* **82**, 2417 (1999).

[11] D. Vitali and P. Tombesi. Using parity kicks for decoherence control. *Physical Review A - Atomic, Molecular, and Optical Physics* **59**, 4178 (1999).

[12] K. Khodjasteh and D. Lidar. Fault-tolerant quantum dynamical decoupling. *Physical Review Letters* **95**, 180501 (2005).

[13] G. Fuchs, V. Dobrovitski, D. Toyli, F. Heremans and D. Awschalom. Gigahertz dynamics of a strongly driven single quantum spin. *Science* **326**, 1520 (2009).

[14] L. Childress *et al.* Coherent dynamics of coupled electron and nuclear spin qubits in diamond. *Science* **314**, 281 (2006).

[15] L. Jiang *et al.* Repetitive readout of a single electronic spin via quantum logic with nuclear spin ancillae. *Science* **326**, 267 (2009).

[16] P. Neumann *et al.* Quantum register based on coupled electron spins in a room-temperature solid. *Nature Physics* **6**, 249 (2010).

[17] R. Hanson, V. V. Dobrovitski, A. E. Feiguin, O. Gywat and D. D. Awschalom. Coherent dynamics of a single spin interacting with an adjustable spin bath. *Science* **320**, 352 (2008).

[18] R. Hanson, L. P. Kouwenhoven, J. R. Petta, S. Tarucha and L. M. K. Vandersypen. Spins in few-electron quantum dots. *Reviews of Modern Physics* **79**, 1217 (2007).

[19] H. Bluhm *et al.* Dephasing time of gaas electron-spin qubits coupled to a nuclear bath exceeding 200 μs. *Nature Physics* **7**, 109 (2011).

[20] J. J. L. Morton *et al.* Solid-state quantum memory using the 31p nuclear spin. *Nature* **455**, 1085 (2008).

[21] J. Klauder and P. Anderson. Spectral diffusion decay in spin resonance experiments. *Physical Review* **125**, 912 (1962).

[22] Z.-H. Wang, G. de Lange, D. Ristè, R. Hanson and V. V. Dobrovitski. Comparison of dynamical decoupling protocols for a nitrogen-vacancy center in diamond. *Physical Review B* **85**, 155204 (2012).

[23] G. Uhrig. Keeping a quantum bit alive by optimized π-pulse sequences. *Physical Review Letters* **98**, 100504 (2007).

[24] M. Biercuk *et al.* Optimized dynamical decoupling in a model quantum memory. *Nature* **458**, 996 (2009).

[25] J. Du *et al.* Preserving electron spin coherence in solids by optimal dynamical decoupling. *Nature* **461**, 1265 (2009).

[26] S. Pasini and G. Uhrig. Optimized dynamical decoupling for power-law noise spectra. *Physical Review A - Atomic, Molecular, and Optical Physics* **81**, 012309 (2010).

[27] L. Cywiński, R. Lutchyn, C. Nave and S. Das Sarma. How to enhance dephasing time in superconducting qubits. *Physical Review B - Condensed Matter and Materials Physics* **77**, 174509 (2008).

[28] T. Gullion, D. Baker and M. Conradi. New, compensated carr-purcell sequences. *Journal of Magnetic Resonance (1969)* **89**, 479 (1990).

[29] M. A. Nielsen and I. Chuang. *Quantum Computation and Quantum Information*. Cambridge University Press, 2000.

[30] D. James, P. Kwiat, W. Munro and A. White. Measurement of qubits. *Physical Review A* **64** (2001).

[31] M. Steiner, P. Neumann, J. Beck, F. Jelezko and J. Wrachtrup. Universal enhancement of the optical readout fidelity of single electron spins at nitrogen-vacancy centers in diamond. *Physical Review B* **81**, 035202 (2010).

[32] V. Jacques *et al.* Dynamic Polarization of Single Nuclear Spins by Optical Pumping of Nitrogen-Vacancy Color Centers in Diamond at Room Temperature. *Physical Review Letters* **102** (2009).

[33] G. S. Uhrig. Exact results on dynamical decoupling by π pulses in quantum information processes. *New Journal of Physics* **10**, 083024 (2010).

[34] H. Uys, M. J. Biercuk and J. J. Bollinger. Optimized noise filtration through dynamical decoupling. *Physical Review Letters* **103**, 040501 (2009).

[35] J. Klauder and P. Anderson. Spectral Diffusion Decay in Spin Resonance Experiments. *Physical Review* **125**, 912 (1962).

[36] R. de Sousa and S. Das Sarma. Theory of nuclear-induced spectral diffusion: Spin decoherence of phosphorus donors in Si and GaAs quantum dots. *Physical Review B* **68**, 115322 (2003).

[37] L. CywiÅĎski, W. Witzel and S. Das Sarma. Pure quantum dephasing of a solid-state electron spin qubit in a large nuclear spin bath coupled by long-range hyperfine-mediated interactions. *Physical Review B* **79**, 245314 (2009).

[38] R. Kubo, M. Toda and N. Hashitsume. *Statistical Physics II.* Springer, Berlin, New York (1998).

[39] G. Milstein and M. Tretyakov. *Stochastic Numerics for Mathematical Physics.* Springer, Berlin, New York (2004).

[40] R. Kubo. No Title. *Journal of the Physical Society of Japan* **17**, 1100 (1962).

[41] C. Slichter. *Principles of Magnetic Resonance.* Springer, third edition (1990).

[42] V. V. Dobrovitski, A. E. Feiguin, R. Hanson and D. D. Awschalom. Decay of rabi oscillations by dipolar-coupled dynamical spin environments. *Physical Review Letters* **102**, 237601 (2009).

Chapter 5

Single-spin magnetometry with multi-pulse sensing sequences

G. de Lange, D. Ristè, V.V. Dobrovitski and R. Hanson

We experimentally demonstrate single-spin magnetometry with multi-pulse sensing sequences. The use of multi-pulse sequences can greatly increase the sensing time per measurement shot, resulting in enhanced ac magnetic field sensitivity. We theoretically derive and experimentally verify the optimal number of sensing cycles, for which the effects of decoherence and increased sensing time are balanced. We perform these experiments for oscillating magnetic fields with fixed phase as well as for fields with random phase. Finally, by varying the phase and frequency of the ac magnetic field, we measure the full frequency-filtering characteristics of different multi-pulse schemes and discuss their use in magnetometry applications.

This chapter has been published in Physical Review Letters **106**, 080802 (2011).

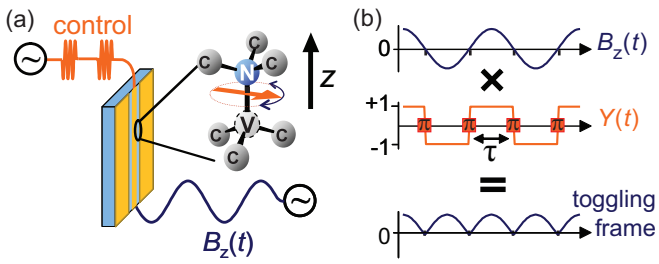

Figure 5.1: **(a)** Magnetometry setup. A CPW transmission line, fabricated directly on a Ib diamond sample, is connected to control lines on both ends. One control line supplies 2.5 GHz microwave bursts for spin control. For details of this part of the setup see Ref. [8]. We use the other side of the CPW to supply the low frequency (< 5 MHz) ac field $B_z(t)$ that we aim to detect. A single NV center located in between the conductors of the CPW is used as the magnetometer. **(b)** Multipulse magnetometry. An ac field $B_z(t)$ modulates the phase of the NV electron spin. Timing π-pulses such that they coincide with the nodes of $B_z(t)$ effectively multiplies the field by $Y(t)$. The bottom trace shows the resulting $B_z(t)$ in the toggling reference frame, which flips whenever a π-pulse is applied to the spin.

5.1 Introduction

The ability to sense weak magnetic fields with nanometer scale resolution has important applications in fundamental and biomedical sciences as well as information storage technology. Several architectures for highly sensitive magnetometers have been implemented, such as superconducting quantum interference devices (SQUIDS) [1], Hall sensors [2], sensors based on magnetic resonance force microscopy (MRFM) [3] and atomic vapors [4]. Recently, approaches to magnetometry based on tracking the evolution of a single electron spin have been proposed [5–7].

The magnetic field to be detected shifts the energy levels of the spin through the Zeeman effect. When a superposition of spin states is prepared, the Zeeman shift leads to a phase difference proportional to the magnetic field, which can be detected as a population difference after application of a suitable control pulse.

5.2 The NV center as single-spin magnetometer

The nitrogen vacancy (NV) defect center in diamond is a prime candidate for single-spin magnetometry [6, 7, 9–13]. The NV center combines an excellent field sensitivity with high spatial resolution resulting from the near-atomic size of the defect. It has a ground state paramagnetic spin (S=1) with the $m_s = 0$ and

$m_s = \pm 1$ levels split by 2.87 GHz at zero magnetic field, with the quantization axis oriented along the symmetry axis of the defect. The NV center spin can be initialized and its spin population difference can be detected optically by measuring its spin-dependent photoluminescence (PL) [14]. First experimental demonstrations of NV-based magnetometry using a sensing sequence with a single π-pulse (spin echo) have outlined its potential as an ultra-sensitive detector [9–11]; even better performance can be achieved by applying more control pulses [7, 15].

Here, we present a detailed experimental study of single NV center magnetometry with multi-pulse sensing sequences. We demonstrate that multi-pulse sequences greatly improve the sensitivity to oscillating magnetic fields. We find the optimal number of control pulses as function of field frequency and spin-echo decay time. These studies are performed both for fields with known phase and for fields with a phase that randomly fluctuates between measurement shots. We finally show that multi-pulse sequences can be used to achieve a high degree of frequency tunability and selectivity by exploiting their frequency-domain characteristics.

5.3 Experimental setup

We use a single NV center in a nitrogen-rich Ib bulk diamond sample (Element Six) as our magnetometer. The setup is shown schematically in Fig. 1(a). We apply a static magnetic field oriented along the NV center's quantization axis z that allows us to selectively address the $m_s = 0 \leftrightarrow m_s = -1$ spin transition. Within this subspace, the NV spin is equivalent to a spin-1/2. Using lithographically defined on-chip coplanar waveguides (CPWs) [16] we achieve high fidelity ($\approx$99%) control of the NV center electron spin state [8,29]. The length of a single π-pulse used here is $t_p = 8$ ns. With the CPW low-frequency magnetic fields can be applied along the z-axis as well.

5.4 General principle of single-spin magnetometers

We consider a time-varying oscillating magnetic field oriented along the quantization axis z of the probing spin $B_z(t) = b_z \sin(2\pi f t + \phi)$. Components oscillating along the transverse axes will average to zero due to the rapid (2.5 GHz) precession of the NV spin. The working principle behind detecting a field of the form $B_z(t)$ is outlined in Fig. 1(b). An electron spin initialized in a superposition state precesses under the influence of the oscillating field. During each half-cycle the electron spin phase acquires $\delta\Phi = \int_0^{1/2f} 2\pi\gamma B_z(t)dt = (2\gamma b_z/f)\cos\phi$, with

$\gamma = 28$ GHz/T for the electron spin of an NV center. Since the field oscillates the total phase after many cycles averages to zero. This can be prevented by using an N-pulse sequence with evenly spaced π-pulses

$$[\tau/2 - \pi - \tau - \pi - \tau/2]^{N/2}. \tag{5.1}$$

Note that this sequence has the same timing properties as the Carr-Purcell sequence (CP) [17] known from NMR. CP-like sequences have very recently been explored with NV centers in the context of dynamical decoupling from decoherence by a spin bath environment [15, 18, 29]. When the π-pulses of the sequence coincide with the nodes of $B_z(t)$, the electron accumulates a phase which increases with the length of the sequence. This can be understood by moving to the toggling reference frame of the electron spin from where $B_z(t) \to -B_z(t)$ after each π-pulse. Formally, $B_z(t)$ is multiplied by a time-domain filter function $Y(t)$ which changes sign each time a π-pulse is applied (Fig. 1(b)). After N π-pulses (or half-cycles) the total phase of the electron spin state becomes $\Delta\Phi = N\delta\Phi$.

5.5 Phase-locked magnetometry

We first analyze the case when $B_z(t)$ always has the same phase relation with respect to the sequence of π-pulses ($\phi = 0$) [6,7]. This corresponds to a situation where the phase of the field to be measured is under control of the experimenter (e.g. when one aims to detect spins that can be adiabatically inverted periodically). In this case, for a spin initialized along the x-axis, the read out can be performed by rotating the final state by $\pi/2$ around the same axis (see Fig. 2(a)). The resulting signal is then $S_z(b_z) = \frac{1}{2}\sin[(2N\gamma b_z/f)\cos\phi]$ after normalization of the PL levels to $\left[-\frac{1}{2}, \frac{1}{2}\right]$.

In Fig. 2(b) we monitor the evolution of the NV electron spin under application of an ac field with frequency $f = 1$ MHz for increasing N. The ac field is phase-locked such that the π-pulses coincide with the nodes of $B_z(t)$. We observe oscillations which demonstrate spin precession in the applied ac field. The amplitude of the oscillations decays exponentially due to decoherence and pulse imperfections. We can limit the influence of pulse imperfections on the signal decay by using the XY4 sequence which is self-compensating for pulse errors [19] and has the same timings as Eq. (5.1). We find the maximum number of pulses that can be applied before pulse errors start to play a role to be ~ 130 pulses [29].

In our type Ib diamond sample the coherence time is limited by dipolar interactions with electron spins, which are located at the sites of substitutional nitrogen atoms in the diamond lattice [20]. The one-pulse spin-echo signal decays as $\sim \exp[-(\tau/T_2)^3]$ where $T_2 = (2.8 \pm 0.1)$ μs for the NV center used here [29]. Increasing the number of pulses to N reduces the signal by a fac-

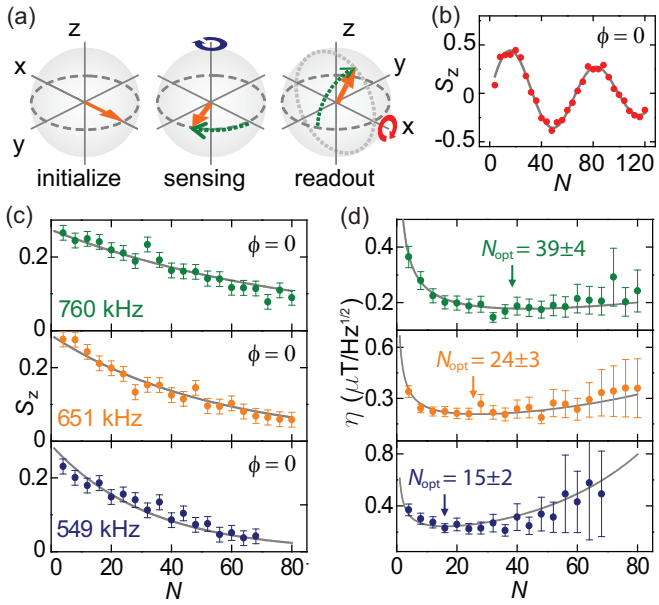

Figure 5.2: Phase-locked magnetometry. **(a)** Measurement scheme. A spin initialized along the x-axis will accumulate a phase during the sensing stage due to $B_z(t)$. A final rotation around the x-axis is applied to transform the phase into a population difference. **(b)** A 1 MHz ac field with constant amplitude is measured with increasing number of pulses N. Solid line is a fit to Eq. (5.2), yielding $b_z = 1.6$ μT. **(c)** Signal for three ac fields with different frequency. The amplitude is rescaled by $1/N$. Solid lines are fits to Eq. (5.2) yielding $2N\gamma b_z/f \approx 0.2\pi$ and $T_2 = (2.86 \pm 0.04)\mu s$ **(d)** Sensitivities calculated from the data (points) and from the fits (solid lines) in (c).

tor $\sim \exp[-N(\tau/T_2)^3]$ for the CP sequence, which leads to the observed exponential decay in the signal in Fig. 2(b). For $B_z(t)$ oscillating with frequency $f = [2(\tau + t_p)]^{-1} \approx (2\tau)^{-1}$ (assuming $t_p \ll \tau$) this gives a total signal of

$$S_z(b_z) = \frac{1}{2} \sin\left(\frac{2N\gamma b_z}{f} \cos\phi\right) e^{-N/(2fT_2)^3}. \tag{5.2}$$

The optical detection of the spin population is limited by shot noise, which depends on the experimental parameters such as the number of photons collected per measurement shot ς and the contrast C which combine to give the noise per measurement shot $\sigma_{S_z} \approx 1/(C\sqrt{\varsigma})$ [7, 21]. The sensitivity for detecting a field oscillating in phase ($\phi = 0$) is given by combining the shot-noise limited minimum detectable field $b_{\min} = \sigma_{S_z}|\mathrm{d}b_z/\mathrm{d}S_z| \approx \sigma_{S_z}\frac{f}{\gamma N}$ and the total integration time $T = N(\tau + t_p) = N/2f$ to give

$$\eta\,(f, N) = b_{\min}\sqrt{T} = \frac{1}{\gamma C}\sqrt{\frac{f}{2\varsigma N}} e^{N/(2fT_2)^3}. \tag{5.3}$$

It is instructive to consider two limiting cases. If $N \ll 2fT_2$, decoherence is negligible and the use of a multi-pulse sequence improves the sensitivity by a factor $1/\sqrt{N}$. In the other extreme, where $N \gg 2fT_2$, decoherence has a detrimental influence on the sensitivity: $\eta \propto e^{N/(2fT_2)^3}$. Thus, for a given frequency of $B_z(t)$ there exist an optimum number of pulses N_{opt}. By minimizing η we find $N_{\mathrm{opt}} = 4T_2^3 f^3$.

In Fig. 2(c) we demonstrate the detection of ac magnetic fields of three different frequencies, for increasing N. In order to keep the signal in the linear regime the amplitude of the field is rescaled as N increases so that the total acquired phase after applying the sequence remains constant. For every measurement shot we also measure the zero-field signal to account for possible drifts in the setup. From the curves in Fig. 2(c) the sensitivity is calculated and depicted in Fig. 2(d), along with the predicted N_{opt} (calculated using the independently determined $T_2 = (2.8 \pm 0.1)\mu$s). We observe that there indeed exists an optimum number of pulses for each frequency and find excellent agreement between the predicted N_{opt} and the data.

5.6 Magnetometry of signals with random phases

We now turn to the case where $B_z(t)$ has a phase which varies randomly between measurement shots, but remains constant during each individual measurement shot. The phase that a spin, initialized along x, acquires will be different for each measurement shot with zero average, as depicted in Fig. 3(a). Rotating the

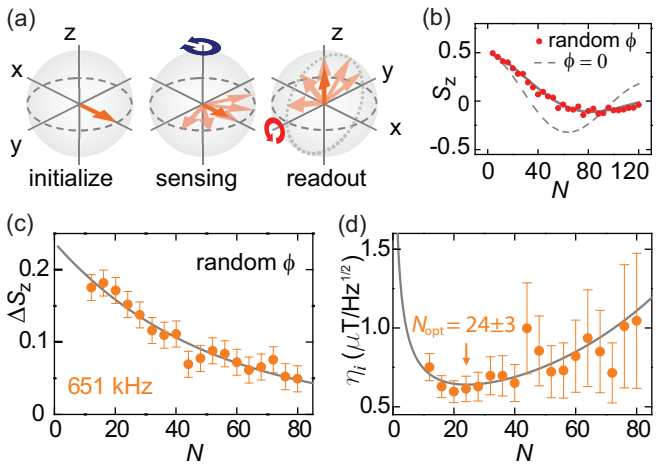

Figure 5.3: Magnetometry for ac fields with random phase. **(a)** Measurement scheme. In each measurement shot the spin, initialized along the x-axis, accumulates a different phase during the sensing stage that depends on ϕ. A signal can nonetheless be measured by applying the final $\pi/2$ rotation over the y-axis. **(b)** Measured signal for a field with constant amplitude and averaged over ϕ for increasing N. Solid line is a fit to Eq. (5.4); the expected signal for $\phi = 0$ (dashed) is included as a reference. **(c)** Signal intervals for a random-phase ac field of 651 kHz. The amplitude b_z is rescaled by $1/N$. Solid line is a fit to Eq. (5.4) yielding $2N\gamma b_z/f \approx 0.47\pi$ and $T_2 = (2.77 \pm 0.05)\mu s$. **(d)** Interval sensitivities calculated from the data (points) and from the fit (solid line) in (c).

final state over the x axis therefore yields zero signal when averaged over many measurements. However, as shown in Fig. 3(a), the state can also be rotated around the (orthogonal) y-axis. This will give a signal, when averaged over the phase, of

$$\begin{aligned} S_z(b_z) &= \frac{1}{2}\left\langle \cos\left(\frac{2N\gamma b_z}{f}\cos\phi\right)\right\rangle_\phi e^{-N/(2fT_2)^3} \\ &= \frac{1}{2}J_0\left(\frac{2N\gamma b_z}{f}\right) e^{-N/(2fT_2)^3} \end{aligned} \tag{5.4}$$

where $\langle\rangle_\phi$ denotes averaging over ϕ and J_0 is the zeroth-order Bessel function of the first kind. In the absence of any field $S_z(0) = \frac{1}{2}$. The data in Fig. 3(b) demonstrate that we can also detect the ac magnetic field if it has a random phase.

A consequence of measuring the x-projection is that $|\mathrm{d}S_z/\mathrm{d}b_z| \approx 2N^2\gamma^2 b_z/f^2$ will vanish as $b_z \to 0$, leading to a divergence in the differential sensitivity.

We therefore turn to calculating the interval sensitivity [22] by extending the definition of the minimum detectable field per measurement shot to that measured for a given signal interval: $b_{\min} = \sigma_{S_z} b_z / |S_z(b_z) - S_z(0)|$. The interval sensitivity η_i for measuring oscillating fields with random phase is given by

$$\eta_i\left(f, N, b_z\right) = \frac{2 b_z \sigma_{S_z}}{\left|J_0\left(2N\gamma b_z / f\right) - 1\right|} \sqrt{\frac{N}{2f}} e^{\frac{N}{(2fT_2)^3}}. \tag{5.5}$$

Analogously to the phase-locked experiment, we verify this expression experimentally in Fig. 3(c). The corresponding calculated interval sensitivities are depicted in Fig. 3(d). It shows a qualitatively similar picture as for the phase-locked case. Since we rescale b_z by $1/N$, also here $N_{\text{opt}} = 4T_2^3 f^3$. Again, we observe that the theory gives an excellent description of the data.

5.7 Frequency response

Until now we discussed the situation where the sequence was tuned exactly in resonance with $B_z(t)$. In order to analyze what happens when the sequence is detuned with respect to $B_z(t)$ (so $\tau \neq \frac{1}{2f}$) we move to the frequency domain. For a sequence of evenly spaced pulses and $\phi = 0$ the response of the magnetometer in the frequency domain is given by [7]

$$Y_N(f, \tau) = \frac{1 - \sec(\pi f \tau)}{2\pi \tau f} \sin(2\pi N f \tau). \tag{5.6}$$

Figure 4(a) depicts the signal detected as a function of frequency of $B_z(t)$ (with $\phi = 0$) for $N = 4$ to 80 for fixed τ, mapping out the complete filter function Eq. (5.6). Figure 4(b) shows line traces for three different N. With increasing N, the bandwidth of the response decreases by a factor N while the peak signal increases N times. Therefore, by tuning τ a single frequency component can be selected. This is useful for measuring the linewidth of $B_z(t)$ or for spectroscopic applications. The resolution is set by the full-width at half-maximum (FWHM) $\Delta f \approx 0.3/(N\tau)$.

We study the influence of the phase of $B_z(t)$ in more detail by performing a measurement at a fixed number of pulses for a range of initial phases. The results are depicted in Fig. 4(c). By averaging over the phase the response to fields with random phase is retrieved (see top panel of Fig. 4(c)). The filter function of sequences other than CP-like sequences can be investigated in a similar way.

The Uhrig dynamical decoupling (UDD) sequence [23] has been conjectured as a valuable tool in detecting randomly fluctuating fields [24]. The N-pulse

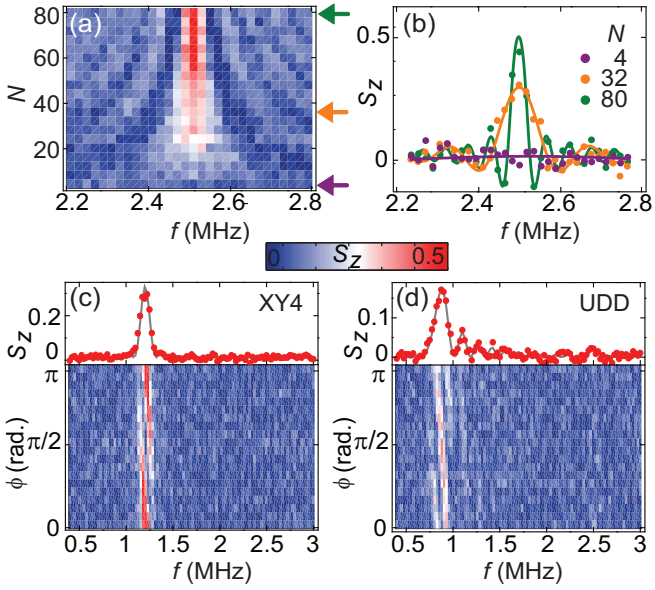

Figure 5.4: Frequency domain analysis. **(a)** Measured filter response $Y_N(f,\tau)$ of the CP sequence vs. frequency for a field amplitude of $b_z \approx 0.8$ μT for $\phi = 0$ and $\tau = 192$ ns. The scheme for measuring a phase-locked signal from Fig. 2(a) is used. A maximum signal is observed at $f = 2(\tau + t_{\rm p})^{-1} = 2.5$MHz. As N is increased the bandwidth reduces and peak signal becomes higher. **(b)** Line traces from (a). Solid lines are fits using Eq. (5.6). **(c)** Magnetometer response vs. frequency and phase using the CP-like XY4 sequence with $N = 20$ pulses and 8.16 μs integration time ($\tau = 400$ ns). The field amplitude is adjusted to ~ 1.7 μT. The scheme for measuring a random phase signal from Fig. 3(a) is used. **(d)** Signal for the same field and integration time measured in (c) but now using the 20-pulse aperiodic UDD sequence. The upper panels in (c) and (d) depict the signal averaged over the phase.

UDD sequence has pulses spaced irregularly according to $\tau_k = \sin^2[\pi k/(2N+2)]$ with τ_k the k-th pulse spacing. A characterization of the UDD sequence similar to Fig. 4(c) is presented in Fig. 4(d). UDD is seen to give a broader frequency response and reduced peak signal compared to a sequence with CP-like timings (Eq. (5.1)). The higher peak signal and reduced bandwidth of the latter is especially useful when gradients are used to achieve high spatial resolution. It will in general depend on the nature of $B_z(t)$ and the specific application for which sequence the best performance will be achieved.

5.8 Conclusions

in this work we have reported a detailed investigation of spin-based magnetometry with multi-pulse schemes. Our results show significantly enhanced performance both for ac fields with known and with unknown phase. These results pave the way towards unprecedented magnetic field sensitivity beyond the limit set by the spin-echo sequence. Note that the multi-pulse sequences also make the magnetometer insensitive to instabilities in the setup, such as drifts in the applied static magnetic field or in temperature [25]. The insights gained here will help guide experimenters in tailoring the pulse sequence and number of control pulses to their specific application.

We gratefully acknowledge support from FOM, NWO, the EU SOLID and the DARPA QuEST program. Work at Ames Laboratory was supported by the Department of Energy — Basic Energy Sciences under Contract No. DE-AC02-07CH11358.

Bibliography

[1] R. Jaklevic, J. Lambe, A. Silver and J. Mercereau. Quantum interference effects in josephson tunneling. *Physical Review Letters* **12**, 159 (1964).

[2] A. Chang *et al.* Scanning hall probe microscopy. *Applied Physics Letters* **61**, 1974 (1992).

[3] D. Rugar, C. Yannoni and J. Sidles. Mechanical detection of magnetic resonance. *Nature* **360**, 563 (1992).

[4] I. Kominis, T. Kornack, J. Allred and M. Romalis. A subfemtotesla multichannel atomic magnetometer. *Nature* **422**, 596 (2003).

[5] B. Chernobrod and G. Berman. Spin microscope based on optically detected magnetic resonance. *Journal of Applied Physics* **97**, 014903 (2005).

[6] C. Degen. Scanning magnetic field microscope with a diamond single-spin sensor. *Applied Physics Letters* **92**, 243111 (2008).

[7] J. Taylor *et al.* High-sensitivity diamond magnetometer with nanoscale resolution. *Nature Physics* **4**, 810 (2008).

[8] V. Dobrovitski, G. De Lange, D. Ristè and R. Hanson. Bootstrap tomography of the pulses for quantum control. *Physical Review Letters* **105**, 077601 (2010).

[9] J. Maze *et al.* Nanoscale magnetic sensing with an individual electronic spin in diamond. *Nature* **455**, 644 (2008).

[10] G. Balasubramanian *et al.* Nanoscale imaging magnetometry with diamond spins under ambient conditions. *Nature* **455**, 648 (2008).

[11] G. Balasubramanian *et al.* Ultralong spin coherence time in isotopically engineered diamond. *Nature Materials* **8**, 383 (2009).

[12] B. Maertz, A. Wijnheijmer, G. Fuchs, M. Nowakowski and D. Awschalom. Vector magnetic field microscopy using nitrogen vacancy centers in diamond. *Applied Physics Letters* **96**, 092504 (2010).

[13] S. Steinert *et al.* High sensitivity magnetic imaging using an array of spins in diamond. *Review of Scientific Instruments* **81**, 043705 (2010).

[14] J. Wrachtrup and F. Jelezko. Processing quantum information in diamond. *Journal of Physics Condensed Matter* **18**, S807 (2006).

[15] B. Naydenov. Dynamical decoupling of a single-electron spin at room temperature. *Phys. Rev. B* **83**, 081201 (2011).

[16] G. Fuchs, V. Dobrovitski, D. Toyli, F. Heremans and D. Awschalom. Gigahertz dynamics of a strongly driven single quantum spin. *Science* **326**, 1520 (2009).

[17] H. Carr and E. Purcell. Effects of diffusion on free precession in nuclear magnetic resonance experiments. *Physical Review* **94**, 630 (1954).

[18] C. Ryan, J. Hodges and D. Cory. Robust decoupling techniques to extend quantum coherence in diamond. *Physical Review Letters* **105**, 200402 (2010).

[19] T. Gullion, D. Baker and M. Conradi. New, compensated carr-purcell sequences. *Journal of Magnetic Resonance (1969)* **89**, 479 (1990).

[20] R. Hanson and D. Awschalom. Coherent manipulation of single spins in semiconductors. *Nature* **453**, 1043 (2008).

[21] C. Meriles *et al.* Imaging mesoscopic nuclear spin noise with a diamond magnetometer. *Journal of Chemical Physics* **133**, 124105 (2010).

[22] G. Bauer. *Appl. Opt.* **7**, 1017 (1968).

[23] G. Uhrig. Keeping a quantum bit alive by optimized ÏĂ-pulse sequences. *Physical Review Letters* **98**, 100504 (2007).

[24] L. Hall, C. Hill, J. Cole and L. Hollenberg. Ultrasensitive diamond magnetometry using optimal dynamic decoupling. *Physical Review B - Condensed Matter and Materials Physics* **82**, 045208 (2010).

[25] V. Acosta *et al.* Temperature dependence of the nitrogen-vacancy magnetic resonance in diamond. *Physical Review Letters* **104**, 070801 (2010).

Chapter 6

Controlling the quantum dynamics of a mesoscopic spin bath in diamond

G. de Lange, T. van der Sar, M.S. Blok, Z. H. Wang, V.V. Dobrovitski, and R. Hanson

Understanding and mitigating decoherence is a key challenge for quantum science and technology. The main source of decoherence for solid-state spin systems is the uncontrolled spin bath environment. Here, we demonstrate quantum control of a mesoscopic electron spin bath in diamond at room temperature. The resulting spin bath dynamics are probed using a single nitrogen-vacancy (NV) center electron spin as a magnetic field sensor. We exploit the spin bath control to dynamically suppress dephasing of the NV spin by the spin bath. Furthermore, by combining spin bath control with dynamical decoupling, we directly measure the coherence and temporal correlations of different groups of bath spins. These results uncover a new arena for fundamental studies on decoherence and enable novel avenues for spin-based magnetometry and quantum information processing.

This chapter has been submitted for publication. See also http://arxiv.org/abs/1104.4648

6.1 Introduction

In the past few years, new advances in quantum science and technology have underscored the importance of understanding and controlling decoherence of single solid-state spins [1–3]. Decoherence of a single central spin in contact with a spin bath environment has been intensively studied in various systems such as quantum dots [4–7], donors in silicon [8] and defects in diamond [9–12] through control and readout of the central spin. Here, we implement quantum control of both the central spin and its spin bath environment, thereby enabling a range of new experiments on fundamentals of decoherence. Moreover, spin bath control is a crucial ingredient of recent proposals for environment-assisted magnetometry [13], room-temperature quantum computing using spins in diamond [14, 15] and spin squeezing [16].

Our study focuses on the electronic spin bath environment formed by nitrogen impurities surrounding a single NV center in diamond (Fig. 6.1a). The electron spin of the NV center can be initialized and read out optically, and coherently controlled with high fidelity at room temperature using microwave magnetic pulses [17–19]. For controlling the quantum state of the bath spins, we apply short (tens-of-nanoseconds) radiofrequency (RF) pulses to the sample. The control fields for both the central NV spin and the bath spins are delivered through a broadband coplanar waveguide (CPW) fabricated on the diamond substrate.

6.2 A single NV center as a sensor to probe the spin bath dynamics

The state of the (optically inactive) spin bath can in principle be monitored directly via the emitted RF radiation as in conventional electron spin resonance. However, this method requires many orders of magnitude more spins than contained in our mesoscopic region of interest, and is limited to high magnetic fields. Instead, we exploit the coupling of the bath spins to the single NV center. The near-atomic size of the NV center, combined with the strong ($\sim 1/r^3$) distance dependence of the dipolar coupling to the surrounding bath spins, renders the NV spin mainly sensitive to a small number N (a few tens) of bath spins. This local spin bath exhibits a large statistical polarization ($\sim 1/\sqrt{N}$) that is felt by the NV center as a magnetic dipolar field δb. The spin bath polarization and the corresponding value of the bath field δb change in time due to flip-flop processes within the bath, leading to dephasing of the NV center spin on a timescale $T^*_{2,\mathrm{NV}}$ of about 300 ns [19]. This quasi-static dephasing is compensated in a spin echo sequence with a refocusing π-pulse (Fig. 6.1b), yielding decay on a much longer

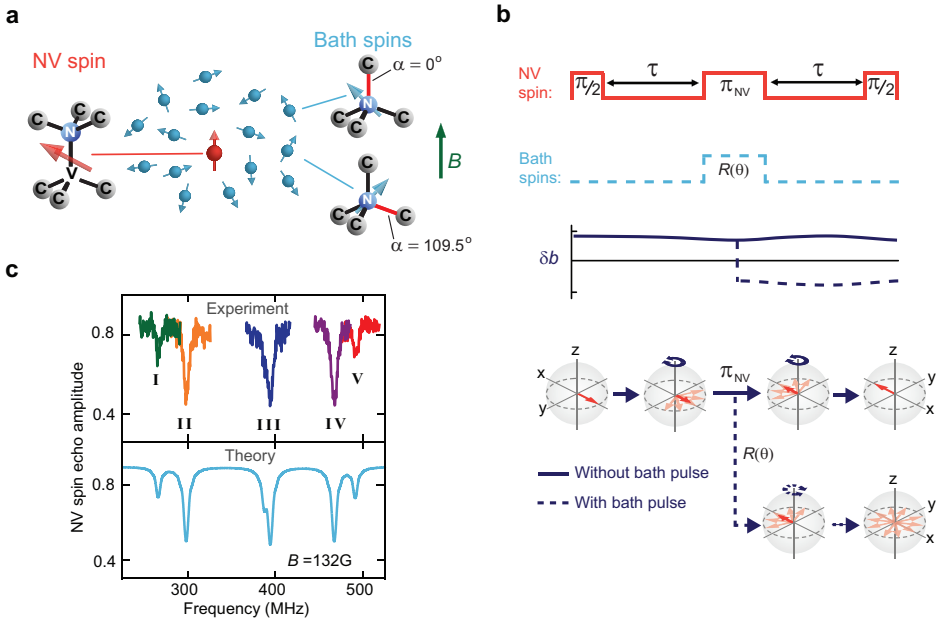

Figure 6.1: Magnetic resonance spectroscopy of a spin bath using a single spin sensor. a. Schematic of the system: a single NV center electronic spin ($S = 1$) is surrounded by a bath of electron spins ($S = 1/2$) belonging to substitutional N impurities. The applied external magnetic field B is aligned with the symmetry axis of the NV center, which is oriented along the [111] crystallographic direction. Nitrogen impurities exhibit a static Jahn-Teller distortion, which results in an elongation of one of the four N-C bonds. As a result, the defect has a symmetry axis, also called the Jahn-Teller axis (indicated red), which is oriented along randomly along one of the crystallographic axes. Two geometric types of bath spins exist, distinguished by the orientation of their Jahn-Teller axis w.r.t. to the external field B: those with their JT axis at an angle $\alpha = 0^o$, and those with $\alpha = 109.5^o$. **b**, Measurement sequence for spin bath spectroscopy. A spin echo sequence is applied to the NV spin using MW pulses; bath spins are controlled by RF pulses. The evolution of the NV spin during the sequence is sketched in the Bloch spheres at the bottom, both for the case of no spin bath control (solid line), and for the case of a pulse applied to bath spins (dashed line). **c**, Upper panel: Magnetic resonance spectroscopy of the spin bath. A magnetic field $B = 132$ G is applied along the NV center symmetry axis. Roman numbers label the different groups of N electron bath spins, according to their nuclear spin projections m_I and angle α between their Jahn-Teller axis and the external magnetic field: I,V: $m_I = \pm 1$ and $\alpha = 0°$, II,IV: $m_I = \pm 1$ and $\alpha = 109.5°$, III: $m_I = 0$ and $\alpha = 0°$ or $109.5°$. Lower panel: Calculation of the spectrum (See section 6.7).

timescale $T_{2,\mathrm{NV}} = 2.6(1)\ \mu$s [19]. However, if we induce changes in the state of the bath spins (thus changing the value of δb) by applying an RF pulse halfway the NV spin echo sequence, the refocusing is ineffective and the NV spin echo amplitude is reduced (Fig. 6.1b). Therefore, by incorporating the spin bath control within a spin echo sequence of the NV center the resulting spin bath dynamics can be probed.

6.3 Magnetic resonance spectroscopy of bath spins

To identify the environmental spins we perform magnetic resonance spectroscopy by sweeping the frequency of applied RF pulses while monitoring the NV spin echo amplitude (upper panel of Fig. 6.1c). Several sharp dips are observed, demonstrating that spins in the environment are being rotated at these specific frequencies. The obtained spectrum matches that of single electron spins ($S = 1/2$) belonging to substitutional Nitrogen (N) impurities [20]. We find excellent agreement with a theoretical spectrum calculated using known values for the Zeeman energy and the anisotropic hyperfine interaction with the N nuclear spin (lower panel of Fig. 6.1c). Since the resonance frequencies are spaced by several line widths, only spins that belong to the same spectral group can exchange energy via flip-flop processes. The spin environment of the NV center can therefore be decomposed into different spectral groups of electron spins (labelled I to V) that are distinguished by their hyperfine interaction with the host N nuclear spin.

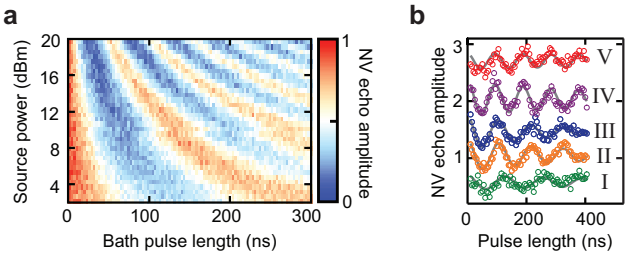

Figure 6.2: Coherent control of the spin bath. a. Coherent driven oscillations of group II bath spins, using RF pulses of 298 MHz. Revivals in NV echo amplitude are observed whenever the bath spins from group II perform a 2π rotation. The maximum Rabi frequency extracted from fitting the upper trace at 20 dBm source power is $f_1 = 20.5(1)$ MHz. **b.** Independent coherent control of all groups of bath spins. Solid lines are fits to $\propto e^{-t/T_D}\cos(2\pi f_1 t)$ with t the length of the RF pulse.

With the resonance frequencies known, we can coherently control the spin environment. Fig. 6.2a shows the effect of short RF pulses at the resonance

frequency of group II spins. Periodic revivals in the NV spin echo amplitude are observed as a function of RF pulse length, with a frequency that increases with RF pulse amplitude. This behaviour is the key signature of coherently driven ("Rabi") oscillations, demonstrating that we have achieved quantum control of the spin environment. We note that the NV spin echo revives almost completely whenever the bath spins are rotated by a multiple of 2π, indicating that the environment has returned to the state it had before the RF pulse. We can control all other spin bath groups in a similar manner (Fig. 6.2b). In addition, our setup allows us to rotate several or all of the groups simultaneously.

6.4 Spin echo double resonance (SEDOR)

The ability to control both the NV center spin and its spin bath environment opens up a range of new possible experiments aimed at studying and manipulating the coupling between a central spin and a spin bath as well as investigating the internal bath dynamics. We first apply the bath control to measure the coupling of each of the bath spin groups to the NV center spin using a spin echo double resonance (SEDOR) scheme [21] (Fig. 6.3a).

With this scheme the dephasing of the central spin induced by one particular group of bath spins can be probed, while the effect of all other dephasing channels (including other spin bath groups) is refocused. We find that, whereas the NV spin echo amplitude decays as $\propto \exp(-(2\tau/T_{2,\mathrm{NV}})^3)$, the SEDOR scheme yields a faster, Gaussian-shaped decay (see Fig. 6.3a). The Gaussian shape indicates that the decay observed with SEDOR is dominated by the quasi-static static dephasing channel that we have selectively turned on. Therefore, the SEDOR decay time $T_{\mathrm{SEDOR},i}$ directly yields the r.m.s. interaction strength b_i between the NV spin and the i^{th} spin bath group via $1/T_{\mathrm{SEDOR},i} = b_i/\sqrt{2}$. We find $b_I = 0.83(2)\ \mu\mathrm{s}^{-1}$, $b_{II} = 1.59(3)\ \mu\mathrm{s}^{-1}$, $b_{III} = 1.58(4)\ \mu\mathrm{s}^{-1}$, $b_{IV} = 1.63(4)\ \mu\mathrm{s}^{-1}$ and $b_V = 0.80(2)\ \mu\mathrm{s}^{-1}$ (see Fig. 6.5 for the SEDOR data of groups III, IV, and V). These values are close to the ratio of $b_I : b_{II} : b_{III} : b_{IV} : b_V = 1 : \sqrt{3} : 2 : \sqrt{3} : 1$ expected from the abundance of each spectral group [20], except for the slightly lower value for group III. This group is actually composed of two subgroups which spectrally do not coincide perfectly. The control fidelity is therefore lower for this group which results in a lower measured coupling in the SEDOR experiment.

The r.m.s. field fluctuations generated by the full electron spin bath are given by $b_{\text{spin-bath}} = \sqrt{\sum_i b_i^2} = 3.01(4)\ \mu\mathrm{s}^{-1}$. This value falls short of the measured total dephasing rate of $b_{\mathrm{total}} = 3.6(1)\ \mu\mathrm{s}^{-1}$ (Fig. 6.6a), suggesting the presence of additional dephasing channels, such as the carbon-13 nuclear spins [9, 10] and magnetic field drifts, with a strength of $b_{\mathrm{excess}} = \sqrt{b_{\mathrm{total}}^2 - b_{\text{spin-bath}}^2} = 1.97(4)\ \mu\mathrm{s}^{-1}$. This interpretation is supported by independent measurements on an NV

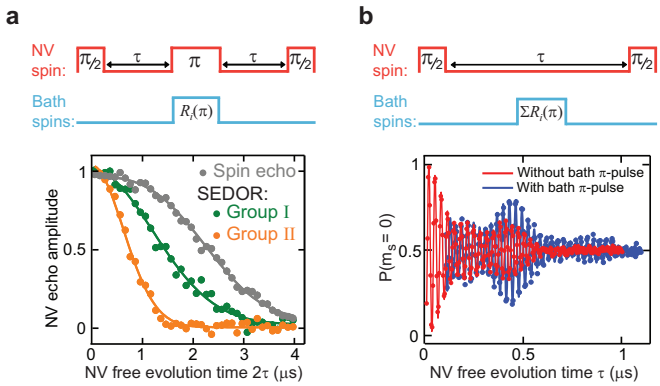

Figure 6.3: Control of NV spin coherence by spin bath manipulation. a. Spin echo double resonance (SEDOR) experiment. The RF pulses have been calibrated to rotate a preselected group of bath spins over a π angle. The NV spin echo curve is fit to $\propto \exp(-(2\tau/T_{2,\mathrm{NV}})^3)$, SEDOR curves are fit to $\propto \exp(-(2\tau/T_{\mathrm{SEDOR},i})^2)$. **b.** Dynamical suppression of NV center spin dephasing through spin bath control. Free evolution of the NV spin is shown with (blue) and without (red) RF π-pulse applied to the bath spins. Solid lines are fits that include the detuning ($\Delta f = 30$ MHz) of the MW driving field compared to the NV spin splitting, and local hyperfine interaction of 2.2 MHz with the host nuclear N spin. The overall signal decays with a Gaussian envelope, with decay constant $T^*_{2,\mathrm{NV}} = 278(5)$ ns ($b_{\mathrm{total}} = 3.60(6)\ \mu\mathrm{s}^{-1}$) in the absence of the spin bath control (red) and with decay constant $T^*_{2,\mathrm{NV}} = 450(9)$ ns ($b_{\mathrm{excess}} = 2.11(7)\ \mu\mathrm{s}^{-1}$) in the case where the bath control pulses are applied (blue).

center in a pure diamond sample with low nitrogen content under the same experimental conditions that yield $b_{\mathrm{excess}} = 2.06(4)\ \mu\mathrm{s}^{-1}$ (Fig. 6.6b).

For applications in quantum information processing [1] and spin-based dc-magnetometry [2,3], suppressing dephasing is crucial. We now demonstrate that quantum control of the spin bath can be used to eliminate the effect of the spin bath on the free evolution dynamics of the NV center spin (see Fig. 6.3b). By flipping all bath spins, the interaction between the NV center and bath spins can be time-averaged to zero. This procedure is akin to dynamical decoupling as recently demonstrated on single NV center spins [19,22,23], but has the advantage that no control pulses on the NV center itself are required. We find that a refocusing π-pulse applied simultaneously to all bath spins (Fig. 6.3b)) increases $T^*_{2,\mathrm{NV}}$ up to the limit set by b_{excess}, indicating that dephasing by the electron spin bath is suppressed. Similar enhancement is achieved by continuous driving of all bath spins (6.6a).

6.5 Coherence and temporal correlations of bath spins

By combining the spin bath control with the ability to freeze the evolution of the NV spin by dynamical decoupling [19,22,23], coherence and temporal correlations during free evolution within the spin bath can be directly probed. We replace the single refocusing pulse of the spin echo sequence on the NV spin by a dynamical decoupling (DD) sequence with a net π-rotation. The DD sequence provides a means to temporarily turn off our sensor (the NV center) as it is made insensitive to the magnetic environment for the duration of the DD sequence; the net π-rotation ensures that the refocusing action of the sequence is preserved. The two periods of free evolution τ_s of the NV spin now serve as sensing stages which each sample the dipolar field generated by the bath spins. The NV echo amplitude is therefore a measure of the correlation between the dipolar fields measured during the two sensing stages. While the sensor is switched off, we can apply multi-pulse RF sequences to individual spectral groups of bath spins to study their coherence during free evolution.

An RF Ramsey sequence (Fig. 6.4a) and Hahn-echo sequence (Fig. 6.4b) is applied to spectral group i to measure its spin dephasing time $T^*_{2,i}$ and coherence time $T_{2,i}$ respectively. Data is shown for spectral groups I and II.

The values we find for $T^*_{2,i}$ are similar for the two groups as expected, since all bath spins suffer from the same dephasing channels formed by spins from all groups. From the value of $T^*_{2,i}$ we estimate the local density of bath spins to be $n = \frac{6\sqrt{3}}{\pi^2 T_2^*} \frac{\hbar}{\mu_0 g^2 \mu_B^2} = 100$ parts per million [24, 25].

The bath spin-echo sequence yields different decay times, $T_{2,\mathrm{I}} = 1.9(6)\ \mu\mathrm{s}^{-1}$ and $T_{2,\mathrm{II}} = 0.89(13)\ \mu\mathrm{s}^{-1}$, for spectral groups I and II. The difference in coherence times between different spectral groups may arise due to dephasing caused spins within the same group, in a process which is known as instantaneous diffusion [26, 27]. The RF π-pulse does not refocus the dipolar interactions between spins of the same spectral group since these spins are themselves rotated by the RF π-pulse. The resulting intra-group dephasing is much stronger in group II because it contains three times more spins than group I.

To characterize the temporal correlations resulting from the dynamics in the environment we perform a direct measurement of the auto-correlation function and its $1/e$ decay time τ_C. The field generated by the complete magnetic environment is sampled during two sensing stages separated by a variable waiting time during which we turn off the NV center sensor (Fig. 6.4c) and let the spin bath evolve freely [28]. As the sensor off-time is increased, the initial correlation between the two fields is gradually lost resulting in decreasing NV echo amplitude. We observe a decay of the auto-correlation function on a timescale of about

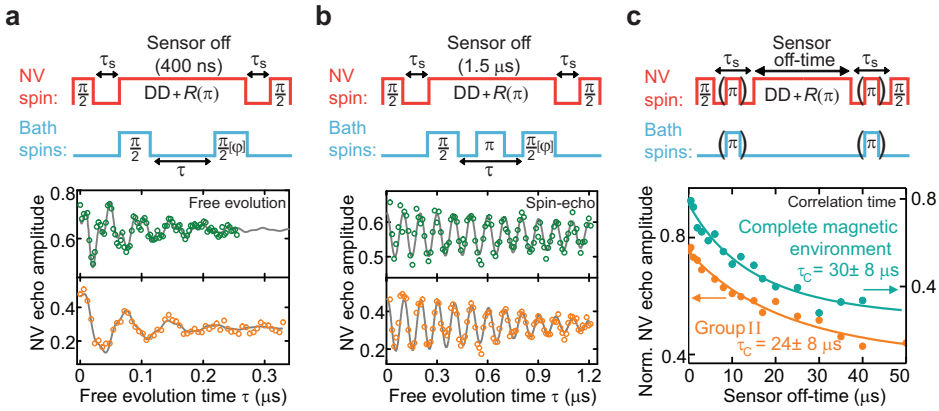

Figure 6.4: Coherent dynamics and temporal correlations of the spin bath. **a.** Measurement of decay during free evolution of spin bath groups I and II. The two sensing stages marked by τ_s serve to sample the magnetic environment before and after the Ramsey sequence is applied to the bath spins. The NV spin sensor is turned off while the RF Ramsey sequence is applied to the bath spins (see main text for details). Instead of detuning the RF pulse field with respect to the transition to observe fringes, an artificial detuning f_a is introduced by changing the phase of the final RF $\pi/2$-pulse linearly with pulse separation $\phi = 2\pi f_a \tau$. The fast modulation of Ramsey fringes for group I (upper panel) result from off-resonant driving of the more abundant spins from group II. Solid lines are fits to $\propto y_0 + \sum_{i=\mathrm{I,II}} A_i e^{-\tau/T^*_{2,i}} \cos(2\pi f_a \tau + \phi_i)$. From the fits we extract the decay constants $T^*_{2,\mathrm{I}} = 97(11)$ ns and $T^*_{2,\mathrm{II}} = 91(7)$ ns. **b.** Spin echo on spin bath groups I and II. The phase of the final RF $\pi/2$-pulse is changed as a function of total free evolution time τ as $\phi = 2\pi f_a \tau$ with $f_a = 10$ MHz, resulting in oscillations in the NV spin echo amplitude with free evolution time τ. Solid lines are fits to $\propto e^{-\tau/T_{2,i}} \cos(2\pi f_a \tau + \phi_i)$ from which the decay times $T_{2,\mathrm{I}} = 1.9(6)$ μs and $T_{2,\mathrm{II}} = 0.89(13)$ μs are extracted. **c.** Measurement of temporal correlations on the full environment and on spin bath group II alone. During the sensing stages marked by τ_S, MW and RF π-pulses can be applied simultaneously to the NV spin and to the bath spins to selectively measure the correlation time of a particular group of bath spins. Solid lines are fits to $\propto \exp(-b^2 \tau_\mathrm{S}^2 (1 - e^{-t/\tau_C}))$.

20 μs. We can also find the correlation time of an individual spin bath group by inserting a SEDOR sequence in the sensing stage, as demonstrated for group II (Fig. 6.4c). The measured correlation time of group II is comparable to that of the complete magnetic environment, indicating that the coherence time of the NV center is indeed limited by the dynamics of the electron spin bath. The measured correlation time is comparable to the value $\tau_C = b^2_{\text{spin-bath}} T^3_{2,\mathrm{NV}}/12 \approx 13$ μs expected from mean-field theory [19, 26].

6.6 Conclusions

In conclusion we have demonstrated full quantum control of a spin bath surrounding a single NV center. These results pave the way for a new class of experiments on spin bath decoherence, such as manipulating the correlation time of different spin bath groups and generating squeezed spin bath states [16]. Furthermore, the suppression of spin dephasing by spin-bath control may be exploited for protecting coherence in spin-based quantum technologies [1–3, 14, 29, 30]. Finally, quantum control of nitrogen electron spins close to NV centers as demonstrated here enables implementation of quantum registers of individual N electron spins [31, 32], scalable coupling of NV center quantum bits via spin chains [15] and ultra-sensitive environment-assisted magnetometry [13].

6.7 Additional material

Magnetic resonance spectroscopy

Pulses with a length of $t_p = 200$ ns and Rabi frequency of $f_1 \approx 2.5$ MHz were used on the RF channel to achieve lower Rabi frequency than the expected linewidth. These experimental parameters reflect the trade-off in achieving equilibrium at the end of the RF pulse, a long free evolution period for the NV spin to get high signal and the limited spin echo decay time of the NV spin.

The theory curve of the magnetic resonance spectroscopy in Fig. 6.1 is calculated by assuming a Lorentzian distribution $L(f_{RF})$ with transition frequencies given by the bath Hamiltonian eq. (1): $E = \{266, 298, 387, 394, 467, 491\}$ MHz with relative abundances [20].

$$D = \{1/12, 3/12, 1/12, 3/12, 3/12, 1/12\}\,.$$

All transitions are assumed to suffer from the same inhomogeneous broadening by ≈ 4 MHz as was measured in Fig. 6.4a. Since the Rabi frequency is of the same order as the line-width, each point in the theory curve is determined by

$$S_{NV}\left(f_{RF}\right) = W \exp\left[-b^2\tau^2 \int R(f_{RF}, f_0)L(f_0)df_0\right] \tag{6.1}$$

with f_{RF} the RF driving frequency, the sensing time $\tau = 600ns$ which is given by the delay between the $\pi/2$ and π-pulse on the NV spin, $b \approx 3$ μs is the total interaction strength between NV and its spin environment. The factor W is there to take into acount the decay due to the limited coherence time T_2 of the NV spin and is given by $W = \exp\left[-\left(2\tau/T_2\right)^3\right]$. With the given τ and $T_2 = 2.6$ μs,

$W \approx 0.9$. The factor $R(f_{RF})$ is the probability that a bath spin with resonance frequency f_0 is found to be flipped after the 200 ns RF pulse and is given by

$$R(f_{RF}, f_0) = \frac{f_1^2}{f_1^2 + (f_0 - f_{RF})^2} \sin^2\left(\pi\sqrt{f_1^2 + (f_0 - f_{RF})^2}t_p\right) \tag{6.2}$$

Coherent driven oscillations of bath spins

Curves are fit to $\propto e^{-t/T_d}\cos 2\pi f_{1,i}t_p$ to extract the Rabi frequency $f_{1,i}$ for group i. As the length increases the effective sensing time decreases due to the decoupling of bath spins from the NV spin while bath spins are driven (see Fig. 6.3b). Improved fitting can in principle be achieved when these effects are taken into acount but was not done for these measurements.

SEDOR and decoupling by continous driving

Pulses are calibrated by performing coherent oscillations of the bath spins at various powers. Especially for group I and V the off-resonant driving of nearby groups (II and IV respectively) prevents a proper calibration at high powers. For this reason lower power is used for the outer two transitions (group I and V). Fig. 6.5 shows the SEDOR curves for groups III to V.

The NV spin echo decay in a SEDOR experiment on group i, which is induced by the other groups, will modulate the SEDOR decay shape. However, these modulations can be ignored as its contribution becomes comparable when $\tau > b_i^2 T_2^3/4$. Since $b_i >> 1/T_2$, the modulation only influences the tail of the SEDOR curves and does not compromise the reliability of the fits.

The π-pulses used in the pulsed RF dynamical decoupling measurements from Fig.6.3b are calibrated by driving all groups simultaneously with the same amplitude while varying the pulse length resulting in a 83 ns multifrequency π-pulse. We also dynamically decoupled the NV spin from the spin bath by continuously driving all bath spins with a long multifrequency RF pulse with a length equal to the free evolution time of the NV spin. The result is in Fig. 6.6a. Each tone in the multifrequency RF pulse drives a single group with a Rabi frequency of 6 MHz.

Ramsey and spin echo decay of the nitrogen spin bath

To explain the origin of the signal of Figs. 6.4a. and b. we analyse a single measurement cycle. At the beginning of the measurement cycle the spin bath is in some randomly polarized state such that it induces a dipolar field $\delta b_{z,1}$ along the quantization axis of the NV center. Taking the sequence from Fig. 4a a MW $\pi/2$-pulse on the NV spin creates a superposition of the $m_s = 0$ and $m_s = -1$

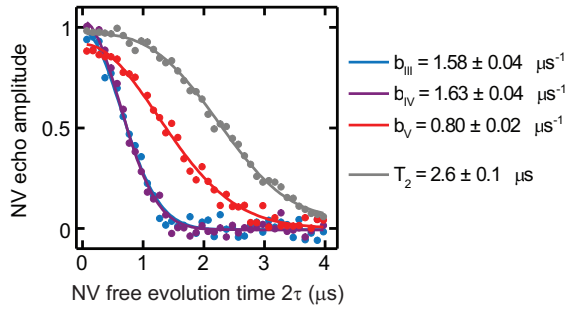

Figure 6.5: SEDOR curves of groups III to V. Gray is the NV spin echo curve which decays $\propto e^{-(2\tau/T_2)^3}$, observed for the case that no RF pulses are applied to the bath spins. The colored curves are SEDOR data obtained as described in the main text. They exhibit faster Gaussian decay $\propto e^{-2\tau^2 b_i^2}$. The parameters b_i quantify the coupling between NV spin and bath group i.

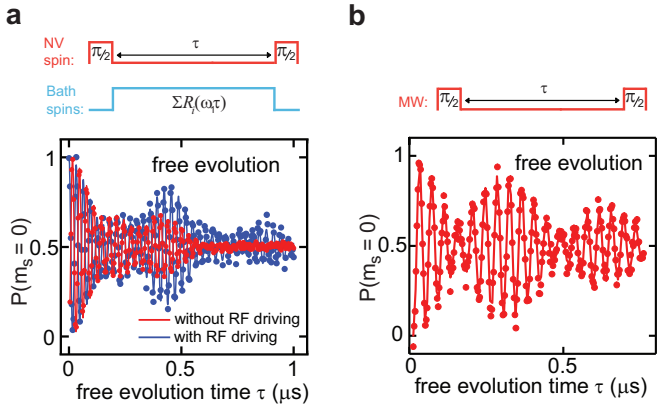

Figure 6.6: (**a**) Decoupling of the NV spin by continuous driving of the spin bath. Fitting the data with RF pulse (blue) to Gaussian decay gives $b_{\text{excess}} = (2.02 \pm 0.05)$ μs^{-1}. (**b**) Ramsey fringes for an NV center with a ^{15}N atom in low nitrogen content IIa diamond. The beating frequency is 3 MHz, because the hyperfine interaction of the NV electron spin with a ^{15}N nuclear spin has different strength compared to ^{14}N. We find a value of $b = (2.06 \pm 0.06)$ μs^{-1} for this NV center, in very good agreement with b_{excess}.

NV spin states, which freely precesses during a time τ_s. During this period of free precession the NV spin will accumulate a phase $g\mu_B \delta b_{z,1} \tau_s$. The NV spin state is then frozen for a fixed time and flipped by the sequence $DD - X - DD$,

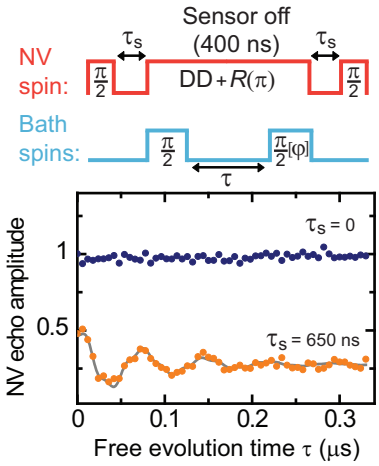

Figure 6.7: Same data as the upper panel of Fig 4a is shown (orange). The DD sequence used is the XY4 sequence with $\tau_1 = 32$ ns. The total sensor off time is 400ns and is kept constant for all data points. As a control measurement we perform the same measurement with the exact same MW and RF sequences to NV and bath spins respectively but now we set the sensing time $\tau_s = 0$ (blue). For the control measurement the full unperturbed NV echo amplitude is retrieved, verifying that indeed the NV sensor is switched off during the DD sequence.

with DD the dynamical decoupling sequence.

During the $DD - X - DD$ sequence on the NV sensor, an RF pulse sequence is applied to the bath spins (a Ramsey and spin echo sequence in Figs 4a and 4b respectively). This sequence is applied symmetrically with respect to the central X-pulse. The interpulse delays in the DD sequence are kept short ($\tau_1 = 30-50ns$ compared to T_2^* in order to limit the perturbation of the NV spin during the sensor-off time. That the sensor is indeed switched off is verified in Supplementary figure S3. Note that the motion of the NV spin does not noticeably influence the intra-bath dynamics, since the evolution of each bath spin is determined primarily by the couplings to a large number of other bath spins, which completely overshadow the impact of a single NV spin.

After the RF sequence and the DD sequence end the bath is in a new state and generates a dipolar field $\delta b_{z,2}$. The NV spin will continue to precess again under the influence $\delta b_{z,2}$ for a time τ_s. Due to the net π rotation the total phase accumulated before and after the Ramsey sequence is then $\Delta\phi = g\mu_B(\delta b_{z,1} - \delta b_{z,2})\tau_s$. A final MW $\pi/2$-pulse on the NV spin and subsequent optical read-out will then measure the echo of the NV spin $\propto \cos(\Delta\phi)$. The NV spin echo amplitude will therefore depend on the correlation between $\delta b_{z,1}$ and $\delta b_{z,2}$ giving maximum

amplitude for a full correlation and minimum amplitude for anti-correlation.

Extracting the correlation time of the spin bath.

We consider first the protocol for measuring the correlation time of the environment as a whole. The protocol is very similar to that for measuring stimulated echoes [21] and works as follows. We start with a $\pi/2$ pulse on the NV center, which is assumed to be perfect. Then, there is a free evolution for the time τ_s, after which the XY4 DD sequence on the NV center is applied for time T (referred to as the "sensor off-time" in Fig. 4c). As in the previous measurements, the evolution of the NV spin during the DD period corresponds to a full π rotation. During the sensor off-time T, the bath freely evolves and flip-flip processes within the bath will change the statistical polarization of spins surrounding the NV spin. After time T the DD sequence ends and another period of free evolution of the NV spin of duration τ_s follows. Finally, another ideal $\pi/2$ pulse is applied to NV center, and its state is read out.

The measured signal is proportional to

$$F = \mathrm{Tr}\left[\exp\left(i\hat{B}\tau_s\hat{S}_z^{NV}\right)\hat{Z}\exp\left(-i\hat{B}\tau_s\hat{S}_z^{NV}\right)\hat{Z}^\dagger\right]. \tag{6.3}$$

the operator $\hat{Z}$ is simply

$$\hat{Z} = \exp\left[-iT\hat{H}_B\right]. \tag{6.4}$$

Therefore, the unnormalized signal, the quantity F, can be written as

$$F = \mathrm{Tr}\left[\exp\left(i\hat{B}\tau_s\hat{S}_z^{NV}\right)\exp\left(-i\hat{B}(T)\tau_s\hat{S}_z^{NV}\right)\right]. \tag{6.5}$$

where $\hat{B}(T) = \exp\left[iT\hat{H}_B\right]\hat{B}\exp\left[-iT\hat{H}_B\right]$. Within the mean-field approximation, we replace the operator $\hat{B}$ by the effective dipolar field $B(t)$, which is a random Ornstein-Uhlenbeck (OU) process with rms b and the correlation time $\tau_C = 1/R$. In case of $\tau_s \ll \tau_C$, we can take the field $B(t)$ as static during both intervals τ_s. Correspondingly, taking into account normalization, the measured signal is

$$S_{NV} = \left\langle \exp\left(iB(t)\tau_s\right)\exp\left(-iB(t+T)\tau_s\right)\right\rangle, \tag{6.6}$$

where the angular brackets denote the average over the OU process. To calculate the average, we take into account that for a Gaussian random process $B(t)$, the characteristic functional can be calculated explicitly [33]

$$\Phi[\xi(t)] = \left\langle \exp\left(i\int_0^T B(t)\xi(t)dt\right)\right\rangle = \exp\left(-(1/2)\int_0^T dt\int_0^T ds\ \phi(t,s)\xi(t)\xi(s)\right)$$

(6.7)

where, in our case, $\xi(t) = \tau_s[\delta(t) - \delta(t-T)]$, and the correlation function $\phi(t,s) = b^2 \exp(-R|t-s|)$. The result is

$$S_{NV} \propto \exp\left[-b^2\tau_s^2\left(1 - \mathrm{e}^{-RT}\right)\right]. \tag{6.8}$$

Acknowledgements

We sincerely thank D. D. Awschalom, S. Frolov, G. D. Fuchs, K. Nowack, D. Risté and L. M. K. Vandersypen for useful discussions. We gratefully acknowledge support from the Defense Advanced Research Projects Agency, the Dutch Organization for Fundamental Research on Matter (FOM), the Netherlands Organization for Scientific Research (NWO), and the European Union SOLID programme. Work at Ames Laboratory was supported by the Department of Energy-Basic Energy Sciences under Contract No. DE-AC02-07CH11358.

Bibliography

[1] T. D. Ladd *et al.* Quantum computers. *Nature* **464**, 45 (2010).

[2] C. L. Degen. Scanning magnetic field microscope with a diamond single-spin sensor. *Applied Physics Letters* **92**, 243111 (2008).

[3] J. M. Taylor *et al.* High-sensitivity diamond magnetometer with nanoscale resolution. *Nature Physics* **4**, 810 (2008).

[4] H. Bluhm *et al.* Dephasing time of gaas electron-spin qubits coupled to a nuclear bath exceeding 200 μs. *Nature Physics* **7**, 109 (2011).

[5] H. O. H. Churchill *et al.* Electron - nuclear interaction in 13C nanotube double quantum dots. *Nature Physics* **5**, 321 (2009).

[6] I. T. Vink *et al.* Locking electron spins into magnetic resonance by electron - nuclear feedback. *Nature Physics* **5**, 764 (2009).

[7] C. Latta *et al.* Confluence of resonant laser excitation and bidirectional quantum-dot nuclear-spin polarization. *Nature Physics* **5**, 758 (2009).

[8] A. Morello *et al.* Single-shot readout of an electron spin in silicon. *Nature* **467**, 687 (2010).

[9] L. Childress *et al.* Coherent dynamics of coupled electron and nuclear spin qubits in diamond. *Science* **314**, 281 (2006).

[10] N. Mizuochi *et al.* Coherence of single spins coupled to a nuclear spin bath of varying density. *Physical Review B* **80**, 041201 (2009).

[11] R. Hanson, V. V. Dobrovitski, A. E. Feiguin, O. Gywat and D. D. Awschalom. Coherent dynamics of a single spin interacting with an adjustable spin bath. *Science* **320**, 352 (2008).

[12] G. Balasubramanian *et al.* Ultralong spin coherence time in isotopically engineered diamond. *Nature Materials* **8**, 383 (2009).

[13] G. Goldstein *et al.* Environment-Assisted Precision Measurement. *Physical Review Letters* **106**, 140502 (2011).

[14] N. Y. Yao *et al.* Scalable Architecture for a Room Temperature Solid-State Quantum Information Processor. *Arxiv:1012.2864v1* (2011).

[15] P. Cappellaro, L. Viola and C. Ramanathan. Coherent-state transfer via highly mixed quantum spin chains. *Physical Review A* **83**, 032304 (2011).

[16] M. S. Rudner, L. M. K. Vandersypen, V. Vuletic and L. S. Levitov. Generating Entanglement and Squeezed States of Nuclear Spins in Quantum Dots. *arXiv:1101.3370v2* (2011).

[17] G. D. Fuchs, V. V. Dobrovitski, D. M. Toyli, F. J. Heremans and D. D. Awschalom. Gigahertz dynamics of a strongly driven single quantum spin. *Science* **326**, 1520 (2009).

[18] F. Jelezko and J. Wrachtrup. Single defect centres in diamond: A review. *physica status solidi (a)* **203**, 3207 (2006).

[19] G. de Lange, Z. H. Wang, D. Ristè, V. V. Dobrovitski and R. Hanson. Universal dynamical decoupling of a single solid-state spin from a spin bath. *Science* **330**, 60 (2010).

[20] W. Smith, P. Sorokin, I. Gelles and G. Lasher. Electron-spin resonance of nitrogen donors in diamond. *Physical Review* **115**, 1546 (1959).

[21] C.P. Slichter. *Principles of Magnetic Resonance*. Springer-Verlag, New York (1990).

[22] C. Ryan, J. Hodges and D. Cory. Robust Decoupling Techniques to Extend Quantum Coherence in Diamond. *Physical Review Letters* **105**, 200402 (2010).

[23] B. Naydenov *et al.* Dynamical decoupling of a single-electron spin at room temperature. *Physical Review B* **83**, 081201 (2011).

[24] A. Abragam. *Principles of Nuclear Magnetism*. Clarendon, Oxford (1961).

[25] E. C. Reynhardt, G. L. High and J. A. van Wyk. Temperature dependence of spin-spin and spin-lattice relaxation times of paramagnetic nitrogen defects in diamond. *Journal of Chemical Physics* **109**, 8471 (1998).

[26] J. Klauder. Spectral diffusion decay in spin resonance experiments. *Physical Review* **125**, 912 (1962).

[27] A. Tyryshkin, S. Lyon, A. Astashkin and A. Raitsimring. Electron spin relaxation times of phosphorus donors in silicon. *Physical Review B* **68**, 193207 (2003).

[28] A. Laraoui, J. S. Hodges, C. Ryan and C. A. Meriles. The diamond Nitrogen-Vacancy center as a probe of random fluctuations in a nuclear spin ensemble. *arXiv:1104.2546v1* (2011).

[29] R. Takahashi, K. Kono, S. Tarucha and K. Ono. Voltage-Selective Bidirectional Polarization and Coherent Rotation of Nuclear Spins in Quantum Dots. *arXiv:1012.4545v3* (2011).

[30] M. N. Makhonin *et al.* Fast control of nuclear spin polarization in an optically pumped single quantum dot. *Nature Materials* **10**, 844 (2011).

[31] T. Gaebel *et al.* Room-temperature coherent coupling of single spins in diamond. *Nature Physics* **2**, 408 (2006).

[32] R. Hanson, F. M. Mendoza, R. J. Epstein and D. D. Awschalom. Polarization and readout of coupled single spins in diamond. *Physical Review Letters* **97**, 087601 (2006).

[33] R. Kubo, M. Toda and N. Hashitsume. *Statistical Physics II.* Springer, Berlin, New York (1998).

Chapter 7

Probing the dynamics of an electron-spin ensemble via a superconducting resonator

V. Ranjan, G. de Lange, R. Schutjens, T. Debelhoir, J. P. Groen, D. Szombati, D. J. Thoen, T. M. Klapwijk, R. Hanson, L. DiCarlo

We study spin relaxation and diffusion in an electron-spin ensemble of nitrogen impurities in diamond at low temperature (0.25-1.2 K) and polarizing magnetic field (80-300 mT). Measurements show mode- and temperature- dependent coupling of hyperfine-split sub-ensembles to the resonator. Temperature-independent spin linewidth and relaxation time suggest that spin diffusion limits spin relaxation. Depolarization of one sub-ensemble by resonant pumping of another indicates fast cross-relaxation compared to spin diffusion. This has implications for when sub-ensembles are used as independent quantum memories.

This chapter is still being redacted and may be subject to minor changes.

7.1 Introduction

The study of spin ensembles magnetically coupled to superconducting integrated circuits (SC) is of both fundamental and technological interest. An eventual quantum computer may involve a hybrid architecture [1] combining superconducting qubits [2] for fast processing of information and solid-state spins [3,4] for storage. Pioneering proof-of-principle experiments have demonstrated coherent information transfer between a SC qubit and an ensemble of negatively charged nitrogen-vacancy (NV) centers in diamond [5,6]. Additionally, superconducting resonators allow the study of spin ensembles at low temperatures with ultra-low excitation powers and high spectral resolution [7,8]. While one spin couples very weakly to a single microwave photon (bare magnetic coupling $g \approx 10$ Hz), an ensemble of N spins collectively couples with $g_{\mathrm{ens}} = g\sqrt{N}$ [9,10], reaching the strong-coupling regime $g_{\mathrm{ens}} > \kappa, \gamma$ at $N \gtrsim 10^{12}$ [10–12], where κ and γ are the circuit damping and spin dephasing rates, respectively.

Among the solid-state spin ensembles under consideration, nitrogen defects in diamond (P1 centers) [13] are excellent candidates for quantum information processing. Diamond samples can be synthesized with P1 centers as only paramagnetic impurities, leading to high-purity spin ensembles. Additionally, samples with spin densities ranging from highly dense (> 200 ppm) to very dilute (< 5 ppb) are commercially available, allowing the tailoring of spin linewidth ($\gamma \propto N$ [14]) and collective strength ($g_{\mathrm{ens}} \propto \sqrt{N}$). In contrast to nitrogen-vacancy centers in diamond [3] and rare-earth ions in Y_2SiO_5 [15,16], P1 centers are optically inactive, making a coupled microwave resonator the ideal probe for their study. However, similar to phosphorus in silicon [17], P1 centers lack zero-field splitting. Lifting the constraint of near-zero magnetic field operation, would allow using very pure and highly polarized ensembles of P1 centers at cryogenic temperatures [12] for which decoherence is quenched [18]. Through dynamical decoupling [19] long storage times be achieved with high fidelity, realizing a useful quantum memory.

In this Letter, we investigate the internal dynamics of a P1 electron-spin ensemble probed by controlled resonant and dispersive coupling to the two lowest-frequency modes of a coplanar waveguide (CPW) resonator patterned on NbTiN films [20] withstanding applied fields beyond the needed 300 mT. Three hyperfine-split spin sub-ensembles are clearly resolved in spectroscopy, with mode-dependent collective coupling strengths in accordance with magnetic-field- and temperature-controlled spin polarization. Using a pump-probe technique in the dispersive regime, we measure spin linewidth and relaxation time. The observed temperature independence below 1 K shows that internal spin equilibration is dominated by spin diffusion across the mode volume [21] rather than spin-lattice relaxation [22]. Finally, as an initial test of the possible use of sub-ensembles as

independent quantum memories, we measure the steady-state depolarization of a sub-ensemble by resonant pumping of another. The pump-power dependence observed indicates fast cross-relaxation compared to spin relaxation in the mode volume, calling for follow-up experiments probing the millisecond scale.

7.2 Experimental setup

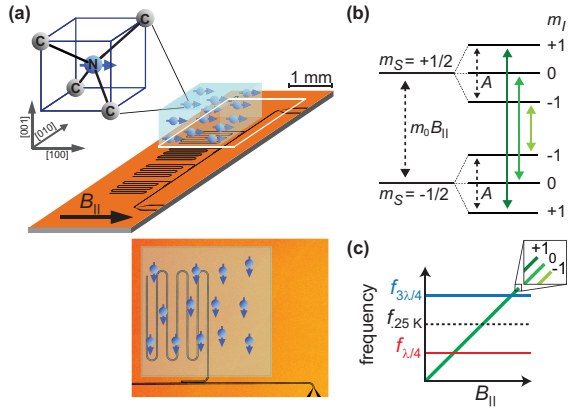

Figure 7.1: (a) Schematic of the hybrid resonator-spin system. A single-crystal diamond piece (1.7 mm × 1.7 mm × 1.1 mm, type Ib Sumicrystal, ∼ 200 ppm N content) is placed on top of one of four CPW resonators capacitively coupled to a common feedline. The resonators are patterned on a NbTiN film (70 nm thick, critical temperature $T_c = 12.5$ K) on sapphire (C-plane, 430 μm thick). An external magnetic field $B_\parallel$ is applied parallel to the film, along the diamond [100] direction. (b) Hyperfine interaction $A \approx 94$ MHz with the N host nuclear spin splits each electron-spin level into a triplet. Only electron-spin transitions that preserve nuclear spin (solid arrows) are allowed. (c) $B_\parallel$ tunes the electron-spin energy levels through resonance with the $\lambda/4$ or $3\lambda/4$ modes of the resonator. The dashed line represents the thermal energy $k_B T/h \approx 5$ GHz at $T = 0.25$ K.

Our hybrid system, shown schematically in Fig. 7.1, consists of four resonators capacitively coupled to a common feedline and a type-Ib diamond sample placed above one of them. The CPW structures are patterned on a film of disordered superconductor (NbTiN [20], critical temperature $T_c = 12.5$ K) withstanding in-plane fields up to 300 mT. The electron-spin ensemble consists of unpaired electrons (spin-1/2) at substitutional nitrogen impurities (∼ 100 ppm density) [Fig. 7.1(a)]. Each electron spin exhibits strong anisotropic hyperfine interaction with the host nucleus (spin-1). The Hamiltonian for one defect is given by $H_N =$

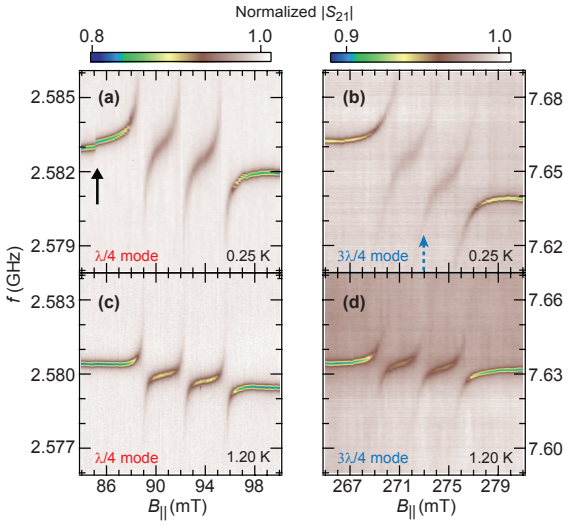

Figure 7.2: Transmission spectroscopy. Image plots of normalized feedline transmission as a function of $B_\parallel$ and frequency near the $\lambda/4$ and $(3\lambda/4)$ mode resonances at $T = 0.25$ K (a,b) and 1.2 K (c,d). Each plot reveals three avoided crossings, corresponding to allowed hyperfine-split electron-spin transitions. Note that the frequency span in (b,d) is 10 times larger than in (a,c). The arrow in (a) points to a flux jump shifting the resonator frequency. All other image plots shown are corrected for these events.

$-m_0\vec{B}\cdot\vec{S} + h\vec{S}\cdot A\cdot\vec{I}$, with $\vec{S}$ and $\vec{I}$ the spin operators for the electron and nitrogen nucleus, respectively, $m_0/h = 28.04$ MHz/mT, h Planck's constant, and $A = \mathrm{diag}(81.33, 81.33, 114.03)$ MHz the hyperfine interaction tensor [23] [third (first, second) index parallel (normal) to the Jahn-Teller axis]. Low-energy terms only involving $\vec{I}$ have been left out. We tune the electron-spin transitions with a magnetic field ($B_\parallel$) applied along the diamond [100] direction. Because all N-C bonds have $\langle 111\rangle$ orientation and make the same angle with $B_\parallel$, the hyperfine interaction is the same for all impurities, creating three hyperfine-split electron-spin transitions [13].

7.3 Magnetic field dependent transmission spectroscopy of the $\lambda/4$ and $3\lambda/4$ resonator modes

Measurements of the feedline transmission $|S_{21}|(f, B_\parallel)$ near the fundamental $(\lambda/4)$ and the second-harmonic $(3\lambda/4)$ modes at $T = 0.25$ K and 1.2 K clearly

show three avoided crossings, as expected for coherent coupling [24] (Fig. 7.2). The coupling strength of each hyperfine transition to the $3\lambda/4$ mode is evidently stronger than to the $\lambda/4$ mode, and decreases for both modes with increasing temperature. The hybridized dips observed when spin sub-ensembles are resonant with the $3\lambda/4$ mode [Fig. 7.3(a)] support strong coupling ($2g_{\mathrm{ens}} > \gamma, \kappa$). The absence of double dips on resonance with the $\lambda/4$ mode indicate $2g_{\mathrm{ens}} < \gamma$.

7.4 Temperature dependence of g_{ens}

We extract g_{ens} by the simple model in Ref. [12], treating the spin sub-ensembles as separate harmonic oscillators coupled to the resonator, but not to each other:

$$S_{21}(\omega) = 1 + \frac{\kappa_{\mathrm{e}}/2}{i\Delta_{\mathrm{c}} - (\kappa_{\mathrm{i}} + \kappa_{\mathrm{e}})/2 + \sum_n \frac{g_{\mathrm{ens}}^2}{i(\Delta_n) - \gamma/2}}. \tag{7.1}$$

Here, $\Delta_{\mathrm{c}} = \omega - f_{\mathrm{c}}$ is the frequency detuning between the probe and bare resonator mode, κ_{i} and κ_{e} are resonator intrinsic and the extrinsic dissipation rates, $\Delta_n = \omega - \omega_{m_I=n}$ is the probe detuning from the $m_I = n$ hyperfine transition and γ is the transition linewidth (assumed independent of m_I). As shown in Figs. 7.3(a) and 7.3(b), fitting the double-dip spectrum for the $3\lambda/4$ mode and the quality factors (Q) for $\lambda/4$ mode at 0.25 K using Eq. (7.1) yields collective coupling strengths $g_{\mathrm{ens}}/2\pi = 17.0 \pm 0.4$ MHz and 3.9 ± 0.2 MHz, respectively (see section 7.8).

To obtain $g_{\mathrm{ens}}(T)$ for each mode, we measure transmission spectra at several temperatures in the range $0.25 - 1.2$ K and perform the same analysis as above. The results for both modes are shown in Fig. 7.3(c) together with the best fits to

$$g_{\mathrm{ens}}(T) = g_{\mathrm{ens}}(0)\sqrt{P(B_{\parallel}, T)}\ , \tag{7.2}$$

where $g_{\mathrm{ens}}(0)$ is the zero-temperature coupling strength, and

$$P(B_{\parallel}, T) = \tanh\big(m_0 B_{\parallel}/2k_{\mathrm{B}}T\big) \tag{7.3}$$

the spin polarization in thermal equilibrium, with k_{B} the Boltzmann constant. Two factors combine to make $g_{\mathrm{ens}}(T)$ higher for the $3\lambda/4$ mode. First, P increases monotonically with the Zeeman energy $m_0 B_{\parallel}$. Second, the bare spin-coupling strength g increases as $\sqrt{f_{\mathrm{c}}}$ owing to a larger vacuum magnetic field strength. The ratio 2.7 between the best-fit $g_{\mathrm{ens}}(0)/2\pi$ values for the $3\lambda/4$ and $\lambda/4$ modes (22.7 ± 0.6 and 8.3 ± 0.2 MHz, respectively) differs from the expected $\sqrt{3}$. This discrepancy may be due to inhomogeneous distribution of P1 centers in the mode volume [25] (see further below).

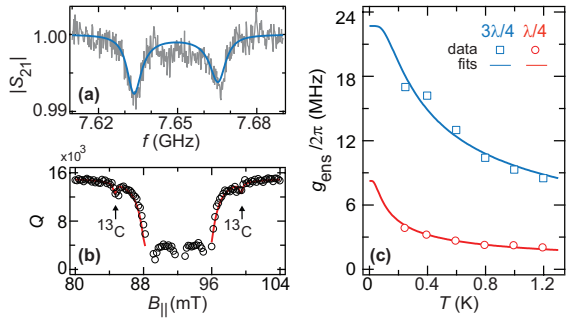

Figure 7.3: Extraction of collective coupling strength. (a) A vertical cut of Fig. 2(b) at $B_{\|} = 272.8$ mT (dashed arrow) shows Rabi-split transmission dips. The best fit to Eq. (1) gives $g_{\text{ens}} = 17.0$ MHz. (b) Measured loaded quality factor of $\lambda/4$ mode as a function $B_{\|}$ at $T = 0.25$ K. The best fit of Eq. (1) away from the avoided crossings gives $g_{\text{ens}} = 3.9$ MHz. Arrows point to satellites resulting from hyperfine coupling of electron spin to the nuclear spin of ^{13}C atoms adjacent to some P1 centers. Only transitions corresponding to energy splitting of $m_I = -1$ and $+1$ are visible, the other four are overshadowed by the ^{14}N hyperfine lines. (c) Best-fit g_{ens} to the $\lambda/4$ (circles) and $3\lambda/4$ (squares) modes as a function of temperature. Solid curves are the best fits of Eq. (2). Error bars are smaller than the symbol size.

7.5 Relaxation time of the spin ensemble

Having characterized coherent coupling in the hybrid system, we now turn to using the resonator as a probe of spin dynamics and equilibration. We first measure linewidth γ of the $m_I = +1$ transition in the dispersive regime [10], with ~ 70 MHz $\gg g_{\text{ens}}$ detuning between the $\lambda/4$ mode and $m_I = +1$ transition. We extract γ by measuring the resonator shift (Δf) immediately following a pump pulse whose frequency is stepped through resonance with the $m_I = +1$ transition [Fig. 7.4(b)]. The pump pulse slightly decreases the polarization of the ensemble, red shifting the resonance. We fit a Lorentzian lineshape to $|\Delta f|$, finding a full-width-at-half-maximum $\gamma/2\pi = 9.0 \pm 0.3$ MHz. A similar dispersive measurement using the $3\lambda/4$ mode at $B_{\|} = 263$ mT gives $\gamma/2\pi = 12.0 \pm 0.7$ MHz. The increase in γ with $B_{\|}$ is attributed to field inhomogeneity. Furthermore, we find these values to be temperature independent below 1.2 K [Fig. 7.4(c)], which is consistent with γ being limited by dipolar interactions and field inhomogeneity.

The spin relaxation time is measured by applying a pump pulse resonant with the $m_I = +1$ transition and monitoring the frequency shift in time as the spin polarization returns to equilibrium. We observe a bi-exponential decay response with time constants ~ 20 s and ~ 160 s [Fig. 7.4(d)]. These constants

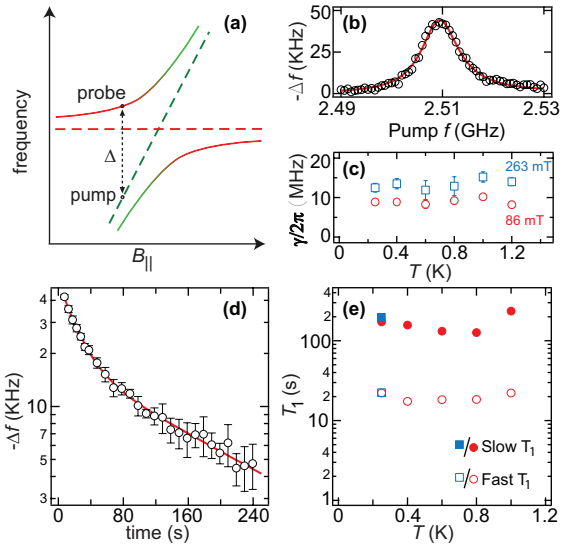

Figure 7.4: Measurement of spin linewidth and relaxation times using dispersive spin-resonator interactions. (a) Schematic and (b) measurement of spin linewidth (T = 0.25 K, $B_{||}$ = 86 mT) obtained by probing the frequency shift of the $\lambda/4$ mode at $f = (f_r - \Delta f_r/2) = 2.58$ GHz after applying a pump pulse (0.4 s duration, −50 dBm incident power) through resonance with the $m_I = +1$ transition (60 s wait between successive measurement points). A similar measurement of γ at $B_{||}$ = 263 mT is obtained using the $3\lambda/4$ mode. (c) γ at $B_{||}$ = 86 mT (circles) and $B_{||}$ = 263 mT (squares) as a function of temperature. (d) Measurement of spin relaxation time T_1 by probing the resonator shift as a function of time after the pump pulse switches off. A bi-exponential decay is observed. (e) Temperature dependence of the two time constants, extracted by probing with the $\lambda/4$ (circles) and $3\lambda/4$ (squares) modes. Error bars, unless shown, are smaller than the symbol size.

are independent of temperature below 1 K [Fig. 7.4(e)], suggesting that spin polarization decay is not limited by spin-lattice relaxation [22] but spin diffusion instead. Through dipolar flip-flop processes, the depolarization diffuses out of the resonator mode volume, leading to repolarization of the ensemble. The rate for this process depends on the dipolar coupling strength, which itself depends on the spin density [14]. The two time constants may be explained by two diamond sectors inside the mode volume with electron-spin densities differing by a factor of ~ 8 [25, 26] (see section 7.8).

7.6 Spin exchange between sub-ensembles

To investigate spin dynamics across sub-ensembles, we measure how pumping one sub-ensemble can affect the coupling strength of other sub-ensembles to the resonator (see section 7.8). As shown in Fig. 7.5(a), pumping at $f_{m_I=0}(B_\parallel)$ completely suppresses the avoided crossing between the $m_I = 0$ transition and the resonator [2]. Remarkably, partial depolarization is evident in the $m_I = \pm 1$ sub-ensembles. The coupling strengths of the undriven transitions ($m_I = \pm 1$) to the $3\lambda/4$ mode are reduced to $g_{\rm ens}/2\pi = 12.5 \pm 0.5$ and 12.0 ± 0.5 MHz, respectively. To quantify this steady-state cross-relaxation, we measure the minimum-splitting between the hybridized dips at $B_\parallel = 269.1$ mT [arrow in Fig. 4(a)] as a function of pump power $P_{\rm p}$. As shown in the inset of Fig. 7.5(b), the undriven $m_I = 1$ sub-ensemble depolarizes further with increasing $P_{\rm p}$. We can reproduce (see section 7.8) this power-dependent steady-state cross-depolarization using a rate equation including a spin diffusion rate $\Gamma_{\rm o}$ across the mode volume and a cross-relaxation rate Γ between sub-ensembles [21]. We assume $\Gamma \gg \Gamma_{\rm o}$ consistent with previous measurements of cross-relaxation in high density P1-center samples by Sorokin *et al.* [26]. Under these assumptions, the steady-state normalized polarization of each sub-ensemble is $\bar{P} = \Gamma_{\rm o}/(\Gamma_{\rm o}+\Omega_0/3)$, where Ω_0 is the pumping rate for the $m_I = 0$ transition. Excellent agreement is found with the model, with only the lever arm between Ω_0 and $P_{\rm p}$ as free parameter. Using the best-fit lever arm in combination with Fermi's golden rule $\Omega_0 = 2\pi g^2 N_{\rm phot}/\gamma$ and the measured $\Gamma_{\rm o} \approx 0.05$ s^{-1} and $\gamma/2\pi \approx 12$ MHz, we estimate $g \sim 2.5$ Hz. [3] Comparing this g to $g_{\rm ens}(T = 0)$ suggests $N \sim 10^{14}$ spins in the resonator mode volume.

7.7 Conclusions

In conclusion, we have used resonant and dispersive interactions with the two lowest-frequency modes of a NbTiN CPW resonator to probe the dynamics of a P1 electron-spin ensemble in diamond at low temperature and polarizing magnetic field. The temperature independence of spin linewidth and relaxation below 1.2 K supports spin out-diffusion as the dominant relaxation mechanism within the resonator mode volume. Resonant pumping of spin sub-ensembles reveals strong cross-relaxation between sub-ensembles. Although this indicates exchange of spin excitations between the sub-ensembles [21], we cannot pinpoint the exact mechanism for cross-relaxation. Follow-up experiments probing the sub-ensemble

[2] This is surprising from a single-spin perspective, because the maximum Rabi driving strength ($f_{\rm Rabi} = g\sqrt{N_{\rm phot}}/2\pi \approx 100$ kHz for $N_{\rm phot} = 10^8$ photons on mode resonance) is significantly smaller than the spin linewidth

[3] Note that $N_{\rm phot}$ is lower than on mode resonance by the filter factor $(\kappa_{\rm i}+\kappa_{\rm e})^2/(f_{\rm c}-f_{\rm pump})^2$.

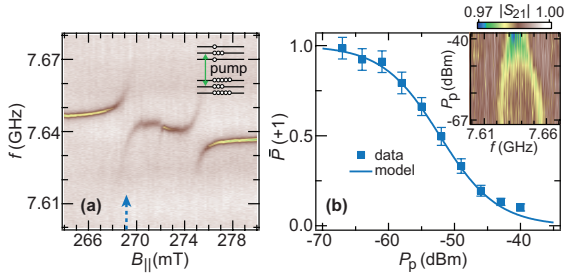

Figure 7.5: (a) Transmission spectroscopy similar to Fig. 7.2(b), with an additional pump pulse resonant with the $m_I = 0$ transition (incident pump power $P_\mathrm{p} = -50$ dBm, 100 ms duration) prior to $|S_{21}|$ measurement. A complete disappearance of the $m_I = 0$ avoided crossing and a reduction in the coupling strength of the undriven transitions are observed. Color scale is the same as in Fig. 7.2(b). (b) Inset: vacuum-Rabi-split dips at $B_\parallel = 269.1$ mT as a function of P_p. The merging of dips with increasing P_p indicates cross-relaxation between the sub-ensembles. Main panel: Extracted polarization $\bar{P}$ (normalized to value without pump) for the undriven $m_I = +1$ sub-ensemble. The curve corresponds to the steady-state solution of a rate equation modeling fast equilibration between sub-ensembles compared to T_1 (see text and section 7.8 for details).

response to one or more resonant pump pulses on millisecond timescales could shed light on the mechanism. The rate of cross-relaxation will ultimately set the time scale over which sub-ensembles may serve as independent quantum memories.

Acknowledgments

We thank D. Ristè for experimental assistance. We acknowledge funding from the Dutch Organization for Fundamental Research on Matter (FOM, grant 12PR3001), the Netherlands Organization for Scientific Research (NWO, VIDI grant 680-47-508), and a Marie Curie Career Integration Grant (grant 304249).

7.8 Additional material

Measurement setup

The device is operated in a ^{3}He refrigerator with base temperature $T = 0.25$ K. All measurements involve continuous-wave heterodyne detection of feedline transmission S_{21} as a function of $B_\parallel$ and T with 1 MHz intermediate frequency and

80 ms integration. Incident power on the feedline ranges from −115 to −95 dBm (−110 to −90 dBm) for the $\lambda/4$ ($3\lambda/4$) mode, corresponding to $\sim 10^3$ to 10^5 intra-cavity photons on resonance (incident power for one photon on resonance $\approx \hbar f_c(\kappa_i + \kappa_e)^2/2\kappa_e$ [27]). All other microwave pulses are also applied through the feedline. At $B_\parallel = 0$ the diamond-coupled resonator has $\lambda/4$ and $3\lambda/4$ modes at 2.59 and 7.67 GHz, respectively ($\sim$ 11% lower than the values without the diamond). The reduction in frequency of the resonator after mounting diamond is due to the higher effective dielectric constant of the diamond ($\sim$ 5.7). The corresponding loaded quality factors are $Q = f_c/(\kappa_i + \kappa_e) = 1.8 \times 10^4$ and 6×10^3 ($\sim$ 3 times lower than the values without the diamond). Increase in intrinsic losses could come from the surface of the diamond itself or/and from the vacuum grease used to glue it on top of the resonator. Increasing $B_\parallel$ to 300 mT further decreases Q by $\sim$ 15%. To release trapped magnetic flux and reduce losses in the superconducting film the system is frequently reset by warming above the film T_c at $B_\parallel = 0$.

Avoided crossings

Transmission spectroscopy measurements in Fig. 2 reveal two regimes of spin-resonator coupling. Rabi-split dips are clearly resolved [Fig. 3(a)] when the $m_I = 0$ transition is resonant with the $3\lambda/4$ mode, evidencing strong coupling ($2g_{ens} > \gamma, \kappa$). To extract g_{ens} in this case, we fit Eq. (1) to $|S_{21}|(f)$ [12]. For this fit, we fix κ_i, κ_e and γ to independently-measured values: $\kappa_i = 1.4 \pm 0.1$ MHz and $\kappa_e = 120 \pm 10$ kHz are extracted on both sides of the avoided crossings, and $\gamma/2\pi = 12.0 \pm 0.7$ MHz is obtained from dispersive pump-probe linewidth measurements (Fig. 5).

The $\lambda/4$ mode is weakly coupled to the resonator with $2g_{ens} < \gamma$ and Rabi-split dips are not resolved on resonance. The extraction of a coupling strength to this mode involves several steps. First, we extract the field-dependent loaded quality factor Q by fitting a lineshape

$$S_{21}(\omega) = \frac{S_{21}^{min} + i2Q(\omega - f_r)/f_r}{1 + i2Q(\omega - f_r)/f_r}$$

to the measured $|S_{21}|(\omega)$ at each magnetic field. Figure 3(a) shows $Q(B_\parallel)$ near the avoided crossings for the $\lambda/4$ mode at $T = 0.25$ K. The decrease in Q when the spin transitions are tuned into resonance with the resonator is caused by absorption of microwave energy by the spin ensemble. An analytic approximation of $Q = f_r/\Delta f_r$ valid away from the avoided crossings can be obtained from Eq. (1) and noting that on resonance, where $|S_{21}|$ is minimum, $\mathrm{Im}(S_{21}) \approx 0$. Here,

$$\Delta f_{\mathrm{r}} = (\kappa_{\mathrm{i}} + \kappa_{\mathrm{e}}) + \sum_n g_{\mathrm{ens}}^2 \frac{\gamma/2}{(\Delta_{\mathrm{n}}^2 + \gamma^2/4)}$$

and $\Delta_{\mathrm{n}} = \omega_{\mathrm{r}} - \omega_{m_I=n}$. The fixed values, $\gamma/2\pi = 9.0 \pm 0.3$ MHz, $\kappa_{\mathrm{i}} = 140 \pm 10$ kHz and $\kappa_{\mathrm{e}} = 32 \pm 1$ kHz, are obtained by the same methods as described for the $3\lambda/4$ mode.

The extraction of g_{ens} requires accounting for all ensembles in the last term of Δf_{r}. We also observe two small dips ~ 4.1 mT away from the avoided crossings with the $m_I = \pm 1$ transitions [indicated by arrows in Fig. 3(b)]. These dips are consistent with coupling to the nuclear spin ($I = 1/2$) of a ^{13}C (1.1% natural abundance) at the nearest-neighbor carbon site present on the Jahn-Teller axis ($A_{^{13}\mathrm{C,a}} = \mathrm{diag}(141.8, 141.8, 340.8)$ MHz [28]). These give rise to six sub-ensembles with coupling strengths $g^{\mathrm{a}}_{\mathrm{ens},^{13}\mathrm{C}} \approx g_{\mathrm{ens}}\sqrt{0.011/2}$. The factor $1/2$ comes from the fact that ^{13}C has nuclear spin of $I = 1/2$ in contrast to ^{14}N ($I = 1$) Additionally, there are six more ^{13}C transitions with $A_{^{13}\mathrm{C,b}} = \mathrm{diag}(32.1, 32.1, 41.0)$ MHz [28], which arise from ^{13}C located at the three remaining nearest-neighbor sites. These are three times more abundant with $g^{\mathrm{b}}_{\mathrm{ens},^{13}\mathrm{C}} \approx \sqrt{3} g^{\mathrm{a}}_{\mathrm{ens},^{13}\mathrm{C}}$. Although they are not visible as separate dips in the data, they do modify $Q(B_\parallel)$. We therefore include all of these sub-ensembles in our modeling.

One can in principle also find an analytical expression for the dispersive shift of the resonance with respect to f_{c} and use it to extract g_{ens} for the $\lambda/4$ mode. In our experiments, however, this is problematic due to sudden changes in f_{c} [indicated by the arrow in Fig. 3(a)] caused by flux jumps in the NbTiN film. The absorption, however, only depends on f_{r}, which is extracted with high precision from the transmission lineshape.

Pumping and depolarization of sub-ensembles

To study the dynamics of spins within and between the sub-ensembles, we resonantly pump the $m_I = 0$ transition and measure the effect on the sub-ensembles. The pulse sequence used for transmission spectroscopy $|S_{21}|(f, B_\parallel)$ in Fig. 4(a) is shown in Fig. 7.6.

We model the depolarization of spin ensembles due to pumping with a simple rate equation. In addition to the pumping rate Ω_0 for the driven transition ($m_I = 0$), we include a spin-equilibration rate Γ_{o} (spin diffusion rate across the resonator mode volume) within each sub-ensemble and a dipolar flip-flop rate Γ that characterizes cross-relaxation between the sub-ensembles. The rate of change of polarization (equal for $m_I = \pm 1$ due to symmetry), is modeled by

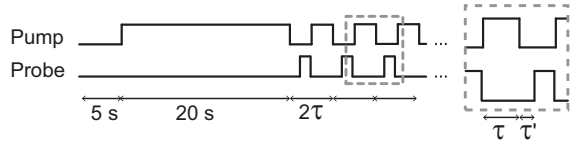

Figure 7.6: Schematic of pump- and probe-tone timings used in Fig. 4. At each $B_\parallel$ setting, following a 5 s waiting time, pump pulses resonant on driven transitions are applied for 20 s. This is followed by a periodic series of pumping and probing steps (period 2τ), with the probe frequency f stepped at the start of every cycle. The probe is always on, but $|S_{21}|(f)$ only measured for a time $\tau - \tau'$. Here τ' is a settling time of 20 ms. While for 2-D transmission spectroscopy [Fig. 4(a)], $\tau = 100$ ms, for measurements of Rabi-split dip separation as a function of pump power at fixed $B_\parallel$ [Figs. 4(b)], $\tau = 270$ ms.

$$\frac{d}{dt}\bar{P} = -M\bar{P} + \Gamma, \tag{7.4}$$

with

$$\bar{P} = \begin{bmatrix} \bar{P}(\pm 1) \\ \bar{P}(0) \end{bmatrix},$$

$$\Gamma = \Gamma_o \begin{bmatrix} 1 \\ 1 \end{bmatrix},$$

and

$$M = \begin{bmatrix} \Gamma_o + \Gamma & -\Gamma \\ -2\Gamma & \Gamma_o + \Omega_0 + 2\Gamma \end{bmatrix}.$$

The steady-state polarization ($d\bar{P}/dt = 0$ condition) is $\bar{P} = M^{-1}\Gamma$, yielding

$$\bar{P}(\pm 1) = \frac{\Gamma_o(\Gamma_o + 3\Gamma + \Omega_0)}{\Gamma_o(\Gamma_o + 3\Gamma + \Omega_0) + \Gamma\Omega_0}.$$

For $\Gamma \gg \Gamma_o$ [26], this expression simplifies to $\bar{P}(\pm 1) = \bar{P}(0) = \Gamma_o/(\Gamma_o + \Omega_0/3)$. In this limit, the fast equilibration between sub-ensembles causes pumping of each transition with an effective rate $\Omega/3$, even though only one transition is directly driven by the pump.

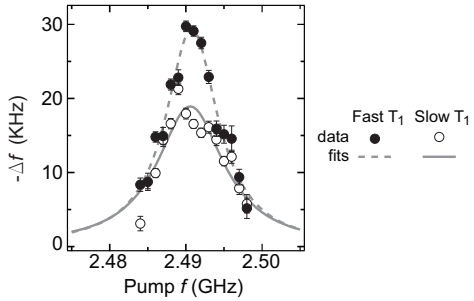

Figure 7.7: Best-fit amplitudes of the two exponential terms observed in the relaxation measurement as function of pump frequency. Lorentzian fits have widths $\gamma_1 = 8.5 \pm 0.5$ MHz (solid circles) and $\gamma_2 = 10.7 \pm 1.5$ MHz (open circles) for fast and slow decays, respectively. Within error bars, these widths are consistent with the spin linewidth measurements in Fig. 5(b-c).

Spin polarization recovery time

Measuring the relaxation of pumped spins over time reveals bi-exponential decay curves. A possible reason for this observation would be the presence of two sectors with different densities of spins in our diamond sample. This is corroborated by several tests. First, we repeat the experiment with the pump far detuned from any spin transition and observe no shift in the resonance frequency. This excludes the possibility that one of the time constants results from the pump influencing the resonator shift (for example, through heating). Second, we perform the experiment varying the pump pulse frequency around $f_{m_I=+1}$ and observe that the amplitudes of both exponentials are modulated by the spin linewidth (see Fig. 7.7). This excludes the possibility of a broad background spin ensemble such as paramagnetic impurities on the surface of NbTiN or diamond itself. In addition, the ratio of $g_{\mathrm{ens}}(T = 0)$ values for the two modes differs from the expected $\sqrt{3}$ by a factor ~ 1.6. This further hints at a strong inhomogeneity of P1 concentration across the diamond.

Bibliography

[1] J. H. Wesenberg *et al.* Quantum computing with an electron spin ensemble. *Phys. Rev. Lett.* **103**, 070502 (2009).

[2] J. Clarke and F. K. Wilhelm. Superconducting quantum bits. *Nature* **453**, 1031 (2008).

[3] M. V. G. Dutt *et al.* Quantum register based on individual electronic and nuclear spin qubits in diamond. *Science* **316**, 1312 (2007).

[4] G. Balasubramanian *et al.* Ultralong spin coherence time in isotopically engineered diamond. *Nature Materials* **8**, 383 (2009).

[5] X. Zhu *et al.* Coherent coupling of a superconducting flux qubit to an electron spin ensemble in diamond. *Nature* **478**, 221 (2011).

[6] Y. Kubo *et al.* Hybrid quantum circuit with a superconducting qubit coupled to a spin ensemble. *Phys. Rev. Lett.* **107**, 220501 (2011).

[7] H. Malissa *et al.* Superconducting coplanar waveguide resonators for low temperature pulsed electron spin resonance spectroscopy. *Arxiv:1202.6305* (2012).

[8] Y. Kubo *et al.* Electron spin resonance detected by a superconducting qubit. *ArXiv:1205.5659* (2012).

[9] A. Imamoglu. Cavity qed based on collective magnetic dipole coupling: Spin ensembles as hybrid two-level systems. *Phys. Rev. Lett.* **102**, 083602 (2009).

[10] R. Amsüss *et al.* Cavity qed with magnetically coupled collective spin states. *Phys. Rev. Lett.* **107**, 060502 (2011).

[11] Y. Kubo *et al.* Strong coupling of a spin ensemble to a superconducting resonator. *Phys. Rev. Lett.* **105**, 140502 (2010).

[12] D. I. Schuster *et al.* High-cooperativity coupling of electron-spin ensembles to superconducting cavities. *Phys. Rev. Lett.* **105**, 140501 (2010).

[13] J. H. N. Loubser and J. A. van Wyk. Electron spin resonance in the study of diamond. *Rep. Prog. Phys.* **41**, 1201 (1978).

[14] J. A. van Wyk, E. C. Reynhardt, G. L. High and I. Kiflawik. The dependences of esr line widths and spinŰspin relaxation times of single nitrogen defects on the concentration of nitrogen defects in diamond. *J. Phys. D: Appl. Phys.* **30**, 1790 (1997).

[15] P. Bushev *et al.* Ultralow-power spectroscopy of a rare-earth spin ensemble using a superconducting resonator. *Phys. Rev. B* **84**, 060501 (2011).

[16] M. U. Staudt *et al.* Coupling of an erbium spin ensemble to a superconducting resonator. *J. Phys. B: At. Mol. Opt. Phys.* **45**, 124019 (2012).

[17] A. M. Tyryshkin *et al.* Electron spin coherence exceeding seconds in high-purity silicon. *Nature Materials* **11**, 143 (2012).

[18] S. Takahashi, R. Hanson, J. van Tol, M. S. Sherwin and D. D. Awschalom. Quenching spin decoherence in diamond through spin bath polarization. *Phys. Rev. Lett.* **101**, 047601 (2008).

[19] G. de Lange *et al.* Controlling the quantum dynamics of a mesoscopic spin bath in diamond. *Sci. Rep.* **2**, 382 (2012).

[20] R. Barends *et al.* Minimal resonator loss for circuit quantum electrodynamics. *Appl. Phys. Lett.* **97**, 023508 (2010).

[21] N. Bloembergen, S. Shapiro, I. S. Pershan and J. O. Artman. Cross-relaxation in spin systems. *Phys. Rev.* **114**, 445 (1959).

[22] E. C. Reynhardt, G. L. High and J. A. van Wyk. Temperature dependence of spin-spin and spin-lattice relaxation times of paramagnetic nitrogen defects in diamond. *J. Chem. Phys.* **109**, 8471 (1998).

[23] R. J. Cook and D. H. Whiffen. Electron nuclear double resonance study of a nitrogen centre in diamond. *Proc. R. Soc. Lond. A* **295**, 99 (1966).

[24] E. Abe, H. Wu, A. Ardavan and J. J. L. Morton. Electron spin ensemble strongly coupled to a three-dimensional microwave cavity. *Appl. Phys. Lett.* **98**, 251108 (2011).

[25] R. Burns *et al.* Growth-sector dependence of optical features in large synthetic diamonds. *J. Crystal Growth* **104**, 257 (1990).

[26] P. P. Sorokin, G. J. Lasher and I. L. Gelles. Cross relaxation studies in diamond. *Phys. Rev.* **118**, 939 (1960).

[27] R. Barends. *Photon detecting superconducting resonator.* Ph.D. thesis, TU Delft (2009).

[28] A. Cox, M. E. Newton and J. M. Baker. 13c, 14n and 15n endor measurements on the single substitutional nitrogen centre (p1) in diamond. *J. Phys.: Condens. Matter* **6**, 551 (1994).

Chapter 8

Conclusions and outlook

The field of quantum control with single quantum objects has developed beyond the point of proof of principle experiments. We are now at the stage where there is a need to perfect these control techniques and use them to push the boundaries in quantum science and technology further. The research presented in this thesis demonstrates how pulse sequences with high fidelity can be applied in the fields of metrology and experimental quantum information science. A summary of the achieved results is given below.

8.1 Summary and conclusions

The experiments in this thesis were aimed to improve, and provide new avenues for, quantum science and technology with spins. The second goal of this thesis was to provide more insight into decoherence in the central spin problem and solid-state spin systems. High fidelity quantum control was used to extend storage times of quantum information stored in a single electronic spin by dynamical decoupling from its spin bath environment.

We showed that multi-pulse sequences can be used to increase the interrogation time of a single-spin magnetometer, improving to improve its sensitivity, and to tune its spectral properties. The demonstration of quantum control of the nitrogen spin environment surrounding a single NV center is the first experimental step towards achieving the coherent coupling of distant NV centers using chains of nitrogen impurities [1, 2] and environment assisted magnetometry [3]. Additionally, it has provided a means to directly observe the decay of correlations in the spin bath.

In our experiments we observed that we can extend the coherence time of

the central spin beyond the bath correlation time. Our results are accurately reproduced theoretically by taking a mean-field approach to the central spin problem. This theory predicts that there is no fundamental limit as to how well the central spin can be decoupled from the spin bath. In practice the limit for the coherence time will be set by spin-lattice relaxation and finite pulse lengths.

These findings can be directly transferred to other systems with a spin bath environment such as quantum dots [4,5] and donors in silicon [6,7]. Furthermore, the techniques developed in this thesis enabled the first demonstration of dynamically protected quantum gates [8]. In addition to diamond dynamical decoupling has found use in a variety of systems, such as trapped ions [9], superconducting qubits [10], rare-earth ions [11], quantum dots [5] and donors in silicon [12], in the context of quantum information and metrology.

Lastly, we have investigated the spin physics of a high-density nitrogen spin ensemble using a superconducting resonator. We investigated the spin dynamics on long timescales and observed spin diffusion and considerable cross-relaxation between hyperfine transitions. Understanding these dynamics is important if one is to consider using a nitrogen spin ensemble as a long term memory for superconducting qubits.

8.2 Open issues and future directions of the field

Although NV centers and nitrogen impurities in diamond are systems with exceptional properties they are far from perfect. A few of the open issues will be listed in this section which have to be dealt with in order for them to reach their true potential. There are already many highly creative ideas put forward and large ongoing experimental efforts underway to tackle these issues. In the process, they will undoubtedly lead to new insights and applications that may impact many other areas of quantum science and technology.

The coherent coupling of distant NV centers

There are several approaches to achieving the coherent coupling between distant NV quantum registers. Two approaches seem to be the most promising.

First, there is the coupling by optical means to achieve entanglement and do computations. All ingredients for this proposal, such as spin-photon entanglement [13], single-shot read out [14] and two photon interference [15] of two NV centers have been demonstrated experimentally. The biggest issue here will be the success probability of generating an entangled NV pair. The main limitation seems to be the limited number of photons emitted in the zero phonon line (ZPL). Several approaches have been investigated to increase the emission into the ZPL using optical cavities in GaP [16] and diamond [17] films. In the latter

experiment the emission into the ZPL was enhanced to 70% of the total emission. The challenge is now to enhance the extraction efficiency of the enhanced ZPL emission.

Second, there is the approach using magnetic coupling either direct, or mediated by a chain of nitrogen spins. The direct coupling between two NV centers roughly 10 nm apart has been demonstrated [18]. However, the unfavorable $1/r^3$ scaling of coupling strengths with NV separation poses a severe limitation of this approach. One can also think of a more indirect way of magnetically coupling two distant NV centers which uses chains of nitrogen electron spins [1, 19] to transfer quantum information. When a achain of spins is used the effective coupling strength between remote registers scales more favorably with distance then the direct coupling by dipolar means. This approach requires implantation techniques which are in principle available. It also requires coherence of the nitrogen spins in the chain which might be limited by the presence of other magnetic moments. As we have demonstrated in chapter 6 the nitrogen spins can be controlled on nanosecond timescales and it is in principle possible to apply decoupling techniques to extend the coherence of chain spins.

Diamond based magnetometry

Single spin magnetometers based on NV centers are perhaps most promising because of their compatibility with living cells and high spatial resolution [20]. In order to achieve high spatial resolution NV magnetometers can be created using diamond nanocrystals, which can be as small as 5 nm.

Such small nanocrystals in general contain large concentrations of nitrogen impurities and may have many strain induced structural defects with a magnetic moment. Together with magnetically active states on the surface of the nanocrystal, which are in close proximity to the NV centers in nanocrystals, these defects form a highly dynamic environment that causes decoherence of the NV spin and degrades sensitivity. In principle this problem can be removed by dynamical decoupling. However, this only works for slow magnetic environments with a relatively long correlation time. In most present nanocrystals, however, a considerable portion of the magnetic environment has a relatively short correlation time.

It seems that for improving the quality of nanocrystals the problem is one of material science. It is interesting to note that if the magnetic moments associated with defects other then nitrogen impurities can be eliminated, the nitrogen impurities can be controlled and turned into a resource [3] to further improve the sensitivity of such magnetometers. An increased understanding of the type of defects involved and new developments in the growth of cleaner nanocrystals (in terms of additional magnetic moments besides N and NV centers) may ultimately

enable us to use of NV magnetometers to image protons in single molecules.

Strong coupling between superconducting resonators and nitrogen spin ensembles

Although this is a relatively new research area, already remarkable results have been achieved in diamond with NV centers [21–24] and nitrogen spins [25]. In chapter 7 we explored the properties of a high-density nitrogen spin ensemble coupled to a superconducting NbTiN resonator.

The purity of the nitrogen spin ensemble and quenched decoherence at high polarizing magnetic field [26] are desirable features when nitrogen spin ensembles are used as long-term memory for superconducting qubits. However, the density of the nitrogen spin ensemble studied here is too high with too strong coupling between the spins in the ensemble. As a consequence inhomogeneous broadening and cross-relaxation between sub-ensembles pose a severe obstacle for using these ensemble as a quantum memory. Lower density samples should be used instead. The nominal spin-spin coupling scales linearly with density [27]. Reducing the density, however, will reduce the coupling strength between resonator and spin ensemble, but this reduction scales with the square root of the density.

There are certainly more significant developments needed on both the superconducting and spin ensemble side before nitrogen spins ensemble can be used as quantum memory. First, to access the long memory times for the storage of quantum information, high fidelity quantum control at dilution-fridge temperatures of the spin ensemble needs to be developed in order to apply the required echo techniques. Achieving strong driving requires large amplitude and homogeneous microwave magnetic fields to be delivered to the whole ensemble. This can be done by either using the superconducting resonator itself to drive the ensemble or by an external driving circuit [28]. This is challenging to achieve in a dilution fridge, but not fundamentally impossible.

Second, high magnetic fields are required in order to polarize the nitrogen spin ensemble. Operating superconducting quantum circuits at high in-plane magnetic fields is challenging and superconducting qubits that survive high magnetic fields have not yet been demonstrated. Approaches that are being pursued in our group today use ultra-thin aluminum films and disordered superconductors such as those used in Ch. 7 to create such qubits. Their development is essential if one is to use solid-state spin ensembles as a quantum memory.

Bibliography

[1] N. Y. Yao *et al.* Robust quantum state transfer in random unpolarized spin chains. *Physical Review Letters* **106**, 040505 (2011).

[2] A. Ajoy and P. Cappellaro. Perfect quantum transport in arbitrary spin networks. *arXiv:1207.5580v1* (2012).

[3] G. Goldstein *et al.* Environment-Assisted Precision Measurement. *Physical Review Letters* **106**, 140502 (2011).

[4] R. Hanson, L. P. Kouwenhoven, J. R. Petta, S. Tarucha and L. M. K. Vandersypen. Spins in few-electron quantum dots. *Reviews of Modern Physics* **79**, 1217 (2007).

[5] H. Bluhm *et al.* Dephasing time of gaas electron-spin qubits coupled to a nuclear bath exceeding 200 μs. *Nature Physics* **7**, 109 (2011).

[6] B. E. Kane. A silicon-based nuclear spin quantum computer. *Nature* **393**, 133 (1998).

[7] J. J. L. Morton *et al.* Solid-state quantum memory using the 31p nuclear spin. *Nature* **455**, 1085 (2008).

[8] T. van der Sar *et al.* Decoherence-protected quantum gates for a hybrid solid-state spin register. *Nature* **484**, 82 (2012).

[9] M. J. Biercuk *et al.* Optimized dynamical decoupling in a model quantum memory. *Nature* **458**, 996 (2009).

[10] J. Bylander *et al.* Noise spectroscopy through dynamical decoupling with a superconducting flux qubit. *Nature Physics* **7**, 565 (2011).

[11] J. Du *et al.* Preserving electron spin coherence in solids by optimal dynamical decoupling. *Nature* **461**, 1265 (2009).

[12] Z.-H. Wang *et al.* Effect of pulse error accumulation on dynamical decoupling of the electron spins of phosphorus donors in silicon. *Physical Review B* **85**, 085206 (2012).

[13] E. Togan *et al.* Quantum entanglement between an optical photon and a solid-state spin qubit. *Nature* **466**, 730 (2010).

[14] L. Robledo, H. Bernien, T. van der Sar and R. Hanson. Spin dynamics in the optical cycle of single nitrogen-vacancy centres in diamond. *New Journal of Physics* **13**, 025013 (2011).

[15] H. Bernien *et al.* Two-photon quantum interference from separate nitrogen vacancy centers in diamond. *Physical Review Letters* **108**, 043604 (2012).

[16] T. van der Sar *et al.* Deterministic nanoassembly of a coupled quantum emitter - photonic crystal cavity system. *Applied Physics Letters* **98**, 193103 (2011).

[17] A. Faraon, C. Santori, Z. Huang, V. M. Acosta and R. G. Beausoleil. Coupling of Nitrogen-Vacancy Centers to Photonic Crystal Cavities in Monocrystalline Diamond. *arXiv:1202.0806v1* (2012).

[18] P. Neumann *et al.* Quantum register based on coupled electron spins in a room-temperature solid. *Nature Physics* **6**, 249 (2010).

[19] N. Yao *et al.* Scalable architecture for a room temperature solid-state quantum information processor. *Nature Communications* **3**, 800 (2012).

[20] C. L. Degen. Scanning magnetic field microscope with a diamond single-spin sensor. *Applied Physics Letters* **92**, 243111 (2008).

[21] Y. Kubo *et al.* Strong Coupling of a Spin Ensemble to a Superconducting Resonator. *Physical Review Letters* **105**, 140502 (2010).

[22] Y. Kubo *et al.* Electron spin resonance detected by a superconducting qubit. *arXiv:1205.5659* (2012).

[23] R. Amsüss *et al.* Cavity qed with magnetically coupled collective spin states. *Physical Review Letters* **107**, 060502 (2011).

[24] X. Zhu *et al.* Coherent coupling of a superconducting flux qubit to an electron spin ensemble in diamond. *Nature* **478**, 221 (2011).

[25] D. Schuster *et al.* High-cooperativity coupling of electron-spin ensembles to superconducting cavities. *Physical Review Letters* **105**, 140501 (2010).

[26] S. Takahashi, R. Hanson, J. van Tol, M. Sherwin and D. Awschalom. Quenching Spin Decoherence in Diamond through Spin Bath Polarization. *Physical Review Letters* **101**, 047601 (2008).

[27] A. Abragam. *Principles of Nuclear Magnetism.* Clarendon Press, Oxford (1961).

[28] H. Malissa *et al.* Superconducting coplanar waveguide resonators for low temperature pulsed electron spin resonance spectroscopy. *arxiv:1202.6305* (2012).

Summary

Quantum control and coherence of interacting spins in diamond

In this thesis we describe experiments on solid-sate spins in diamond in the context of quantum science and technology. In particular we focus on the spin associated with single nitrogen vacancy (NV) centers and nitrogen impurities. The NV center is a fluorescing defect in diamond which consists of a single substitutional nitrogen atom and an adjacent vacancy in the diamond carbon lattice. The electronic spin associated with the NV center can be initialized and read out optically and coherently controlled with high fidelity at room temperature using microwave pulses. The nitrogen impurity also consists of a single substitutional nitrogen atom and has an electron spin associated with it. Unlike the NV center, the nitrogen impurity is optically inactive and can only be detected through its magnetic moment.

Research on spins in diamond started already in the late 50's and an extensive literature already exists on the subject. Recently, research with diamond spins, especially with NV centers, has intensified dramatically owing to their unique properties that are useful for applications in quantum science and technology. In this thesis we use spins in diamond to investigate quantum control techniques in the context of quantum information technology, spin-based metrology and to study the fundamentals of decoherence.

To be able to exploit quantum control of isolated quantum systems, control errors have to be kept at a minimum. Minimizing these errors starts by knowing what they are exactly. In chapter 3 we have developed, and experimentally verified, a pulse tomography technique that determines the rotation axis and angle errors for pulses used in quantum control. We also show how knowledge of these errors can be used to correct the results of quantum process tomography.

In chapter 4 we apply quantum control and show that we can preserve an arbitrary quantum state of a single NV spin by self-correcting dynamical decoupling sequences. In dynamical decoupling the refocussing effect is used that is

achieved by periodically inverting the state of a two level system by a sequence of π pulses. We performed quantum process tomography to show that our dynamical decoupling protocol indeed is equal to the identity process and that no decoherence is introduced by the operations. The scaling of the coherence time with the number of pulses is accurately predicted by our mean-field theoretical model of the electron spins bath. From this theory we conclude that with dynamical decoupling, decoherence caused by the spin bath no longer sets the upper limit for the coherence time, but is set by spin-lattice relaxation and finite length of the pulses.

The spin of the NV center can also be used as an extremely sensitive magnetic-field probe. In chapter 5 we used dynamical decoupling pulse sequences as sensing sequences to improve the sensitivity of a NV spin magnetometer for AC magnetic fields by eliminating the magnetic noise resulting from its direct magnetic environment. We showed this improvement for both phase locked signals as well as for signals that do not have a well defined phase. We also demonstrated the spectral filtering characteristics of both the periodic CPMG-like sequences and the aperiodic UDD sequence.

In chapter 6 we demonstrated magnetic resonance spectroscopy and quantum control of the mesoscopic spin environment of a single NV spin. In these experiments we use the NV center as a probe to detect resonances and quantum dynamics of its local spin environment. The interaction strengths between the NV spin and individual spectral groups within the spin bath were measured. Dephasing of the NV spin was suppressed by controlling the spin bath. The ability to extend the dephasing time of the NV spin will improve the sensitivity when it is used as a DC magnetometer. We used double resonance techniques to perform a direct measurement of the spin dephasing, spin echo and correlation times of the spin bath. We find that our results are in excellent agreement with the mean-field theoretical model referred to previously.

Ensembles of diamond spins can also be used in hybrid devices where they are coupled to other quantum systems such as superconducting quantum circuits. In such devices the spin ensemble can be used as a quantum memory for qubits with short coherence times. Understanding the internal dynamics of the spin ensemble and how it depends on the ensemble density is, apart from a fundamental perspective, an important aspect in finding the optimum design parameters for such hybrid devices. In chapter 7 we demonstrate that strong coupling can be achieved between a high-density ensemble of nitrogen spins and a NbTiN superconducting coplanar waveguide resonator. We observed hyperfine transitions associated with the ^{14}N nitrogen and ^{13}C nuclei. We further demonstrate strong depolarization of the whole ensemble by selectively pumping one hyperfine transition. The power dependence of the depolarization is consistent with considerable cross-relaxation between hyperfine transitions. Finally, we probe the coupling

strengths, spin line-width and spin-relaxation time as a function of temperature. We find a bi-exponential decay with the two time constants independent of temperature. From the temperature dependence we conclude that spin relaxation is dominated by dipolar processes instead of spin lattice relaxation.

Gijs de Lange
Delft, 2012

Samenvatting

Quantum controle en coherentie van interacterende spins in diamant

In dit proefschrift worden experimenten beschreven waarin onderzocht wordt hoe quantumcontrole van spins in de vaste stof gebruikt kan worden voor toepassingen in nieuwe quantum technologieën en fundamenteel onderzoek in de quantumfysica. In onze experimenten gebruiken we de spintoestand van geïsoleerde nitrogen-vacancy (NV) centra en stikstofverontreinigingen in diamant. Het NV centrum is een fluorescerend defect in diamant bestaande uit een substitutioneel stikstofatoom naast een lege plek in het kristalrooster. De spintoestand van het NV centrum kan optisch worden geïnitialiseerd en uitgelezen. Tevens kan zijn toestand coherent worden gemanipuleerd met hoge precisie met behulp van microgolfpulsen. De stikstofverontreiniging, ook wel P1 centrum genoemd, bestaat uit een enkel substitutioneel stikstofatoom in het kristalrooster van diamant met een donorelektron gelokaliseerd bij het defect. Anders dan het NV centrum zijn stikstofverontreinigingen niet optisch actief en zij kunnen alleen worden waargenomen door middel van het magnetisch moment geassocieerd met de spin toestand van het donorelektron.

Het onderzoek naar spins in diamant begon al aan het einde van de vijftiger jaren. Er bestaat dan ook al een aanzienlijke hoeveelheid literatuur over het onderwerp. In de laatste tien jaar heeft het onderzoek naar spins in diamant, in het bijzonder dat naar het NV centrum, een enorme vlucht genomen vanwege zijn unieke eigenschappen, die erg gunstig zijn voor toepassingen in nieuwe quantumtechnologieën en voor fundamentele quantumwetenschap. Dit proefschrift concentreert zich hoofdzakelijk op de onderzoeksgebieden quantum informatie, metrologie en de fundamentele studie naar decoherentie.

Om quantumcontrole van geïsoleerde quantumsystemen te kunnen gebruiken voor nieuwe toepassingen is het nodig dat fouten in de microgolfpulsen, die gebruikt worden voor het manipuleren van quantumtoestanden, tot een minimum worden beperkt. Het analyseren en minimaliseren van pulsfouten begint met

weten wat ze zijn. In hoofdstuk 3 hebben we een nieuwe pulstomografie techniek ontwikkeld, en experimenteel getest, waarmee de fouten in de rotatie-hoeken en assen van quantumcontrolepulsen kunnen worden bepaald. Tevens laten we zien hoe de kennis van deze fouten kan worden gebruikt om de resultaten van quantumprocestomografie, waarin quantumcontrolepulsen worden gebruikt, te corrigeren.

In hoofdstuk 4 passen we quantumcontrole toe om de spintoestand van een enkel NV centrum te beschermen tegen de verstorende invloed van het bad van elektronspins, behorende bij omringende stikstofverontreinigingen, met behulp van zelfcorrigerende dynamische ontkoppelingspulssequenties. In dynamische ontkoppeling wordt de herfocusserende werking van het herhaaldelijk inverteren van een twee-niveausysteem met π-pulsen gebruikt om omgevingsinvloeden uit te middelen. We laten zien met behulp van quantumprocestomografie dat het dynamische-ontkoppelingsproces gelijk is aan de identiteitsmatrix en dat elke spintoestand met hoge precisie bewaard kan worden. In onze experimenten laten we zien dat de coherentietijd van de spintoestand van het NV centrum kan worden verlengd met meer dan een factor 25. De schaling van de coherentietijd met het aantal ontkoppelingspulsen wordt exact gereproduceerd door een model waarin de invloed van het elektronspinbad wordt benaderd met behulp van gemiddeldeveldtheorie. Deze theorie voorspelt dat met dynamische ontkoppeling de limiet voor het verlengen van de coherentietijd van een enkel elektron in een langzaam spinbad niet gesteld wordt door de interactie met het spinbad, maar dat de (veel langere) spin-relaxatietijd en eindige pulslengte de limiet zijn voor de coherentietijd.

De spintoestand van het NV centrum kan ook gebruikt worden als extreem gevoelige magneetveldsensor. In hoofdstuk 5 laten we zien hoe dynamische ontkoppelingssequenties gebruikt kunnen worden als meetsequenties om de gevoeligheid en spectrale selectiviteit van op spin gebaseerde magneetveldsensoren te verbeteren. We laten zien dat de verbetering geldt zowel voor AC signalen die een goed gedefinieerde fase hebben, als AC signalen met een willekeurige fase. Ook meten we de spectrale filterkarakteristiek van deze sensoren voor zowel de periodieke CPMG sequentie, als de aperiodieke UDD sequentie.

In het onderzoek naar individuele quantumsystemen speelt decoherentie een hoofdrol. Voor het NV centrum in diamant wordt decoherentie veroorzaakt door de magnetische interactie met spins in de directe mesoscopische omgeving. In hoofdstuk 6 laten we zien hoe het NV centrum gebruikt kan worden om magnetische resonantiespectroscopie en quantum controle van de spins in zijn directe omgeving te meten. Tevens meten we de bijdragen van verschillende spectrale groepen in het spinbad aan het toestandsverval van het NV centrum. Het toestandsverval van de spintoestand van het NV centrum kan worden onderdrukt door de dynamische ontkoppeling toe te passen op de spins in de omgeving van

het NV centrum. Dit is belangrijk wanneer het NV centrum wordt gebruikt als DC magneetveld sensor. We gebruiken dubbele resonantietechnieken om de lijnbreedtes, spinecho vervaltijden en correlatietijden van spectrale groepen van het spinbad te meten en laten zien dat deze resultaten eveneens met grote precisie worden gereproduceerd door de eerder gebruikte gemiddelde veldtheorie.

Ensembles van spins in diamant kunnen ook gebruikt worden in hybride structuren waarin ze zijn gekoppeld aan andere quantumsystemen zoals supergeleidende quantumcircuits. Hiermee kan de spin dynamica worden gemeten en het ensemble zou als quantumgeheugen voor supergeleidende qubits met korte coherentietijden kunnen fungeren. Het begrijpen van de dynamiek in zulke ensembles is, afgezien van een fundamenteel oogpunt, een belangrijk onderdeel voor het vinden van het optimale ontwerp parameters voor zulke hybride structuren. In hoofdstuk 7 demonstreren we sterke koppeling tussen een ensemble van stikstofspins en een supergeleidende resonator. We observeren de hyperfijne transities behorende bij kernspin behoudende elektronspintransities van het stikstof spinensemble. Daarnaast demonstreren we sterke depolarisatie van het gehele ensemble wanneer op een van deze transities word gepompt. De afhankelijkheid van de depolarisatie als functie van het pompvermogen is consistent met een uitwisseling van excitaties tussen de verschillende hyperfijne transities, die vele malen sneller is dan de tijdschaal waarop het hele ensemble herpolariseert. Tevens is de temperatuursafhankelijkheid gemeten van de koppelingsterkte met de resonator, de spin lijnbreedte en de herpolarisatiesnelheid van het spin ensemble. De koppelingsterkte hangt af van de polarisatie welke de Boltzmann statistiek volgt. De tijd waarin het ensemble herpolariseert is onafhankelijk van temperatuur. Hieruit wordt geconcludeerd dat de spin relaxatie dynamica gedomineerd wordt door dipool processen in plaats van spin-rooster relaxatie.

Gijs de Lange
Delft, 2012

Acknowledgements

I first joined the quantum transport (QT) group as a master student to do my final research project, I found out that the people in QT are, in at least one way, like me; They all get very enthusiastic about things no normal person really cares about. But the common interests did not stop there. I was happily surprised when I observed what happens when they are not working. I found out that during the many "leisure" activities things have a tendency of getting out of hand. They party with the same vigor and enthusiasm as they do their work. What happens when QT invades local bars and disco's around the world is hard to describe. Let's just say that QT has a reputation not only for its academic activities. For me it was clear that after my master thesis I wanted to do a PhD in QT. Working and partying with people like that in such a great place for more than five years was very stimulating and has resulted in many extremely fun memories. Being such a large group means I have many people to thank for the excitement and fun I experienced during this time. I'll start with the people I worked most closely with.

First and foremost, I thank the person who guided me in the research I did as a PhD student in his newly-formed group, now known as Team Diamond. Ronald, I thank you for hiring me (and for seeing the nine years I spent studying as a plus). Your vision, leadership, incredible sharpness, focus and humor are the primary reasons why I can look back at four years of fun and, in my opinion, incredible results. I have learned a lot from you and I feel privileged to have taken part in the startup of your research group. It was impressive and exciting to watch you establish yourself in such a highly competitive field of science. Again, thank you for everything.

When I started there were only two group members and an empty lab space, Ronald and one PhD student who started a few months before me. Toeno, I learned a lot from you while we were setting up the lab and from our many discussions. You are the personification of the QT party spirit and I have extremely enjoyed all the good times we spent outside the lab (they were well worth every hangover). Thank you for letting me be your paranimf and for being mine.

Team diamond has grown substantially since I started and every addition to the team has played a huge role in the fun and success I had the past four years. Lucio, you started your postdoc one or two weeks after me. You are one of the most skilled experimental quantum optics experts and smartest guys I know. I learned a lot from the discussions we had over all kinds of technical details and I appreciate your relaxed attitude towards everything and everyone. Herr Pfaff, I am amazed at how much time you can spend in the cleanroom and still keep your enthusiasm and sense of humor. I enjoyed your jokes and our conversations, with and without beervolume, and I thank you for the wiedergutmachungsschnitzels. Your switch to the low-temperature setup(s) has clearly been a great success and I am convinced there is much more to come. Hannes (Haaannus), it was fun working on the QM homework with you. At the moment I'm writing these words you are probably entangling distant NV centers, big ups for that, and for your diamond tits! Tim, when you arrived spin-physics was not exactly your "cup of tea". I am impressed by how fast you mastered RT1 and the results you pulled out of that setup. Also, I very much enjoyed the discussions we had about your data. Bas, good luck with implementing your entanglement scheme and I have no doubt your PhD in team diamond will be very successful. I have had the privilege of supervising several master and bachelor students. Machiel, although I supervised only for a small part of your master thesis project, I enjoyed controlling bath spins with you. Good luck with your PhD in team diamond. I am intimidated by how well you handle tequila. Someone like you I can definitely use as a paranimf. Diego, when you started your master project with me your experimental skills were essentially non-existent and when you tried to connect a BNC to an SMA, I got a bit worried. It turned out to be the most productive year of my PhD and you were one of the main reasons for that. You are now a PhD student in the group of Leo D. where I will do my postdoc. You will probably have to teach me about experiments with superconducting circuits. I look forward to that! Ron, you took a chance starting with me on my last project and worked very hard with enormous enthusiasm to make it the success it is now. I know this was not an easy year for you so all the more respect for that. Just one piece of advice; Don't pick anymore fights with aggressive "ouwe Hagenezen" and make sure you never loose your shoe in the Pijpela again. Arthur, you were the first to realize our pulse fidelities were high. Good luck with consulting. To the other master students that spent time in Team diamond, I wish you all the best. Greg, thanks for the "stimulated" laughs. Ilse, it was fun realizing you can do spin-locking with the optical transition of the NV center, good luck with your PhD and thank you for letting us use you transfer tube. Gerwin, good work on the resonant detection and spin-photon entanglement, and have fun in Boulder. Jelmer, nice job on the missing echo's. Lilly, you were in our group as a guest, I really admire your scientific and didactic skills, thank you for the discussions.

I was also privileged to collaborate with several very talented people outside Team Diamond as well. Slava, most of the ideas for the experiments in this thesis started in your head. I think every experimental group should have a theorist like you. Thank you for explaining to me what I was doing all these years. Zhihui, thank you for the simulations and work on our papers. Leo D., hybridizing with your group has been a great experience with a fair amount of fireworks. I look forward to doing my postdoc in your group. Vishal, I really enjoyed working on the hybrids with you. I hope our paper gets accepted regardless of any missing articles in front of the nouns. Thibault, I wish you all the best.

The fun and excitement I had was not restricted to the people I worked closely with. I thank all the current, and former, members of QT that made the group to what it is today. This would all have not been possible without Hans and Leo. Hans, thank you for creating all the necessary conditions that allowed QT to grow into the world leading research group that it is today. I was honored to be a master student in your sub-group. Leo, thank you for your atypical way of stimulating and facilitating people to interact in settings that extend well beyond the physics building. Thank you for being my promotor. Kees, I have learned so much from you and your intuitive way of explaining physics. Ad, you helped me understand a lot about fabrication. Val, I don't think you will ever have enough lab space to execute all your ideas. Lieven, thank you for commenting on our papers and being on my committee. I have no doubt that under your leadership QT will continue to be the motivating and successful group it is now.

The group can not function without all the support from the administrative and technical staff. Angele, Yuki, Dominique and Marja thank you so much for helping me with all the paperwork and for saving the group from anarchy and for the interest in my personal well-being. Bram, working across the hall from a noisy liquefier made me appreciate your cheerful whistling all the more. Remco, I still did not read the book... Jelle, thanks for all the help. Raymond, it has been said many, many, many times before, but you're the electronics guru and without you, most of the experiments in QT would not have been possible. Sitting in an office next to yours has the great benefit of receiving all kinds of mini demonstrations. Thank you for all of them and I hope to see many more.

I would also like to thank my office mates. Floris, thank you for sticking with me in the office a.k.a the graveyard and for training my anti beer shower defenses. Gabriele, thank you for all the five minute breaks. I enjoyed everyone of them. Maaike, I liked all the discussions about physics and thank you for thinking about my propositions.

Other (former) members of QT I would like to name Stijn and Tim, we corrected many many homework assignments together a tedious task that was made much less tedious because of you. Pieter, thank you for introducing me to python and for taking your job as the group feeder so seriously. Reinier,

without qtlab I would not have been able to do my experiments, thanks for all the help with python. Iron Mike, your low heart rate impresses me, I hope my hummingbird heart will allow me to keep up with you someday. Thanks for your comments on my thesis. Han, that moment of suspense and look in your eyes before you start speaking always makes me think there is some dirty joke or remark coming. I thank you for all of them but also for the times you didn't. Vincent, thanks for the comforting conversations and your laughs. Victor, I am impressed by your ability to sleep in bars. Gary, thanks for making sure there is visual evidence of the "activities" during the QT trips. Maria, thank you so much for organizing the very nice trip to Geneva. I thank Sergey, Nika, Vlad, Guen, Basia, Pierre, Daniel, Fei, Johan, Kun, Arjan and all the others for your contributions to creating such a stimulating environment and for keeping the QT party spirit high. The same goes for all the former members, Arkady, Martin, Lan, Thomas, Katja, Sander, Moira, Floor, Floris, Jelle, Ivo, Lars, Juriaan, Umberto, Stevan, Georg, Maarten and Maarten.

Regardless of having nice colleagues, I would not have been anywhere without the close group of friends and family surrounding me. Being part of the merry band of weirdos (a.k.a Lappen) that I have entered adulthood with, has shaped me into the person I am today (not in the least by helping me get rid of my slowest braincells). I hope you can forgive me all the sjaak-afhaak moments in the past years. To you, and also to all my other friends, thank you for all your support and for making life so easy and fun.

To my in-laws, your support has been invaluable. I am very grateful to be part of the family. To my brother and sisters, thank you for taking care of your little brother. To my parents, I know it has not been easy to watch me find my way in life. I can not thank you enough for your support and everlasting patience and confidence.

Finally, Christa, we have experienced our two most important moments in life together. The loss of our first son, Teun, and the birth of our second, Michiel. They have made me both the saddest and happiest person alive. Thank you for showing me that no matter what happens, as long as I am with you, life can not be better.

Gijs de Lange
Delft, 2012

Curriculum Vitae

Gijsbertus de Lange

Nov. 8, 1980	Born in Rotterdam, The Netherlands.
1993 - 1999	Secondary school, Erasmus College, Zoetermeer.
1999 - 2002	Propaedeutic Applied Physics, *Delft University of Technology.*
2003 - 2006	B. Eng. Applied Physics, *Rijswijk University of Professional Education.* Graduation research at Netherlands Institute for Space Research (SRON) under supervision of Dr.ir. J.J.A. Baselmans.
2005 - 2008	M. Sc. Applied Physics, *Delft University of Technology.* Graduation research in the Quantum Transport group under supervision of Dr. Pol-Forn Diaz and Prof.dr.ir. J.E. Mooij.
2008 - 2012	Ph.D. research at *Delft University of Technology.* Subject: Quantum control and coherence of interacting spins in diamond. Group: Quantum Transport, Kavli Institute of Nanoscience. Promotor: Prof.dr.ir. L.P. Kouwenhoven. Copromotor: Dr.ir.R. Hanson.

List of publications

1. *Probing the dynamics of an electron-spin ensemble via a superconducting resonator.*
   V. Ranjan, G. de Lange, R. Schutjens, T. Debelhoir, J. P. Groen, D. Szombati, D. J. Thoen, T. M. Klapwijk, R. Hanson and L. DiCarlo.
   In preperation.

2. *Controlling the quantum dynamics of a mesoscopic spin bath in diamond.*
   G. de Lange, T. van der Sar, M. S. Blok, Z. H. Wang, V. V. Dobrovitski and R. Hanson.
   Scientific Reports **2**, 382 (2012).

3. *Comparison of dynamical decoupling protocols for a nitrogen-vacancy center in diamond.*
   Z. H. Wang, G. de Lange, D. Ristè, R. Hanson and V. V. Dobrovitski.
   Physical Review B **85**, 155204 (2012).

4. *Een geflipt elektron leeft langer.*
   G. de Lange, T. van der Sar and R. Hanson.
   Nederlands Tijdschrift voor Natuurkunde, Januari 2012.

5. *Single-spin magnetometry using mulipulse sensing sequences.*
   G. de Lange, D. Ristè, V. V. Dobrovitski and R. Hanson.
   Physical Review Letters **106**, 080802 (2011)

6. *Universal dynamical decoupling of a single solid-state spin from a spin bath.*
   G. de Lange, Z. H. Wang, D. Ristè, V. V. Dobrovitski and R. Hanson.
   Science **330**, 60 (2010).

7. *Bootstrap tomography of the pulses for quantum control.*
   V. V. Dobrovitski, G. de Lange, D. Ristè and R. Hanson.
   Physical Review Letters **105**, 077601 (2010).

8. *Nanopositioning of a diamond nanocrystal containing a single nitrogen-vacancy defect center.*
   T. van der Sar, E. C. Heeres, G. M. Dmochowski, G. de Lange , L. Robledo, T. H. Oosterkamp, and R. Hanson.
   Applied Physics Letters **94**, 173104 (2009).